Lunar Magnetism

Exploring the origin of lunar magnetic anomalies through the Parker Inversion method

Jacopo Baccarin

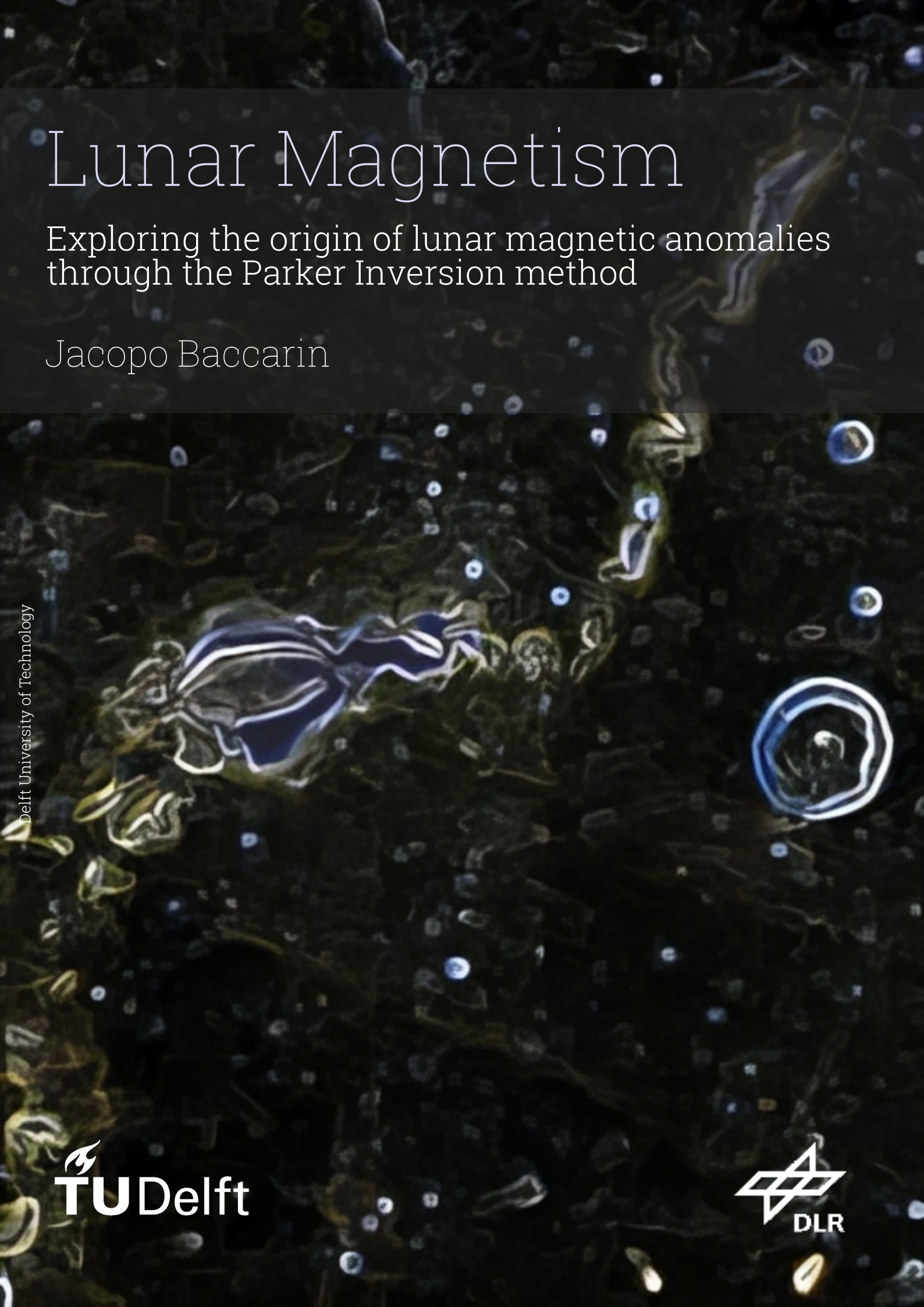

Delft University of Technology

TU Delft

DLR

Lunar Magnetism

Exploring the origin of lunar magnetic anomalies through the Parker Inversion method

by

Jacopo Baccarin

to obtain the degree of Master of Science
at the Delft University of Technology,
to be defended publicly on Monday March 28, 2025 at 10:45 AM.

Student number:	5702003	
Faculty:	Faculty of Aerospace Engineering, Delft	
Project duration:	June 10, 2024 – March 14, 2025	
Thesis supervision:	Dr. Julia Maia,	DLR
	Dr. ir. Bart C. Root,	TU Delft
	Dr. Joana S. Oliveira,	Telespazio for ESA
	Dr. Ana-Catalina Plesa,	DLR

Cover:	NASA Clementine UV-VIS artistically modified color image of the Reiner Gamma magnetic anomaly / swirl and surroundings.
Style:	TU Delft Report, with modifications by Daan Zwaneveld.

An electronic version of this thesis is available at http://repository.tudelft.nl/.

TU Delft

Preface

This report aims to resume, contextualize, and describe the thesis project carried out at the DLR Planetary Physics Department in Berlin, which began on the 10^{th} of June 2024 and concluded on the 14^{th} of March 2025. The project was conducted in collaboration with Telespazio for ESA and exists under the Space Engineering TU Delft master program. The project focuses on investigating the origin of lunar magnetic anomalies using a recently adapted inversion algorithm, the Parker inversion method. Specifically, the role of large impacts is evaluated through correlative analyses.

Before starting, I would like to express my heartfelt gratitude to all my supervisors for embarking on this journey with me and for learning alongside me: I thank Julia, who supervised me from the Internship project and continued to guide me even when the planetary body and dataset transitioned from the more familiar gravity on Venus to the entirely different magnetic field on the Moon. I can confidently say you did an awesome job with your first supervised student! I thank Joana, who welcomed me into her area of expertise of the last years and shared her knowledge, providing it to me in such a way that enabled me to trust myself throughout the learning process and confidently navigate my own journey of discovery. I thank Bart, who always offered wise and encouraging words during meetings, helped me understand the broader context of the project, and (Root)ed for me throughout my personal thesis journey. And last but by no means least, I thank Ina, who, despite her numerous obligations, always found time to contribute with insightful and expert transversal suggestions. I also extend my thanks to Sabatino for the free peer to peer consultations and for the encouragement that proved instrumental in helping me push forward at crucial moments.

The completion of this project marks the end of my university career, but certainly not the end of my learning journey. Looking ahead to the future, I find inspiration in the words of Yuri Gagarin, who, before boarding the Vostok 1 spacecraft to become the first human in space, turned to Sergei Korolev, the chief engineer, and said, *"Поехали!"* (pronounced "Poyekhali"), meaning 'Off we go!' (to do great things).

Jacopo Baccarin
Berlin, March 2025

Contents

List of Figures

List of Tables

Nomenclature

Abbreviations

Abbreviation	Definition
AC	Alternating Current
ALSEP	Apollo Lunar Surface Experiment Package
ESA	European Space Agency
ESD	Equivalent Source Dipole
IMF	Interplanetary Magnetic Field
JAXA	Japan Aerospace Exploration Agency
KREEP	Potassium (K), Rare Earth Elements (REE), Phosphorus (P)
LP	Lunar Prospector
LRO	Lunar Reconnaissance Orbiter
LSM	Lunar Surface Magnetometer
MAG/ER	Magnetometer/Electron Reflectometer
NASA	National Aeronautics and Space Administration
NNLS	Non-Linear Least Squares
NRM	Natural Remanent Magnetization
PFS	Particles and Fields Subsatellite
PLSE	Passive Lunar Seismic Experiment
PRM	Pressure Remanent Magnetization
PKT	Procellarum KREEP Terrane
pTRM	partial Thermal Remanent Magnetization
RMS	Root Mean Square
SELENE	Selenological and Engineering Explorer
SPA	South Pole - Aitken
SRM	Shock Remanent Magnetization
SSD	Sum of Squared Discrepancies
TRCM	Thermochemical Remanent Magnetization
TRM	Thermal Remanent Magnetization
USA	United States of America
VRM	Viscous Remanent Magnetization

Symbols

Symbol	Definition	Unit
B	Magnetic flux density	T
B_r	Radial component of the magnetic field	T
B_θ	Polar component of the magnetic field	T
B_ϕ	Azimuthal component of the magnetic field	T
d	Radial magnetic field (notation in equations)	T
$\vec{d}$	vector of the radial magnetic field observations	T
F	Misfit function	T
g	Radial magnetic field of a single point dipole in the volume (notation in equations)	T
G	Matrix of containing g elements	
H	Magnetic field strength	Am^{-1}
M	Magnetization	Am^{-1}
m	Magnetic moment	Am^2
m_{cutoff}	Cutoff magnetic moment (assumed as 30% of m_{max})	Am^2
m_{max}	Maximum modeled magnetic moment	Am^2
$\hat{m}$	Magnetization direction	
N_d	Number of dipoles in the crust (subscript i refers to one of the N_d dipoles)	
N_o	Number of observations (subscript j refers to one of the N_o observations)	
τ	Magnetic torque	Am^2
μ_0	Permeability of free space	NA^{-2}
V	Volume	m^3

Abstract

Lunar magnetism has remained an unsolved mystery since the Apollo era. The Moon currently lacks a global magnetic field, yet its crust displays heterogeneous magnetization of debated origin. The prevailing hypotheses attribute this magnetization either to an extinct core dynamo that once generated a global magnetic field or to transient magnetic fields induced by large impacts.

Over the years, various datasets have fueled investigations into this puzzle — from lunar rock samples brought back to Earth, to magnetic field measurements with global coverage from orbit and local coverage from the lunar surface. However, the resulting interpretations often conflict. Paleomagnetic studies of lunar samples conducted in laboratory environments suggest that the rocks recorded strong, Earth-like magnetic fields between approximately 4 and 3.5 billion years ago — a necessary condition to explain their remanent magnetization. Such findings point to the existence of an ancient, long-lived core dynamo. However, the field intensities inferred from laboratory analyses are difficult to reconcile with physical simulations of core dynamo models, which consistently yield weaker magnetic fields. On the other hand, simulations exploring post-impact magnetic field generation at the antipode of large impacts propose the alternative transient magnetic field mechanism, but these processes struggle to reproduce the observed field strengths or account for the longevity of crustal magnetization. Magnetic maps derived from orbital data, meanwhile, often fail to establish a direct correlation between magnetic anomalies and any clear geological or geophysical structures.

A major limitation in many previous studies using observational data is their reliance on the existing geological context to interpret magnetic anomalies — an approach that is inherently constrained by the lack of clear surface expressions for most magnetic features. This investigation on the origin of magnetic anomalies overcomes such limitations through a novel approach: the implementation of the versatile Parker inversion method to estimate the spatial distribution, intensity, and direction of surface magnetization that best fits a set of local magnetic data — without the need to reference any pre-existing geological structures. Moreover, it is shown mathematically that by assuming a unidirectional magnetization, a volumetric distribution of dipoles within the crust can be simplified to a surface layer of dipoles, reducing the complexity of the problem from three dimensions to two.

By applying the Parker inversion method, this study investigates the origin of lunar magnetic anomalies by inferring the surface magnetization, which was never obtained before for an extensive number of anomalies. Particularly, it's studied whether the origin can be attributed to magnetized impact ejecta or antipodal processes, and whether the enigmatic lunar albedo anomalies (swirls) trace the distribution of magnetized material.

The correlative analyses suggest that impacts play a prominent role in shaping lunar magnetism. Most isolated near-side anomalies are likely the result of magnetized ejecta from the massive Imbrium impact, with additional contributions from ejecta of other young Imbrian and Nectarian basins. On the lunar far side, surface magnetized material is found to coincide with antipodal regions of large basins — notably Imbrium, Orientale, Serenitatis, Crisium, and Nectaris — suggesting that antipodal magnetization may result from the concentration of ejecta and/or shock waves and/or an impact melt cloud at these complexly magnetized locations. Anomalies at the lunar North Pole are found in proximity to the Schrödinger antipode, pointing to a possible antipode-related origin, while the weak anomalies near the South Pole remain enigmatic and are tentatively proposed to stem from impact ejecta. A third

mechanism is identified in the form of localized magnetization of central impact melt deposits within large impact basins. Swirls (lunar albedo anomalies) are found to consistently outline the distribution of surface magnetized material, reinforcing their role as tracers of crustal magnetization.

Overall, the findings favor a hybrid scenario in which a long-lived core dynamo served as the primary magnetic field source, with impact events strongly contributing to the magnetization of the crust, through magnetized ejecta, antipodal magnetization and central impact melt magnetization. The hypothesis of transient magnetic fields alone is found unlikely to fully explain the observed magnetic features, but impact formed plasma clouds could have acted as amplifiers of a weaker global field. These results provide new insights into the intricate relationship between impact processes and the Moon's magnetic history, offering a step forward in unraveling the origin of lunar magnetism.

1 Introduction

1.1. Pioneering Lunar Science: the beginning of the Space Age

The study of planetary magnetism has long been a key to unlocking the mysteries of celestial bodies. While Earth, with its core-powered magnetic field, has traditionally been the primary focus, the onset of the Space Age in 1957 with the Sputnik 1 (Garcia, 2017) shifted global attention beyond our home planet, particularly to the Moon. The Soviet Luna and American Apollo programs (Siddiqi & Office, 2018), driven by competition, accelerated lunar exploration and the study of its magnetic field. Since the earliest missions, investigating the lunar magnetic field was straightforward thanks to the inclusion of magnetometers — lightweight, low-cost, and easy-to-manufacture instruments that became a common feature in spacecraft's payloads. When placed on satellites orbiting the Moon, magnetometers measured the strength and direction of the lunar magnetic field. Observational data from missions such as Luna 2 (NASA NSSDC, 2024e), the first spacecraft to reach the Moon's surface in 1959 as an impact probe, Luna 10 (NASA NSSDC, 2024d) (1966), and NASA's Explorer 35 (NASA NSSDC, 2024c)(1967-1973) soon confirmed the absence of a significant global dipolar magnetic field (e.g., Dolginov et al., 1966, Sonett et al., 1967). These early findings aligned with the prevailing consensus before 1960, which suggested that the Moon, being much smaller and less geologically active than the Earth and other rocky planets, likely lacked a core capable of sustaining a global magnetic field through a dynamo process (Runcorn, 1983). Challenging the early erroneous consensus that the Moon lacked magnetization altogether, the Apollo program and its 17 missions (1961–1972, Siddiqi and Office, 2018) instead revealed the presence of crustal magnetic anomalies. Of fundamental importance were the rock samples brought back to Earth from the famous Apollo 11 mission (NASA NSSDC, 2024a) and some of the following missions (Apollo 12, 14, 15, 16, 17). The first paleomagnetic records obtained from laboratory analyses of Apollo samples suggested the presence of strong surface magnetic fields (Fuller, 1974), later linked to a time span between approximately 3.9 and 3.7 Gyrs (Cisowski et al., 1983; Fuller & Cisowski, 1987). During the Apollo 15 and 16 missions, in 1971 and 1972 respectively, small sub-satellites (PFS-1 and PFS-2) released into lunar orbit collected magnetic data that confirmed the presence of crustal magnetization on the Moon. These measurements revealed that the magnetic field signals are heterogeneously distributed, with the strongest and largest magnetic anomalies concentrated on the lunar far side. In addition to orbital magnetic data and paleomagnetic records obtained from laboratory analysis of lunar rocks, another type of data has further confirmed the Moon's magnetized state: surface magnetic measurements from lunar ground-based observations (Dyal & Parkin, 1971). These measurements were conducted by the Lunar Surface Magnetometer (LSM), which was deployed by Apollo astronauts as part of the Apollo missions 12, 14 and 16 as part of ALSEP, the Apollo Lunar Surface Experiment Package (US, 1971).

The Apollo program significantly enhanced our understanding of the Moon and its magnetic properties. However, by the end of its operational days, many questions remained unanswered. One of the central questions that arose from the initial findings, and one that became crucial for advancing the study of lunar magnetism, was whether the Moon possesses or ever possessed a metallic core. Determining the presence or absence of such a core is vital for interpreting the magnetic data and understanding the origin of lunar magnetization. Furthermore, this insight could provide important clues about the Moon's differentiation, its geological history, and its comparison to the internal structures and evolutionary pathways of other planetary bodies in the solar system. Evidence of a solid metallic core was strongly hinted by the observed time delay in P-waves following a meteoritic impact (Latham et al., 1973), as detected by ALSEP's Passive Lunar Seismic Experiment (PLSE). This delay was longer than expected if the Moon were composed entirely of silicate materials (a wholly silicate Moon was a strong hypothesis before these findings, e.g., Urey and Korff, 1952), indicating a possible core radius of up to 350 km (Nakamura et al., 1974). Further evidence came from Sonett (1982) that examined the increase in electrical conductivity in the Moon's deep interior induced by the solar wind, finding evidence of a conductive core with a radius potentially extending to 400 km. In more recent days, J. G. Williams et al. (2006) found indication of a partly molten core from the Moon's time-variable rotations. Increased confidence emerged with the reanalysis of old Apollo seismic data with modern techniques by Weber et al. (2011), confirming the presence of a solid core composed predominantly of iron and a fluid outer core (see Figure 1.1). In conclusion, the Moon possesses a relatively small core, making up roughly 20% of its radius, in contrast with the larger cores of most other terrestrial bodies, which are typically about 50% of their radius (Mercury is one of the most notable exceptions, with 80%). The lunar core is now believed to be partially molten, with its composition not fully determined but thought to consist primarily of iron, with small amounts of sulfur and nickel (Righter et al., 2017).

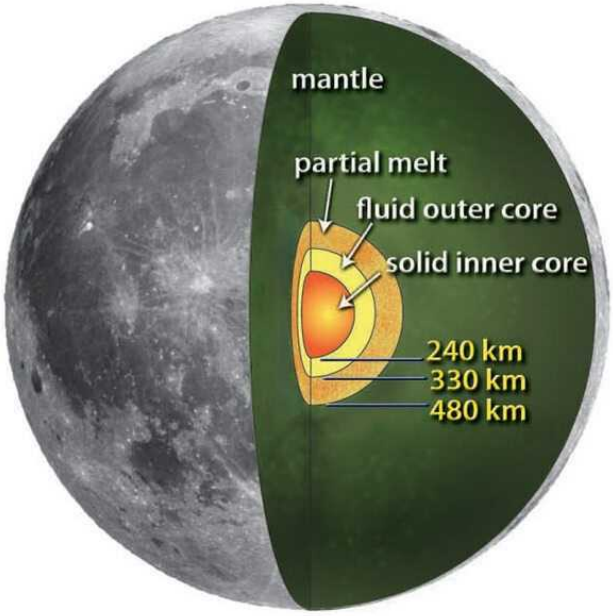

Figure 1.1: Lunar internal core and mantle stratification, with thickness values from Weber et al. (2011). Figure modified from Weber et al. (2011).

1.2. A New Era in Lunar Science: Global Magnetic Mapping and the 1990s-2000s Renaissance

After the Apollo era ended in 1972 and the Luna program concluded in 1976, the Moon was largely overlooked by space missions for about two decades. While Apollo missions provided valuable magnetic field data, their measurements were too fragmented and localized to construct a comprehensive global map. It was not until later missions, such as Lunar Prospector (1998-1999) (Binder, 1998) and Kaguya (2007-2009) (Kato et al., 2010), that magnetic maps with extensive coverage were produced. NASA's Lunar Prospector was equipped with a magnetometer and an electron reflectometer for magnetic mapping purposes. Launched into a $\sim$100 km polar orbit, it gathered improved magnetic data when lowered to $\sim$15-45 km during the extended phase of the mission. The peculiarity of the MAG/ER instrument was that the magnetometer recorded the magnetic field strength at approximately 30 km altitude, while the electron reflectometer measured the flux of low-energy electrons reflected from the lunar surface. These electrons interact with the lunar crustal magnetic fields, which is why the electron

reflectometer is employed in the study. JAXA's Kaguya (The Japanese nickname given to the mission SELENE — Selenological and Engineering Explorer) included a magnetometer onboard its main orbiter (of the three separate spacecrafts featured in the mission), and observed the magnetic field around the Moon in low-altitude (9-80 km) polar orbits. The orbit was then lowered with periapsis near the South Pole — Aitken (SPA) basin to record the strong anomalies related to that area. Thanks to these two missions, magnetic field maps with global coverage, higher resolution and improved sensitivity have been produced. The most notable maps are those produced by Tsunakawa et al. (2015), Ravat et al. (2020) and Hood, Torres, et al. (2021), depicting the total magnetic field strength of the Moon at 30 km altitude. These maps will be the primary datasets of the analysis and will be discussed in more detail in Chapter 3.

1.3. A Long-Standing Question: The Origin of Lunar Crustal Magnetization

The diversity of magnetic datasets available for the Moon — from lunar samples, ground and spacecraft-based magnetometers — resulted in a complex picture of lunar magnetism. Pinpointing the location, intensity, and direction of its sources is necessary to understand the origin of crustal magnetization (Carley et al., 2012) but is a challenging task. One of the major unanswered questions is the origin of the lunar magnetic sources, a topic debated since the first Apollo missions. Solving it requires identifying the geological processes responsible for magnetic anomalies, along with the power source of the magnetic field, which must have been active during those processes. Two main theories are currently under debate regarding the origin of the ambient magnetic field that imparted magnetization to the lunar crust:

- The first focuses on an ambient magnetic field of internal origin, generated by a now extinct core-generated dynamo (Cisowski et al., 1983; Garrick-Bethell et al., 2009; Tikoo et al., 2017; Wieczorek et al., 2023). The core-dynamo is a mechanism that allows a celestial body to generate and sustain a magnetic field and relies on the motion of a rotating, convecting, and electrically conductive fluid, which preserves the magnetic field over long timescales. Such a fluid typically consists of a partially molten metallic core (e.g., Duba and Ringwood, 1973, J. G. Williams et al., 2014) but could also take the form of a more exotic magma ocean (Scheinberg et al., 2018). To note, the core-dynamo mechanism is at the origin of the Earth's magnetic field (Elsasser, 1958).
- The second theory suggests that an ambient magnetic field could result from the local amplification of a pre-existing magnetic field through the combined effects of plasma clouds, shock waves, and ejecta generated by meteoroid impacts (Hood & Artemieva, 2008; Hood & Vickery, 1984; Lin et al., 1988; Tarduno et al., 2021). The pre-existing magnetic field could be that of a core-dynamo, an ancient version of the geomagnetic field, the solar nebula, or the solar wind (also referred to as the interplanetary magnetic field, IMF) (e.g., Hood and Vickery, 1984).

A full understanding on the processes underlying the Moon's magnetic field is key to unraveling its history and evolution. Moreover, it would provide valuable insights into Earth's dynamics and the broader evolution of our planetary system.

There are three different ways contributing to the understanding of lunar magnetization:

- **Observations**: data collected by magnetometers onboard satellites or carried by landers/rovers at the surface;
- **Sample studies**: paleomagnetic analysis in controlled laboratory environment of lunar samples collected during in situ exploration missions;
- **Modeling and simulations**: focusing on dynamo generation and impact-related processes.

The following subsections will present key investigations and findings from previous studies on the origin of crustal magnetization, divided by different methodologies employed. Each approach will be examined in terms of the theories it supports, its strengths, and main drawbacks.

1.3.1. Contribution from sample studies (through paleomagnetism)

Experimental laboratory analyses of lunar rocks have been made possible using samples brought back mainly through the Apollo program (Zeigler et al., 2019). Apollo 11 was the first mission to recover around 21.6 kg of rocks and soil, and an increasing amount was collected in the following manned missions (Apollo 12 and 14 with around 40 kg each, Apollo 15, 16 and 17 with 77 kg, 95 kg and 110 kg, respectively). Rocks were retrieved from the surroundings of the landing spots (thus in the equatorial region on the Moon) from an initial depth of 15 cm, to 70 cm, up to 3 m in the last missions (see Figure 1.2 for the exact locations). The Luna missions contributed with a few hundred grams of mostly surficial material.

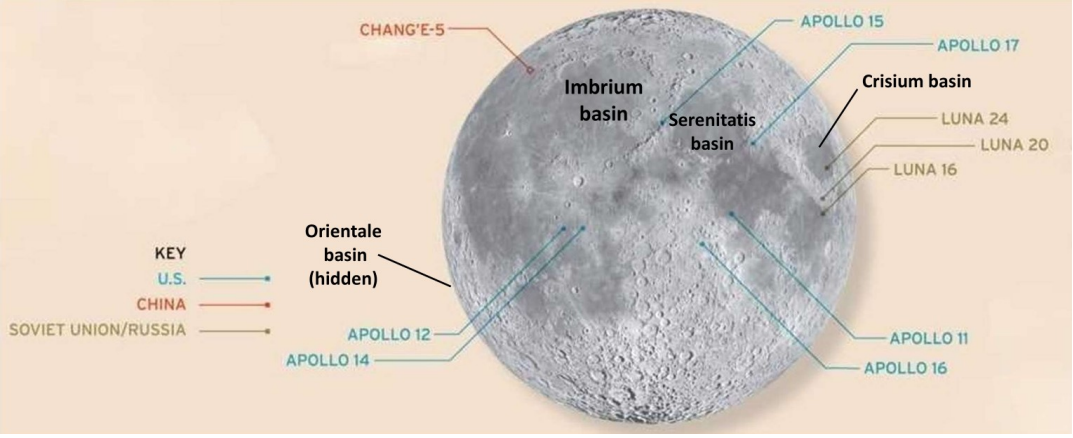

Figure 1.2: Map showing the location of every lunar sample successfully collected and sent back to Earth. Figure adapted from the Planetary Society website.

The past ambient magnetic field of the Moon can be assessed through **paleomagnetic studies** on lunar rock samples. Paleomagnetism is the investigation of a planet's historical magnetic field by analyzing its record in rocks. Defining the orientation of the magnetic carrier magnetization and obtaining the intensity of the recorded magnetization are both valid ways to constrain the origin of the field that magnetized the lunar crust. This process is coupled with radiometric dating techniques to get the age of the rocks. Typically, paleomagnetic studies retrieve both the direction and intensity of the ambient magnetic field when the rock cooled down under the Curie temperature. However, since the Apollo samples were taken without any reference orientation, it's not been possible to recover the direction of the ambient field. Nevertheless, initial measurements of the Apollo samples showed how they recorded high intensity ambient fields — similar to Earth's field intensities — between $\sim$3.9 Gyrs and $\sim$3.7 Gyrs ago, followed by a steady decline in the magnitudes, ending around $\sim$3.2 Gyrs ago (Runcorn, 1983). These early findings are in favor of the core-dynamo theory as: the high magnetization of the magnetic carriers observed is comparable to the current values for the geomagnetic field, powered by a core-dynamo; the sustained duration of the field indicates a long-lived magnetic source.

Concerns about sample contamination, the potential influence of impact-generated transient magnetic fields on the record magnetization of the sample, and the poorly constrained ages of magnetization prevented to reach final conclusions. Starting in the 2000s, renewed interest in paleomagnetic studies, driven by advances in laboratory techniques, sought to address these challenges and push the research forward. The lunar dynamo was proposed to have existed between $\sim$4.25 Gyrs until it stopped between $\sim$1.92 and $\sim$0.80 Gyrs ago (Cournède et al., 2012; Garrick-Bethell et al., 2009, 2017; Shea et al., 2012; Suavet et al., 2013). Standing out from the plethora of investigations, Tikoo et al. (2017) analyzed a young (1.45$\pm$0.45 Gyrs, age study from Mighani et al., 2020) impact melt glass in a regolith breccia, to which ambient field intensities of $\sim$5 μT (low but not null) were associated. This result effectively extended the proposed lunar dynamo duration by a minimum of $\sim$1.5 up to $\sim$2.5 Gyrs. A deeper analysis of the end of the lunar dynamo was conducted by Mighani et al. (2020), who found ambient magnetic field values below the threshold of 0.1μT at 0.91$\pm$0.11 Gyrs. Figure 1.3 summarizes the current constraints of intensity and age of the lunar core dynamo, as resulting from paleomagnetic studies.

However, there is some controversy related to these last results, and a number of critiques and weaknesses have been raised regarding the methods and results of the above-mentioned paleointensity studies (Tarduno et al., 2021):

- Paleointensity estimates from the 70s and 80s are difficult to reconcile with dynamo models, as the Moon's small core may not have sustained such strong fields for extended periods.
- Apollo sample collection had limitations: crude methods prevented accurate magnetization direction recovery, drilling techniques may have altered magnetization, and laboratory procedures introduced uncertainties. Moreover, samples were collected from restricted nearside equatorial regions, a limitation improved by the latest missions to the lunar surface.
- Many Apollo samples were impact-generated, meaning shocks, rather than thermal effects, could be responsible for their magnetization.
- Magnetic anomalies lack spatial and temporal coherence, making their connection to a core dynamo uncertain.
- High uncertainties remain regarding the age and intensity of the hypothesized lunar dynamo, with some studies reporting null field intensities (K. Lawrence et al., 2008).

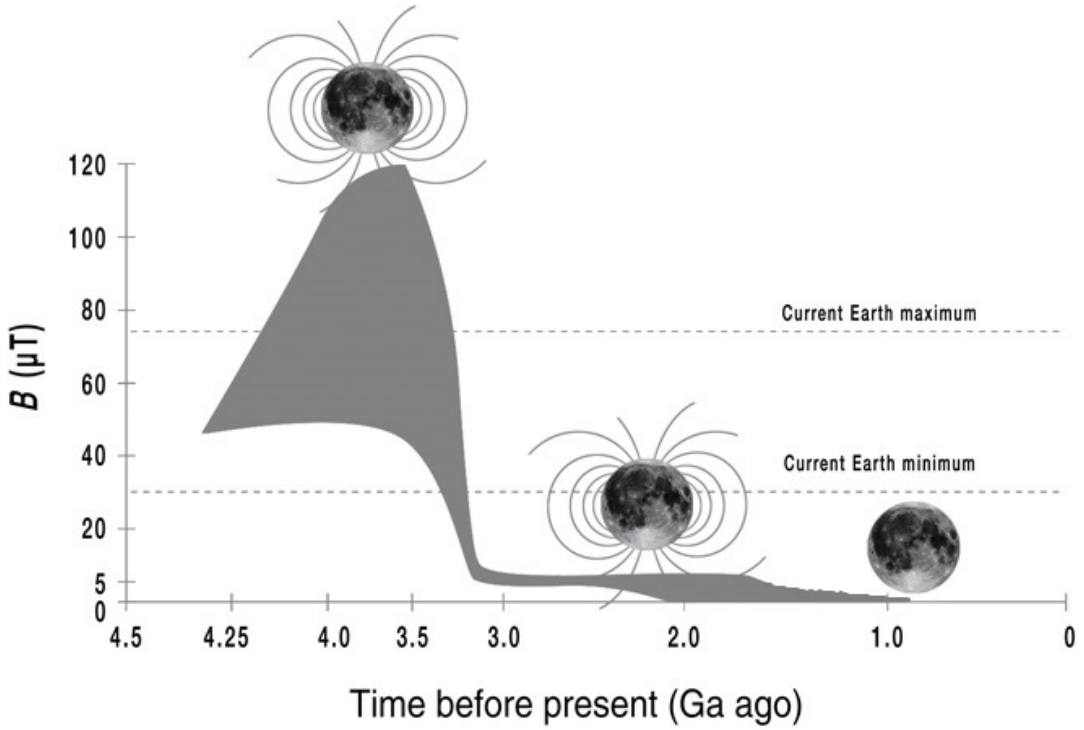

Figure 1.3: Time and intensity estimates of the core dynamo Green et al. (2020), adapted from Mighani et al. (2020).

Recent work from Tarduno et al. (2021) challenges core-dynamo assumptions by demonstrating that: (1) processes other than a dynamo can generate magnetization, and (2) null-field data should not be dismissed as recording failures. A young Apollo glass sample ($\sim$2 Myrs) exhibited strong magnetization despite forming when no core dynamo was expected, undermining the assumption that only a dynamo can produce strong fields. Additionally, five older lunar samples, capable of recording strong fields, showed negligible magnetization, arguing against a long-lived dynamo beyond $\sim$4 Gyrs. Instead, impact-generated fields and shock effects (Gattacceca et al., 2010) may better explain previously reported high paleointensities, as numerical simulations show how impactors <100 m could reproduce these values (Crawford, 2020). This debate could potentially come to an end with the analysis of the new samples acquired after a 50-year gap by the Chinese missions Chang'E 5 and 6 in 2020 and 2024 respectively (NASA NSSDC, 2020 and NASA NSSDC, 2024b). Chang'E 5 samples hold high value due to their young ages ($\sim$2 Gyrs, Qian et al., 2021), while the most recent Chang'E 6 returned rocks represent the first rock samples coming from the lunar far side.

1.3.2. Studies using observations

Studies focused on observations leverage data obtained from magnetometers and electron reflectometers, typically to generate magnetic field maps, either global or regional ones. These observations are essential for understanding the origin of the magnetic sources by analyzing and comparing the data with other datasets, such as topography, gravity and albedo anomalies, to identify potential correlations. Alternatively (and to a lesser and more limited extent), observations can also be used to infer the properties of the ambient magnetic field present when the anomaly source was formed, for example by inferring the paleopole positions. This subsection will present investigations from both perspectives, with the focus set on studies dealing with the location of the magnetic anomalies.

The distribution of magnetic anomalies on the lunar crust is not uniform but rather heterogeneous (see a global map of the lunar magnetic field in Figure 1.4, centered at 0° longitude): the near side, centrally located in the map, exhibits a few strong and isolated magnetic anomalies, some of which are even named. The far side (at the edges of the map) is instead characterized by dense and complex magnetic anomaly formations. Most importantly, the majority of the magnetic anomalies are not correlated with visible geological features, except for a few ones.

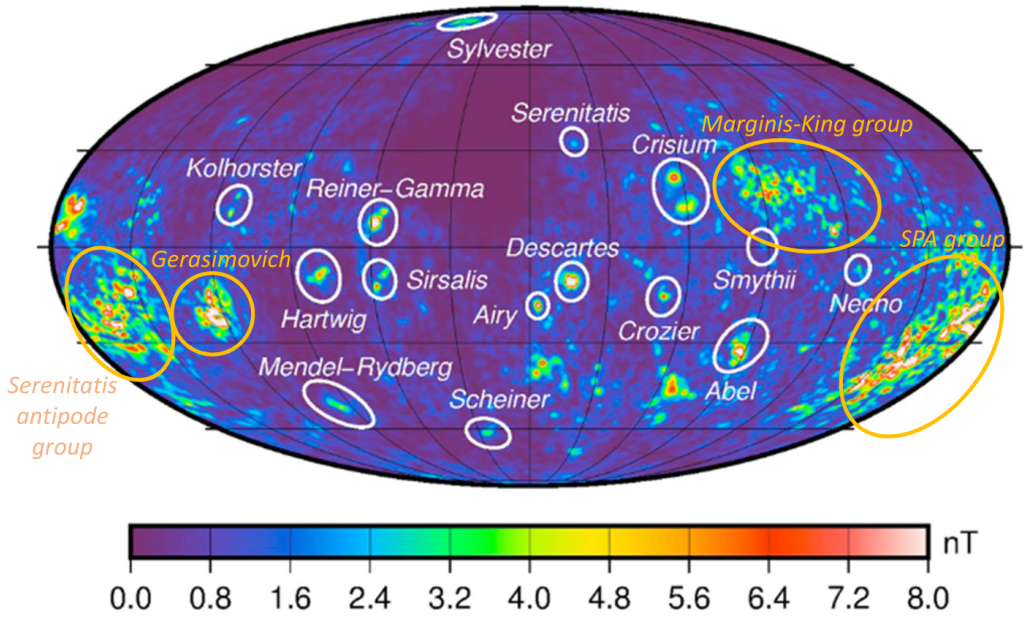

Figure 1.4: Magnetic field strength of the Moon at 30 km altitude from the magnetic model of Tsunakawa et al. (2015). Circled in white are isolated near side anomalies. Circled in orange are major groups of anomalies in the far side. Figure adapted from Oliveira and Wieczorek (2017).

Largest lunar concentration of magnetic signals

The most extensive and intense concentration of magnetic anomalies on the Moon is found on the lunar far side (edges of Figure 1.4). These groups of magnetic anomalies can be identified as: the Marginis-King group in the northern hemisphere, spanning from Mare Marginis to the King crater (approx between 80°-120°E and 0°-30°N); the South Pole — Aitken (SPA) group, in the southern hemisphere (approx between 145°-185°E and 55°S-10°S); the Serenitatis antipode group, west of the SPA group (approx between 185°-215°E and 35°S-5°S); the Gerasimovich anomaly group, more compact and centered at 237°E and 20°S. Far-side magnetic anomalies were investigated with reluctance during the initial stages of lunar magnetism studies, as the far side was less accessible to early missions, resulting in sparser and lower-quality data compared to the near side. This limited the ability to study magnetic anomalies in that region effectively. Two peculiar observations regarding these areas lead to the two main interpretations on its origin. The first observation is that the largest group of anoma-

lies is located just north of the SPA (South Pole — Aitken) basin, one of the oldest and largest impact craters in the Moon, and investigations supporting the association with the SPA basin envision an impact or magmatic origin of the far side anomalies (see Figure 1.5). Wieczorek et al. (2012) for example suggests that this group of strong anomalies (including most of those in the near side) could be the product of the deposition of iron-rich ejecta coming from the SPA impactor, believed to have struck obliquely from the south, which would also explain the elliptical shape of the basin. The second obser-

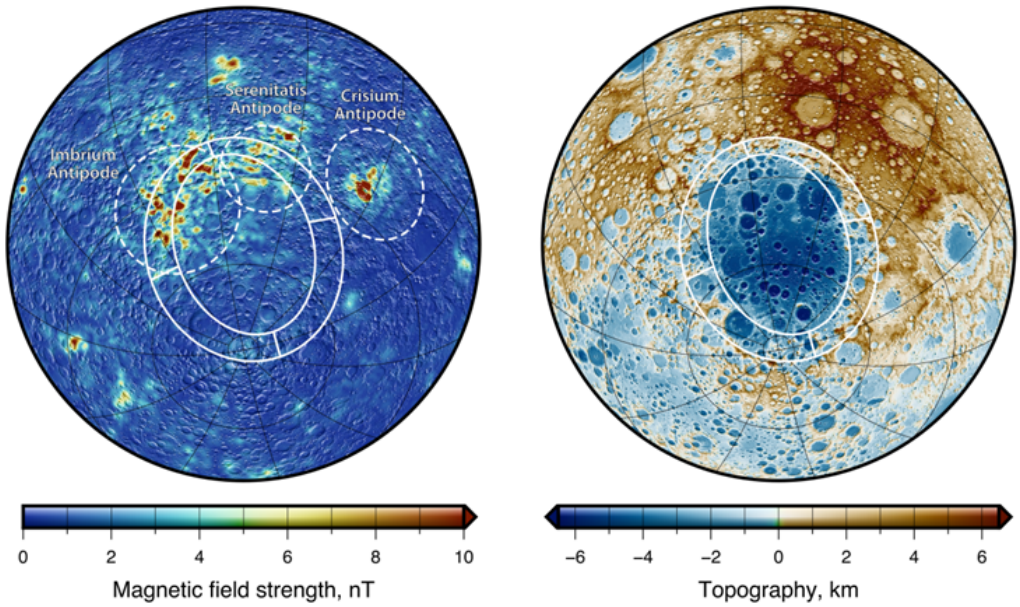

Figure 1.5: Maps of magnetic field strength (left) and topography (right), showing the SPA crater (circled in white, clear in the topography) and the possible impact ejecta nature of the magnetic anomalies (Wieczorek et al., 2012).

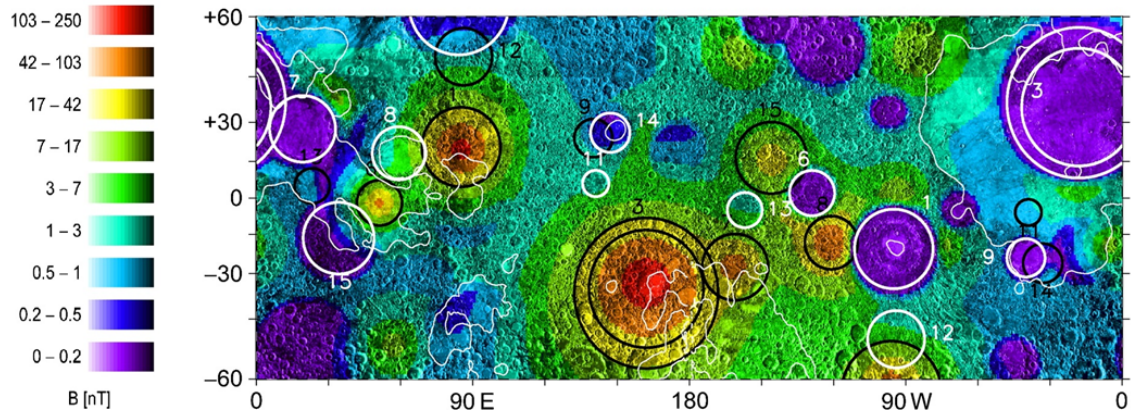

Figure 1.6: Magnetic field strength map of the Moon, highlighting the major nearside impact basins (in white) and the corresponding antipodes to show correlation between the basins and far side magnetic anomalies. Figure taken from Richmond and Hood (2008).

vation is that the four groups of anomalies described above are approximately antipodal to four of the youngest and largest ringed impact basins, namely Orientale, Imbrium, Serenitatis and Crisium (Hood et al., 2013; Lin et al., 1988). This is illustrated in Figure 1.6, where black circles indicate the antipodes of crater rims (shown in white), with numbers corresponding to 1: Orientale, 3: Imbrium, 6: Crisium, and 15: Serenitatis. Studies supporting the view of the anomalies as antipodal to young large basins use impact-field amplification models and findings of unusual terrains at the antipodes (Spudis, 2012) - possibly due to convergence of molten ejecta and/or of seismic waves and/or a plasma cloud (Hood

& Artemieva, 2008; Hood & Vickery, 1984) - to sustain an impact-based origin of the large magnetic anomalies.

Magnetic anomalies related to impact basin melt sheets

Although most anomalies do not show correlation to any geological or geophysical structure, some do, and most of the studies performed focus on anomalies related to the center of impact basin. These anomaly sources are believed to be the result of iron rich material (impact melt) which slowly cooled down under the presence of a steady and long-lived magnetic field, acquiring thermoremanent magnetization (TRM). TRM is a process that a number of scientists interpret as favoring the core-dynamo theory (Arkani-Hamed & Boutin, 2014; Halekas et al., 2003; Hood, 2011). The main reason is given by numerical simulations of impacts, where it is observed how large impactors rise the temperature of the deep subsurface above 1000 K for an extended period of time (Halekas et al., 2003). As the Curie temperature for iron is 770°C, any magnetization existing at the time of the impacts would simply get erased. Slow cooling times following a large impact would require a steady magnetic field to impart magnetization to the subsurface material. It is then a reasonable interpretation to consider anomalies associated to the center of lunar basins and large craters likely generated in the presence of a past core-dynamo. The sources of these magnetic anomalies are probably constituted by "a mix of lunar and iron rich impactor material" found not only beneath the surface but also in the crater's center.

The study of such anomalies can help to reconstruct the possible evolution of the putative core-dynamo and the lunar magnetic field if the associated impact can be linked to a lunar geologic era. The lunar geologic timescale is thus here briefly presented:

- Pre-Nectarian period ($\sim$4.533 to $\sim$3.92 Gyrs): spans from the formation of the lunar crust to the Nectaris impact event.
- Nectarian period ($\sim$3.92 to $\sim$3.85 Gyrs): encompasses the events that occurred between the formation of Nectaris and Imbrium.
- Imbrian period ($\sim$3.85 to $\sim$3.2 Gyrs): divided in early Imbrian, defined as the time period between the formation of Imbrium and Orientale ($\sim$3.85 to $\sim$3.8 Gyrs) and late Imbrian ($\sim$3.8 to $\sim$3.2 Gyrs) which ends with the time at which craters larger than a defined size (D_L) have been almost completely eroded.
- Erastothenian period ($\sim$3.2 to $\sim$1.1 Gyrs): craters of this period show surfaces that haven't been significantly eroded by subsequent impacts, but do not possess a ray system (radial streaks of fine ejecta).
- Copernican period ($\sim$3.2 Gyrs to present): the youngest geological period, presents craters with bright and optically immature ray systems.

Impact basins of Nectarian period such as Moscoviense, Crisium, Mendel-Rydberg, Humboldtianum and Serenitatis, present anomalies in correspondence to their crater center. Basins of Pre-Nectarian age generally display low-magnitude to near-null central anomalies and this can be interpreted in two ways: either younger impact events reprocessed the surface, demagnetizing previously magnetized material, or no ambient magnetic field was present at the time of crater formation, resulting in the absence of any magnetic signal. The three basins of Imbrian period analyzed by Hood (2014) show no detectable central anomalies. This latter result, suggesting a weaker evolution of the core dynamo after the Nectarian age, can be also understood as clashing with the high magnetic field magnitudes inferred by paleointensity estimates for that period. At the same time, this controversy appears weak when considering several factors. First, the sample size of the analyzed Imbrian-aged craters is extremely limited, with only three examples studied (which equals the total number of Imbrian basins existing). Secondly, the presence of a central magnetic anomaly depends strongly on the magnetic susceptibility of the subsurface impact melt and the strength of its magnetization. It is possible that weaker magnetic carriers, bearing lower concentrations of metallic iron-nickel minerals, were produced during the impact — or that the resulting remanent magnetization was not strong and/or stable enough to generate a detectable signal. In both cases, the current magnetic anomaly would be faint or even absent, potentially misleading interpretations. Finally, the Imbrian-aged crater of Imbrium is located within the Procellarum KREEP Terrane (PKT, where KREEP stands for K=Potassium, REE=Rare Earth elements

and P=Phosphorus), possibly too anomalously hot for it to allow for a magnetic signature to exist. Yang and Wieczorek (2024) found that 85% of lunar craters larger than 90 km in diameter do not show any magnetic signature (magnetization or demagnetization). Based on this data, the mechanism of magnetization of central impact melt is likely not a major process in magnetic anomaly formation.

Magnetic anomalies related to impact basin ejecta

The more isolated nature of the near side anomalies, combined with laboratory analyses of rocks collected from areas near major nearside anomalies and an overall greater availability of data compared to the far side, made the lunar near side a straightforward target for early studies of lunar magnetism. Studies of Cayley and Descartes formations, areas in the nearside highlands composed primarily of highland plateau material (perhaps debris from large impact events), indicate how basin ejecta materials are likely the source of the magnetic anomalies related to those two areas (Hood et al., 2001; Richmond et al., 2003). The source of the Reiner-Gamma anomaly, one of the strongest and most peculiar magnetic anomalies and target of the soon-to-launch (end of 2025) Lunar Vertex mission, has been proposed to be Imbrium basin ejecta units (Hood et al., 2001), in light of the fact that it is aligned radially with the center of the Imbrium basin crater. Similarly, Rima Sirsalis, south of Reiner Gamma, has been associated to Imbrium basin ejecta (Hood et al., 2001). Following a new self-created magnetic map that better resolves shapes and distribution of weaker anomalies, Hood, Torres, et al. (2021) expand on the hypothesis that the Imbrium impactor incorporated into ejecta that then deposited in groups radially aligned to the basin, concentrating at the antipode to one of the strongest magnetic anomalies (see Figure 1.7). Monte-Carlo simulations, that estimated the low probability of having these alignments by chance, support the ejecta theory A question yet to be solved is why some ejecta terrains are strongly

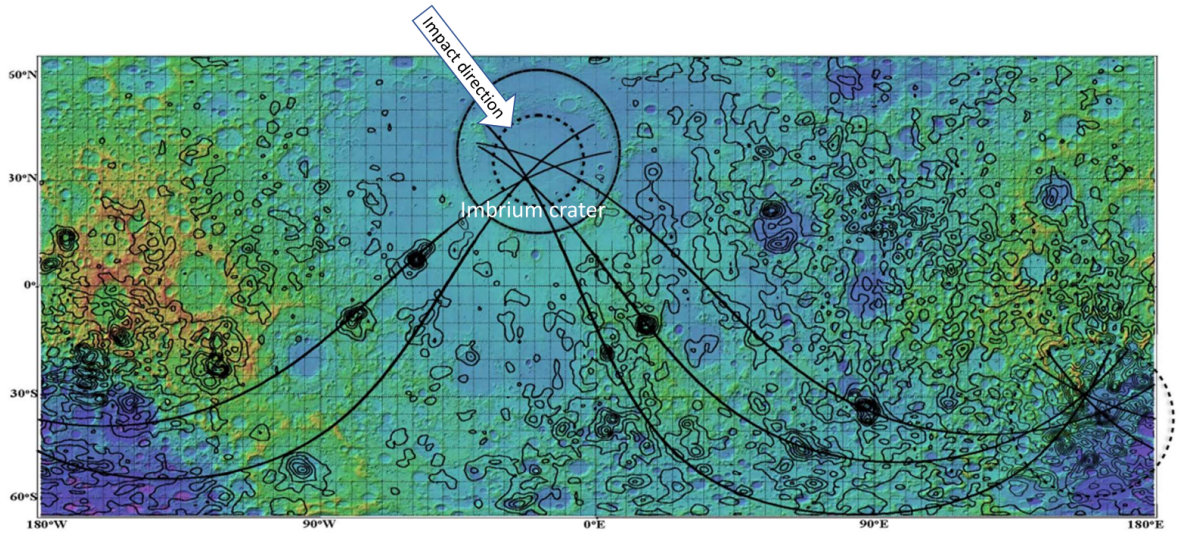

Figure 1.7: The totality of Hood, Torres, et al. (2021) magnetic map with great circle paths extended to the Imbrium antipode zone (large dashed circle). A number of strong, mostly isolated, anomalies are interpreted as basin ejecta unit and appear to be aligned similarly to the proposed circle paths. Imbrium crater is represented through the main rim with the solid black circle line and the inner rim (as interpreted by Neumann et al., 2015. The arrow indicates the proposed impact direction.

magnetized and others are not.

Paleopoles: a particular approach to study the past ambient field

Another category of investigations regards the study of the direction of magnetization and hence the location of the paleopoles, with the aim of uncovering the ancient global lunar magnetic field. The magnetization direction of rock samples cannot be used to constrain the paleopole position, as the original rock orientation is unknown. Instead, paleopoles estimates are retrieved from best-fit magnetization directions resulting from a variety of different approaches, such as methods assuming uniformly

magnetized volumes (Vacquier, 1962), using Surface Vector Mapping (SVM) (Takahashi et al., 2014; Tsunakawa et al., 2015), through DD-CM (defined dipoles, constant magnetization) and GD-VM (gridded dipoles, variable magnetization) inversion algorithms, or through the Parker's method unidirectional discrete model (Oliveira & Wieczorek, 2017). These investigations assume a global dipolar magnetic field to determine the paleopole positions. Depending on whether the paleopoles are clustered in a single region, assumptions are made about the alignment of the magnetic dipole with the spin axis. Multiple attempts to constrain magnetic north pole positions assumed a dipolar field and brought up promising findings when taken singularly, but showed little coherence on the results as a whole. The main takeaways when looking at the studies as a whole are: (1) non-existence of a predominantly dipolar field, (2) no predominant orientation direction for the dipole axis, (3) high variation in time and direction of the field and (4) no universal direction of magnetization of crustal magnetic anomalies (Wieczorek et al., 2023).

Results divide into those that identified a clustering of paleopoles and those which did not. Runcorn (1983) observed three groups of paleopoles, some antipodal to others, supporting a nonrandom view of dipole distribution; Takahashi et al. (2014) detected evidence of two pole clusters, one coinciding with the current spin axis and the other indicating a $\sim$45-60° variation in the spin-axis orientation, supporting a predominantly dipolar geometry of the magnetizing field and a polar wander episode; Oliveira and Wieczorek (2017) showed that the best-constrained paleopoles spanned all latitudes, not identifying a distinct clustering. However, the best-determined paleopoles suggested that the dipole axis may have traced a great circle path along the 90°W and 90°E longitudes. Other investigations instead observed no obvious paleopole clustering, such as the SPA basin-centered study of Nayak et al. (2017), who argues for a modest amount of polar wander experienced by the Moon.

1.3.3. Contribution from numerical modeling

This subsection focuses on studies that make use of mathematical and computational methods to simulate and analyze the magnetic properties and related processes of the Moon.

Core-dynamo power source models

A steady ambient magnetic field at the lunar surface can be generated by a core dynamo. A dynamo is a process that continuously converts kinetic energy into magnetic energy through electromagnetic induction. At first, it was thought that the Moon's core was too small to sustain a dynamo over extended periods. In general, a smaller core has a limited capacity to retain heat, causing it to cool down and crystallize more quickly. Once the core cools sufficiently and begins to solidify, it can no longer support the convective motions necessary to sustain a dynamo, leading to the cessation of the magnetic field.

Several models have been proposed and tested through simulations to assess their potential for generating and sustaining a lunar core dynamo. Here, these models will be briefly presented:

- **Thermal convection**: it rises in the fluid when a sufficiently large temperature difference between the solid mantle and the fluid dynamo region exists, and when certain heat-flux and magnetic Reynolds number related conditions are met. Different variations of a thermal convection driven dynamo have been formulated. The majority of the first thermal evolution models considered a dry mantle: a core-dynamo in these conditions is found to have lasted at most up to 4 Gyrs ago. As more recent studies suggest that water is more abundant in the lunar interior than previously thought (Konrad & Spohn, 1997; Spohn, 2001), core-dynamo models with increased water abundance in the mantle were explored (wet mantle case): the strong effect of water on mantle rheology led to an extended duration of the dynamo up to 2 Gyrs ago (Evans et al., 2014). An alternative direction explored other than water abundance is the presence of a thermally insulating KREEP layer, acting as a blanket and delaying the initiation of the core-dynamo (N. Zhang et al., 2013). A more exotic hypothesis investigated of a possible silicate basal magma ocean found above the metallic core, able to generate a dynamo from 4.2 to 1.6 Gyrs, although with high uncertainties (Scheinberg et al., 2018).

- **Core crystallization**: as the core temperature decreases, solid iron crystallizes, liberating latent heat and light elements. Fluid motion is activated by the rise of light elements if core crystallization occurs at the boundary of the inner core, or by the sinking of the denser iron crystals if it happens at the core-mantle boundary (Q. Williams, 2009). Through this process, a dynamo can be powered. Over the years, various crystallization models have been developed, leading to differing conclusions. However, a common point is shared: a long-lived dynamo is achievable, but it would generate maximum surface field strengths of magnitude lower than approximately 1 μT (Evans et al., 2014; Laneuville et al., 2014), similar in intensity to those produced by thermal convection-powered dynamos.
- **Mechanical forcing**: precession, libration, and changes in rotation rate have been shown to be able to generate a dynamo. Precession refers to the alteration in the orientation of the axis around which a body rotates. A differential motion between mantle and core is established when a liquid lunar core cannot track the precession of the shallower layers, as it is too small (Meyer & Wisdom, 2011). This drives turbulent motions in the core fluid, generating a dynamo. Recent measurement of present-day differential velocity from laser ranging studies are tied to a dissipation rate too small to be able to drive one (J. G. Williams et al., 2001). When the Moon and Earth were closer, higher rotation rates led to larger dissipated power at the core-mantle boundary, generating a dynamo (Dwyer et al., 2011). Contrary to thermally-driven and chemically-driven dynamos, the available power is much higher and able to explain the intensities by paleomagnetic studies. Librations and tides can also act as drivers for the core-mantle differential rotation (Le Bars et al., 2015), especially if instabilities are initiated by impact-induced changes in the lunar rotation. Such a process could have generated short-lived dynamos (Le Bars et al., 2011).

Simulation of post-collision conditions

Besides core dynamo models, simulations of impacts play a crucial role in understanding the effects of impact-derived magnetic fields. These models explore the immediate post-collision conditions, examining the rise in temperature, formation of impact melt, and distribution of ejecta. They also study the propagation of shock and thermal waves, as well as the potential generation and evolution of a partially ionized plasma cloud. The physical process of magnetic field generation and/or amplification (of a pre-

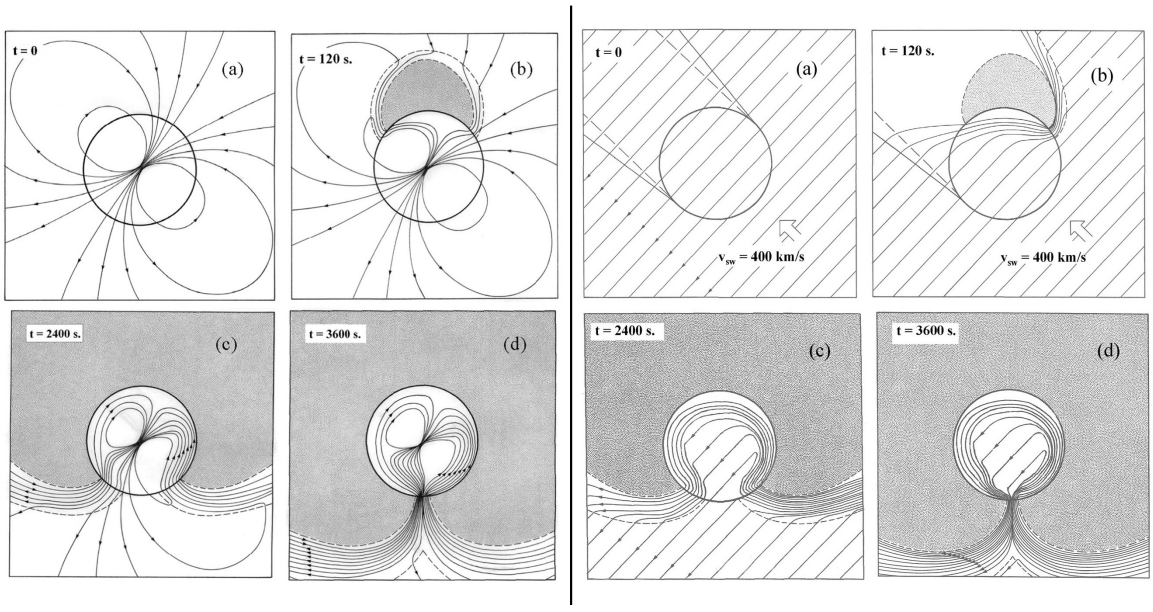

Figure 1.8: Evolution of the partially ionized melt cloud that originates from impacts and consequent intensification of the magnetic field at the antipode. Cases for existing ambient magnetic field of internal origin (dipolar, from a core-dynamo) on the left and of external origin (IMF) on the right (Hood & Artemieva, 2008).

existing one) following hyper-velocity meteoroid impacts have been proposed (e.g., Hood and Vickery, 1984) for the origin of the magnetic field. The simulations performed aim to address or mitigate the challenges posed by the core-dynamo theory, particularly the low paleomagnetic field estimates that

arise due to the Moon's small core size. The study of Hood and Vickery (1984) shows how a partially ionized vapor melt cloud is produced by large impact events which then thermally expands around the Moon and interacts strongly with any ambient magnetic field, temporarily enhancing it (range of 10^2 to 10^4 s). Impact events could thus act as magnitude multipliers for the weak fields generated through the thermal and/or core-crystallization dynamo models and act together in producing a high Earth-like intensity for the magnetic field. Such generated transient magnetic fields are found to present the strongest intensities at the impact antipodes, (Gattacceca et al., 2010; Hood & Artemieva, 2008) and the process represents a possible interpretation of the far side magnetic anomalies (Figure 1.8 shows such simulations from Hood and Artemieva, 2008). Most importantly, such a mechanism could also produce a magnetic field without amplifying an internal pre-existing one but by concentrating at the antipodes the magnetic field lines of the solar wind (thus acting on the IMF), as shown in Figure 1.8 on the right. Other proposed non-dynamo sources for the Moon's magnetic field include that of an ancient Earth and the solar nebula. However, by 3.56 Gyrs ago, the solar nebula had already dissipated (Wang et al., 2017), and the Earth's magnetic field, even at its Roche limit, would have been no stronger than a weak 1 μT, making these two alternative non-dynamo sources highly unlikely to be involved.

Oran et al. (2020) implemented magneto-hydrodynamic and impact simulations for the case of a non-dynamo source for the ambient magnetic field (e.g., the IMF) and found that losses by ohmic dissipation strongly limit the largest magnitude achievable through the ionized-vapor melt model, obtaining magnetic field enhancements that are 2 or 3 orders of magnitude too small and too short-lived to successfully explain antipodal magnetization. The strongest compressed fields didn't reach the crust in the simulations but were instead pushed away. The takeaway message from Oran et al. (2020) is that amplification of IMF through the plasma cloud cannot explain the strong fields recorded through paleomagnetic sources. A companion study by Narrett et al. (2024), which explored the alternative hypothesis that the Moon's magnetization was caused by impact-generated plasmas enhancing a weak ($1\mu T$) core-dynamo magnetic field, used the same MHD code. The study successfully demonstrated that ambient field intensities were compatible with those required to magnetize the analyzed samples.

All in all, numerical modeling studies cannot exactly point to what process or processes generated the crustal magnetic fields we observe today on the lunar surface. In particular, most core-dynamo power source models (physical and numerical) cannot explain the high intensities ambient magnetic fields obtained studying samples, while the simulation of post-collision conditions, focusing mainly on modeling the generation of transient magnetic fields, faces challenges due to the difficulty to accurately reproduce the impact conditions.

1.4. Presentation of the project

1.4.1. Identification of the Scientific Gap and Aim of the Project

As of today, the origin of the magnetic field under which the lunar magnetic anomalies were formed is not clear. As understood from the previous sections, there is no clear hypothesis to explain all observations and laboratory experiments. To summarize the current status of studies on lunar magnetism, the high paleointensities recorded by the lunar samples as found by laboratory studies cannot be reproduced by simulations with the currently proposed physical models for a core-dynamo power source, differing by more than one order of magnitude. Studies using observations cannot find evident correlations for the magnetic anomalies with any geological structure or geophysical process. Physical models and simulations looking at the alternative hypothesis of a mainly transient origin of the magnetic fields also struggle to find a viable physical process that combines the production of a strong-enough magnetic field that can also explain the steady intensities inferred from the sample studies. The possibility of a weak core-dynamo magnetic transiently enhanced has not been extensively explored.

Since this project is based on observational data, specifically magnetic measurements from the latest missions (Kaguya and Lunar Prospector), a scientific gap in the current state of this category of investigations lies in the limited exploration of magnetic anomalies as selected randomly. Most of the studies conducted so far rely on the available regional geological and geophysical context, attempting

to correlate magnetic data with gravity data, topography, or albedo anomalies. For example, Hemingway and Tikoo (2018) and Garrick Bethell and Kelley (2019) use the morphology of lunar albedo anomalies (swirls) as proxy for the structure of subsurface sources of magnetic fields. Kelley and Garrick-Bethell (2020) instead, focusing on the Reiner Gamma anomaly, explores its correlation with a negative Bouguer gravity anomaly, interpreting the anomaly to be a buried impact crater. Topography structures such as impact basins are the focus of Oliveira et al. (2017a), focused on pinpointing the locations of magnetized melt sheets and constraining the iron content.

This project aims to extend the current observational studies, in which only targets related to geological and geophysical structures are analyzed. This analysis includes previously unexplored anomalies randomly selected despite their geological/geophysical context, offering a more unbiased investigation of the lunar magnetic field. In order to do that, a methodology able to retrieve the source of magnetization that is not tied to any information other than the observed magnetic field is implemented. The Parker inversion represents such an approach: it allows estimating the strength and location of a set of surface magnetic dipoles that best fit a local set of magnetic data, under the assumption of a limited complexity of the magnetic sources, particularly assuming unidirectional magnetization. In particular, determining the magnetization location, one of the main products of this inversion method, can be key to understand the geological process originating the magnetic anomalies sources. The assessment of whether the method could retrieve and constrain the surface spatial distribution of the sources of magnetization without any a priori information regarding their location or geometry had not been carried out until Oliveira et al. (2024). Their analysis of the performance of the method tested how accurately the inverted surface dipoles match the 2D surface projection of magnetized subsurface synthetic geometries, which mimics geological structures found in the crust interior. Results proved that Parker's method correctly delineates the magnetized material, indicating that it is suitable for an extensive application on a diverse pool of anomalies on the Moon. By adopting the Parker's inversion method, this project represents the first study to widely apply such method with the aim to constrain the location of the sources of the magnetic anomalies.

The research question under which the project is conducted is straightforward:

What is the origin of lunar magnetic anomalies, and what are the implications for lunar evolution?

The areas of focus of this project are here presented in the form of sub-questions to the research question:

1. **Do magnetic anomalies have an impact-related origin?** This broad question is addressed by examining whether the best-fit distribution, strength, and orientation of surface magnetic dipoles can be explained by:
    - An ejecta origin –> the radial alignment of the anomalies with large and young impact events is assessed
    - An antipodal origin –> the correlation between the antipodes of large and young impact basins and the surface distribution of the magnetic dipoles is explored

    Additionally, this study assesses the plausibility of an impact-related origin in the presence or absence of a core dynamo, building upon and extending the investigations of Hood and Vickery (1984), Hood et al. (2001), Hood and Artemieva (2008), and Hood, Torres, et al. (2021).
2. **Are lunar albedo anomalies (swirls) delineating magnetized material?** These mysterious surface features are believed to be strongly connected to magnetic anomalies. This is well observed in magnetic maps, but the correlation with surface magnetization hasn't yet been proven. Thus, the Parker's method output is an important tool to confirm the validity of the hypothesis.

1.4.2. Project plan

The project plan and its foundational building blocks are illustrated in the Gantt chart. The initial months of the project focused on laying the groundwork, including the conduction of the literature review, gaining familiarity with the state of the art in lunar magnetism, and understanding the background of the

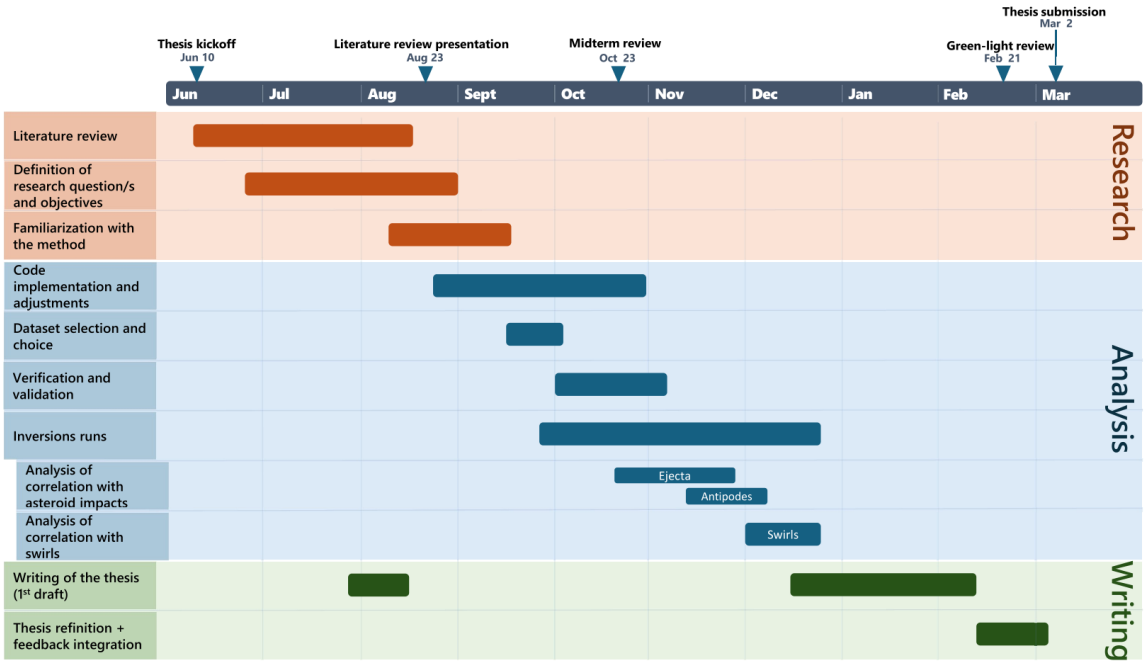

Figure 1.9: Gantt chart showing the project tasks and the predicted temporal allocation for each.

Parker Inversion technique. The definition of objectives and research questions was treated as an iterative process that extended beyond the literature review. Refinements to the research questions were anticipated to happen even during the early stages of the analysis phase. The Analysis phase began with the implementation of the Fortran code for the Parker Inversion method and successive development of a Python code for output visualization, as well as comparing basic results with those of Oliveira et al., 2024, from which the primary Fortran code was derived. The dataset selection process was crucial for identifying the most appropriate magnetic maps. Once these two components were established, the inversion runs began, targeting anomalies of locations and sizes within the capabilities of the Parker Inversion method, while also testing scenarios beyond its typical application range. The two primary focuses of the analysis, namely the correlation of the output with asteroid impacts (ejecta alignment and antipodes) and with lunar swirls, were independent of one another, allowing flexibility in their temporal organization. Although figure 1.9 presents these tasks sequentially, they could have been conducted in reverse order without affecting the workflow. To ensure sufficient time for thesis writing, the Introduction and Literature Review sections were drafted towards the end of the Research phase, while the majority of the writing took place in the latter stages of the project. A complete thesis draft was prepared two weeks before the submission deadline to allow time for the Green-light review, after which any provided feedback were implemented.

1.4.3. Structure of the report

The thesis is structured into eight main chapters. The current chapter has provided a comprehensive introduction to the topic, outlining the state of the art in lunar magnetism, identifying the scientific gap that this project aims to address, and presenting the project's objectives. Chapters 2 and 3 cover the theoretical background and the datasets used, respectively. Chapter 4 explains the methods, detailing the algorithm and its implementation, followed by Chapter 5, which focuses on verification and validation to support the results. Chapters 6 and 7 are dedicated to presenting the results, along with their analysis

and discussion. Finally, Chapter 8 concludes the thesis with a summary of the findings and suggestions for future research.

2

Theoretical Background

2.1. Magnetism: From Fundamental Forces to Planetary Magnetism

The concept of magnetism has fascinated scientists for centuries, with its mysterious ability to influence objects at a distance. It was the French physicist André-Marie Ampère who first proposed that magnetic fields are produced by the motion of electrical charges. In late 1820, at the Paris Academy of Sciences, Ampère presented his reflections on the equivalence between magnets and electric currents, revolutionizing the understanding of magnetism. His groundbreaking work led to the formulation of Ampère's Circuital Law, later generalized by Maxwell in the Ampère-Maxwell law (Garg, 2012), which mathematically describes the relationship between an electric current and the magnetic field it generates (Ampère´s reflections are collected in Ampère, 1825). In its integral form, the law states:

$$\oint_C B \cdot d\ell = \mu_0 I_{\text{enc}} \tag{2.1}$$

where:

- $\oint_C B \cdot d\ell$ represents the circulation of the magnetic field B along a closed path C
- μ_0 is the permeability of free space
- I_{enc} is the total current enclosed by the loop

Ampère's insights quickly extended beyond simple magnets to larger systems. By 1822, he hypothesized that Earth's magnetic field was generated by electric currents within its internal layers. However, the mechanism behind these currents remained uncertain for over a century. In 1919, Joseph Larmor proposed a core-dynamo, a novel concept, to explain the Sun's magnetic field (Larmor, 1919): he suggested that a rotating, convecting, and electrically conductive fluid could sustain a magnetic field over time. Initially met with skepticism, the theory gained traction and was later adapted to Earth with modifications based on studies in secular variation, paleomagnetism, seismology, elemental composition, and Gauss's theories. The dynamo theory requires three key components: an electrically conductive fluid, convective motion generating electric currents, and a rotational mechanism, such as the Coriolis effect, to organize these currents into a coherent magnetic field (see Figure 2.1). In Earth's case, the liquid iron and nickel in the outer core serve as the conductive fluid, while heat from the inner core's crystallization drives convection. The planet's rotation, through the Coriolis effect, aligns these convective currents, sustaining Earth's dipolar magnetic field.

The dynamo theory was soon extended to other planets and celestial bodies. Space missions and magnetic field observations suggested the probable existence of active dynamos in planets such as Jupiter (through the Pioneer 10 mission), Saturn (through the Pioneer 11 mission), and Mercury

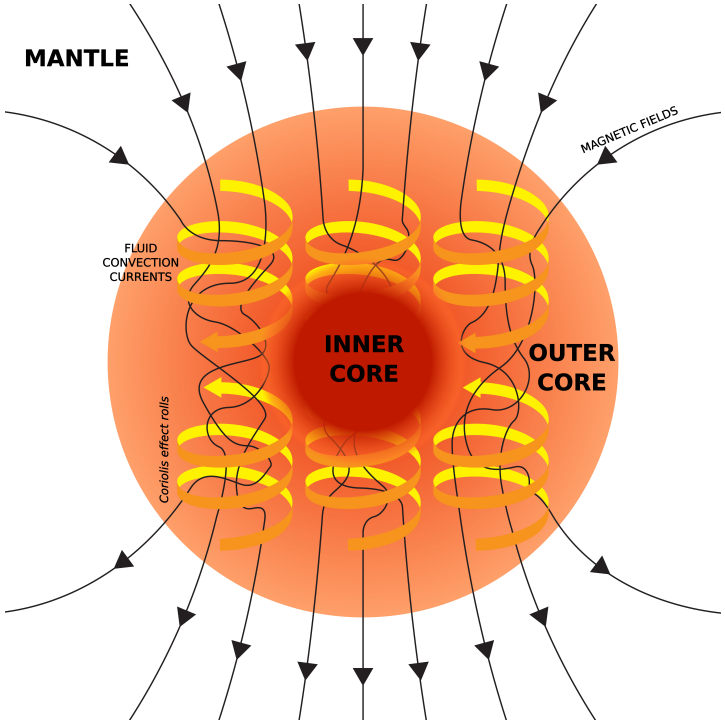

Figure 2.1: Illustration of the dynamo mechanism (strata size is relative to the Earth case): convection currents of fluid metal in the outer core, driven by heat flow from the inner core, generate circulating electric currents, which supports the magnetic field. By Andrew Z. Colvin - own work

(through the Mariner 10 mission). For instance, Jupiter and Saturn exhibit strong magnetic fields, consistent with dynamos in their metallic hydrogen layers (first evidence came from radio source studies, respectively in Burke and Franklin, 1955 and Brown, 1975 for Jupiter and Saturn). Mercury, despite its small size, presents a weak but detectable magnetic field. This hints at a partially active dynamo in its core (Ness et al., 1975). Not all celestial bodies exhibit present-day magnetic fields. For example, Venus, despite being similar to Earth in size and composition, lacks a significant magnetic field. Mars, on the other hand, shows remanent magnetization in its crust, indicating that it had a global magnetic field billions of years ago, now extinguished (Acuña et al., 1999).

The Moon stands as a particularly intriguing case: while it lacks a global magnetic field today, lunar rocks returned by the Apollo missions apparently reveal strong remanent magnetization, indicating the Moon perhaps once had a magnetic field as strong as Earth's. One hypothesis for the Moon's ancient magnetism is a dynamo driven by early internal convection when the Moon's core was still molten. Alternatively, impact-induced magnetization from large basin-forming events might have temporarily amplified local magnetic fields. In order to thoroughly understand the investigation here conducted, other concepts of the lunar magnetization (and on magnetism in general will be now presented).

2.2. What are magnetic anomaly and why are they important to study

In the context of the highly heterogeneous lunar magnetic field, a **magnetic anomaly** is a local variation of the magnetic field resulting from differences in the chemical composition or magnetism of rocks. Celestial bodies, whether they currently possess a global magnetic field or not, can exhibit such features. Since this investigation focuses on the Moon, which lacks a global magnetic field but retains a highly heterogeneous crustal magnetization, studying magnetic anomalies is particularly valuable. These anomalies serve as preserved records of ancient magnetic fields, offering insights into the Moon's past dynamo activity. Additionally, they provide crucial information about the composition of the lunar crust

and the effects of impact events, which may have influenced the magnetization patterns observed today.

The term “magnetic anomaly” is extensively used in this work, usually coupled with the name of a known surface feature (e.g., a crater, a mountain, a rille) to refer to a magnetic area of interest. For example, the Reiner-Gamma magnetic anomaly, a widely studied magnetic feature in the lunar near side, owes its name to the nearby Reiner crater, although its presumed origin has no ties with the geological feature. The term “Gamma” instead reflects the established tradition in lunar mapping of using Greek letters to identify smaller or unique features near primary craters.

2.3. Magnetization and Demagnetization

Before explaining how a magnetic anomaly is created, the important concepts of **magnetic moment**, **magnetization** and **magnetic remanence** are presented. The **magnetic moment** $\vec{m}$ is a vector that quantifies an object’s response to an externally applied total magnetic field $\vec{B}$, determining the torque $\vec{\tau}$ it experiences:

$$\vec{\tau} = \vec{m} \times \vec{B} \quad [Am^2] \tag{2.2}$$

In essence, it acts like a “compass needle”, indicating both the strength and direction of the object’s alignment with the magnetic field. The **magnetization** $\vec{M}$ is defined as the vector field expressing the density of magnetic dipole moments $\vec{m}$ (permanent or induced) in a magnetic material.

$$\vec{M} = \frac{d\vec{m}}{dV} \quad [\frac{A}{m}] \tag{2.3}$$

with dV the volume element and $d\vec{m}$ the elementary magnetic moment. The quantity also describes the response of a material to an applied magnetic field and how the material affects and changes the magnetic field. Material becomes magnetized when exposed to an external magnetic field. The subsequent magnetization strength and direction depend on the intrinsic properties of the material: paramagnetism, diamagnetism and ferromagnetism. When subjected to an external magnetic field, compared to the direction of the field, the magnetic moment orientation of the material can be opposite (diamagnetism) or in the same direction (paramagnetism and ferromagnetism). Ferromagnetic materials present a particularly strong magnetization due to a special interaction of the electron spins and become paramagnetic at high temperatures, above a transition temperature, the Curie Temperature. When the external magnetic field is removed, magnetization is partially retained in ferromagnetic material and the remaining magnetization is referred to as **remanent magnetization**.

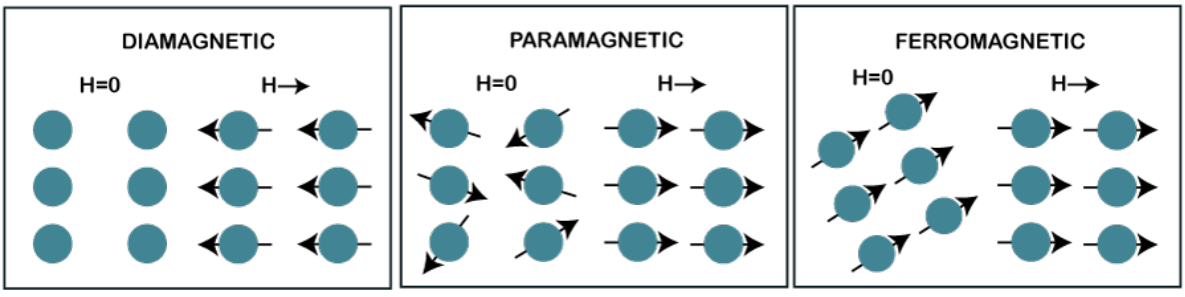

Figure 2.2: Behavior of materials with different intrinsic properties to the presence or absence of the magnetic field strength H. Magnetic remanence for H=0 happens only for the ferromagnetic material case.

Demagnetization, the reduction or elimination of magnetization, can be reached heating rocks above the Curie temperature, easily reached during impact events. Shock demagnetization, in the context of

impacts, is a more complex and less predictable mechanism as it involves multiple interacting factors such as pressure, strain and temperature, and, together with experimental limitations, is lesser understood compared to thermal demagnetization. Now, with the acquired theoretical knowledge on magnetic moment, magnetization & demagnetization, and magnetic remanence, the factors necessary for the formation of a magnetic anomaly are now examined. (Oliveira et al., 2024) states that the following combination of components must exist:

- Presence of magnetic carriers
- Existence of an ambient magnetic field
- Action of a geological mechanism for the carriers to acquire magnetization

Iron-nickel and iron-phosphide minerals (e.g., kamacite, martensite and schreibersite) are the main ferromagnetic carriers for lunar rocks (Rochette et al., 2010) and present grains that form nonuniform magnetic structures in particular vortex states (Wieczorek et al., 2023) which can carry and preserve magnetization for billions of years. Some of these magnetic carriers are of lunar origins, others may instead have been of meteoritical origin.

In regard to the existence of an ambient magnetic field, although the Moon does not currently possess one, its crustal magnetization must have originated from a magnetizing field sometime in its past. The source of this ancient magnetic field has been debated for over fifty years. However, in recent years, growing consensus points towards an ancient, now-extinct core-generated dynamo as the likely cause of a global magnetic field that once magnetized the lunar crust (Dwyer et al., 2011; Laneuville et al., 2014; Wieczorek et al., 2023). However, the alternative theory that suggests that short-lived, impact-generated magnetic fields could also account for some or majority of the lunar magnetization cannot be excluded (Hood & Artemieva, 2008; Tarduno et al., 2021). A thermochemically driven dynamo in the first $\sim$100 Myrs of lunar history is deemed feasible by most because of rapid cooling (Tarduno et al., 2021; Wieczorek, 2018). However, hypotheses diverge regarding the possible mechanisms sustaining the dynamo or the dynamo existence beyond this period.

For the third component, namely the occurrence of a magnetizing event, lunar rocks can acquire Natural Remanent Magnetization (NRM), the permanent magnetism of a rock or sediment, through a variety of processes. Thermal Remanent Magnetization (TRM) occurs when ferromagnetic material cools in the presence of a steady magnetic field. This process can happen during impact events or with volcanic/magmatic activity, for example. When the crust is heated above the Curie Temperature of the magnetic carrier iron (the most abundant), any existing magnetization is lost (demagnetization). As the material then cools down, the magnetic carriers acquire a new magnetization aligned with the ambient magnetic field present during cooling (Hood, 2011; Wieczorek et al., 2012). Subsequent reheating at lower temperatures can impart a partial TRM (pTRM). Laboratory experiments with higher nickel content for the grains, showed that crystal growth contributes to a higher degree - compared to cases with lesser nickel content - to the magnetization of the carriers, contributing to impart a thermochemical TRM. Volcanic and magmatic activity (Hemingway & Tikoo, 2018), are also able to thermochemically alter lunar rocks and produce strong carriers. Hypervelocity impacts can produce Shock Remanent Magnetization (SRM) as a result of shock waves (Gattacceca et al., 2010). Other processes, less desired for subsequent magnetization analysis, can be acquired after sample collection: Isothermal Remanent Magnetization (IRM) is imparted to the carriers if exposed to strong fields (above $1\mu t$) (Garrick-Bethell et al., 2009) while Viscous Remanent Magnetization (VRM) is unavoidably acquired after a long-term exposure to the Earth's magnetic field. Drilling of rock samples for their extraction from the lunar soil or cutting them in the laboratory can also impart pTRM. In general, these contaminating remnants needs to be avoided as they can partially or totally erase older magnetization.

2.4. Properties of lunar crustal magnetism

The Moon displays a highly heterogeneous distribution of magnetic anomalies, with crustal field strengths below 1–2 nT over most of the surface (see the magnetic map from Tsunakawa et al., 2015 at 30 km

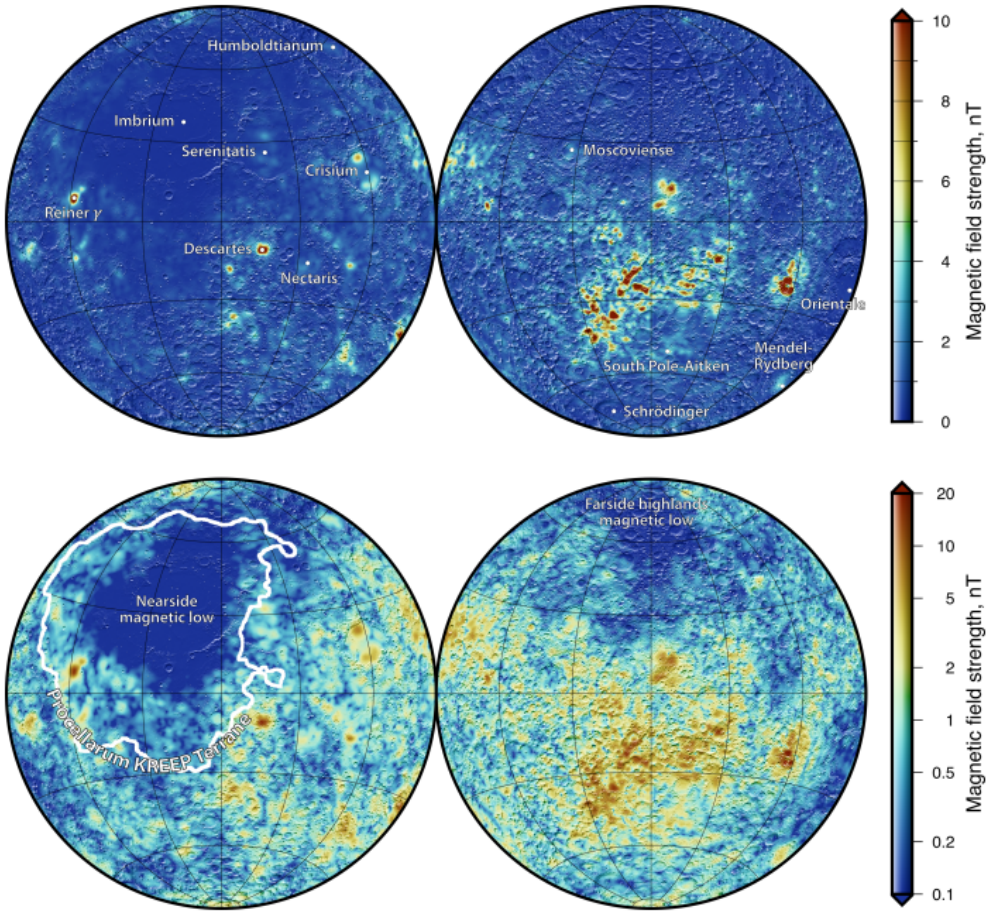

Figure 2.3: Total magnetic field strength of the Moon at 30 km altitude from Tsunakawa et al. (2015) plotted using a linear and logarithmic color scale (respectively, top and bottom). Underlain, a relief map.

altitude shown in Figure 2.3). This is significantly weaker, by tens to hundreds of times, than the crustal field strengths observed on rocky planets like Earth and Mars. There are two regions with exceptionally low magnetic intensities (< 0.1 nT): the nearside magnetic low and the far side highlands magnetic low (as indicated on the map). Additionally, several isolated anomalies with strong magnetic fields are present in both hemispheres, with the highest concentration occurring on the far side. The distribution of high and low magnetization on the Moon's surface reflects its geological history and the evolution of its magnetic field. The generally low magnetization of most of the lunar crust suggests that the Moon's global magnetic field, if it existed, was much weaker and less persistent than Earth's. The isolated areas of high magnetization, particularly on the far side, might point to localized events or processes, like ancient volcanic activity or large impact events, that created or enhanced magnetic anomalies. The areas of exceedingly low magnetic intensity, such as the nearside and far side highlands, could represent regions where the crust is either deficient in magnetic minerals, showing particular composition and thermal evolution (PKT area, delineated in white in figure 2.3), or where any previous magnetization has been erased or never acquired. Despite some anomalies being thought to be correlated with impact basins (either showing up in the inner crater or at the antipodes), volcanic rises, swirl-like albedo markings or other surface expressions, the majority of them shows no correlation with surface geological and geophysical structures or geologic processes. This lack of correlation complicates their interpretation for scientists.

The lunar swirl structure is an objective in this process. A swirl (or albedo anomaly) is characterized by having a high albedo, appearing optically immature (having the optical characteristics of a relatively

young regolith), and (often) showing a sinuous shape. Swirls are though to be heavily linked with magnetic anomalies, with mini-magnetospheres locally generated possibly able to preserve the regolith and slow down maturation (Hood & Schubert, 1980) (see Figure 2.4). Alternative formation models for swirls other than magnetic shielding are cometary impacts (Schultz & Srnka, 1980) and electrostatic (Garrick-Bethell et al., 2011) or magnetic (Pieters et al., 2014) sorting of grains. A review of the state of the art of lunar swirls can be found in Denevi et al. (2016).).

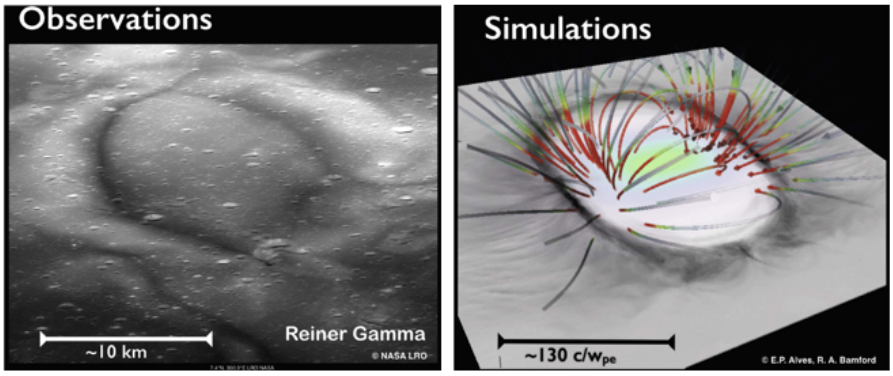

Figure 2.4: Image of the central and widest region of the Reiner Gamma swirl in the left (image from LRO mission, NASA), and in the right a 3D simulation showing the relative proton density from Bamford et al. (2016). The figure wants to show how the magnetic shielding could work.

3

Datasets

This chapter explores how magnetic fields on the Moon are detected and mapped. It starts by presenting the space-borne and surface-borne instruments that measure magnetic fields and briefly explains how they work and the detection process. Then, it looks at how magnetic maps are created from the satellite data collected, with a focus on the importance of selecting quality passes based on plasma conditions to ensure reliable and low-noise results. Finally, it introduces the main magnetic maps developed to date (from Tsunakawa et al., 2015, Ravat et al., 2020 and Hood, Torres, et al., 2021) highlighting their differences and explaining which one was chosen for this project and why. This provides the background needed to understand the data and methods used in the study.

3.1. Magnetic Field Detection: Space- and Surface-Based Methods

Magnetic maps like that in Figure 2.3 are obtained thanks to data acquired in past space missions, such as Magellan, Lunar Prospector and Kaguya. Measuring a planet's magnetic field is a straightforward task for a well-equipped spacecraft: the spacecraft magnetometer is in fact a rather inexpensive, low-weight and easy-to-implement instrument for scientific investigation, generally placed in a boom to minimize magnetic contamination from spacecraft materials. Considering that it can also be used for attitude sensing, it is one of the most widely utilized scientific devices. There are 3 main types of magnetometers: the flux-gate type, the search coil and the ionized vapor magnetometer.

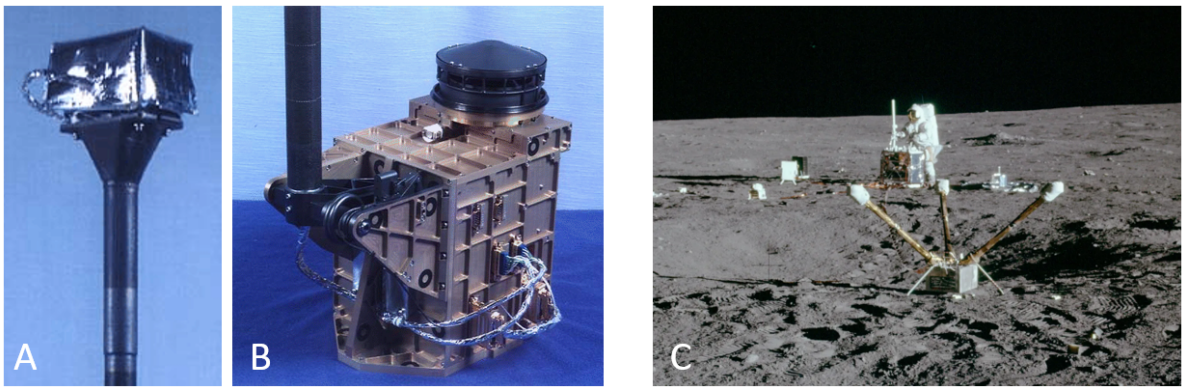

Figure 3.1: Lunar Prospector MAG/ER instrument: FigureA is the magnetometer (MAG) and FigureB is the electron reflectometer. In FigureC in the foreground is the LSM, part of ALSEP. All images from NASA.

A flux-gate magnetometer works similarly to a compass, with an electromagnet used to measure the magnetic field: the working principle relies on capturing the disturbance caused by an external magnetic field to the equilibrium generated by the alternating current (AC) given to a coil wrapped around a ferromagnetic metal. Combining multiple flux-gate sensors in different directions or, alternatively, rotating the spacecraft, the external magnetic field components can be fully described. This instrument can precisely measure weak/static fields and its electronic simplicity, reliability, low weight and low power make it a great choice for the study of planetary fields and long-term space missions. A search coil, or induction magnetometer, operates based on Faraday's law of induction, in which a changing magnetic field generates an electric current in the coil. This makes it particularly well-suited for measuring rapidly changing magnetic fields. Ionized gas magnetometers provide magnetic data with high resolution and accuracy by observing the effects of the field on the energy levels of atoms in gases such a cesium or helium. The optimal instrument suite for a purely scientific point of view would be a combination of the flux-gate and the ionized gas magnetometers. The redundancy is needed for cross calibration purposes, but it is not a realistic choice due to high mass and power constraints.

The last 2 major lunar missions, Lunar Prospector and Kaguya, the magnetic data of which has been used to produce the latest magnetic maps (e.g., Figure4.2 from Tsunakawa et al. (2015)), were both equipped with a triaxial flux-gate magnetometer. Interestingly, Lunar Prospector had another magnetic-oriented instrument in its suite, the electron reflectometer (ER). This is an electrostatic analyzer which measures the energy spectrum and direction (pitch angle) of solar wind electrons reflected from the Moon by its magnetic field. By this, it indirectly studies the surface lunar magnetic field and provides complementary data to the classic magnetometer, despite having limited spatial resolution and accuracy. The MAG/ER (Magnetometer & Electron reflectometer) onboard of Lunar prospector is seen in Figure3.1 (A, B).

Triaxial flux-gate magnetometers record all components of the magnetic field, and the output data turned into map presents positive and negative values depending on the structure of the anomaly and its magnetization direction (e.g., Figure3.2). Figure 3.3 shows how to understand and interpret this dual (negative-positive) nature of the magnetic field component, taking the radial component as example. This can be understood as the spacecraft in orbit detects the mini-magnetosphere generated by magnetized crustal areas. Through the magnetometer, the magnetic field lines are recorded as radially positive when they are "exiting the planet" and as radially negative when they are "entering the planet". Figure 3.3 depicts an artificially generated magnetic anomaly with an arbitrarily chosen direction of magnetization being sensed by a satellite in orbit. Thus, when examining the central region of the Reiner Gamma anomaly, where the radial magnetic field (B_r) is positive in the northern part and negative in the southern part, this pattern suggests that the underlying magnetized material has a magnetic dipole oriented towards the north. By convention, the direction of magnetization is defined as south-to-north (S-N), meaning the magnetic field lines emerge from the northern end of the dipole and re-enter at the southern end (observe in the figure). Such northward orientation explains the radial magnetic pattern of the anomaly. In cases where this positive-negative duality is less evident, with predominantly positive or negative values observed over a specific area, the interpretation suggests a magnetization direction with a strong radial component rather than a tangential one. Specifically, magnetization directed more toward the planet's center corresponds to predominantly negative values, while magnetization directed more away

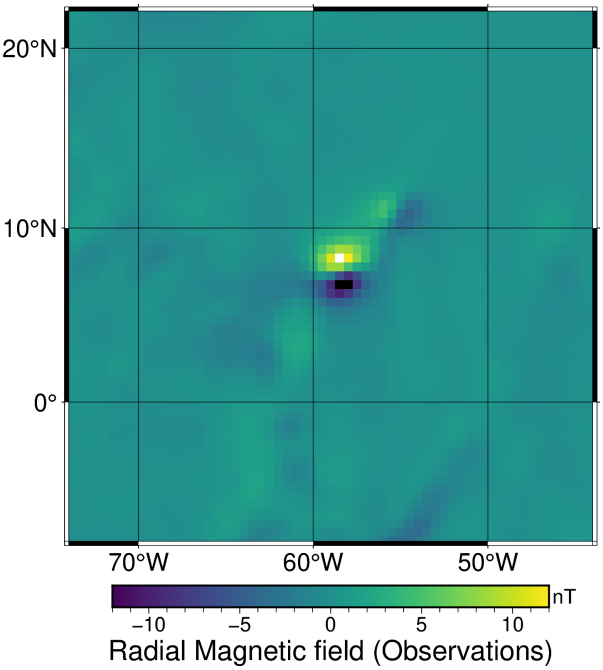

Figure 3.2: Radial magnetic field for the Reiner Gamma magnetic anomaly, using the Tsunakawa map (Tsunakawa et al., 2015)

from the center corresponds to predominantly positive values.

Besides space-born magnetometers, if the mission lands on the planet, there is the chance to equip the lander with a surface magnetometer (which can eventually be deployed on the surface). This is what happened with the Lunar Surface Magnetometer (LSM) experiment, deployed during the Apollo 12, 14 and 16 missions a few hundred kilometers northeast from the strong Descartes magnetic anomaly. Once again a triaxial flux-gate magnetometer was chosen, and it detected a local surface field strength of 32-36 nT likely produced by a nearby localized magnetized body. Clearly unsuited for global mapping, a surface magnetometer can provide for precious surface localized magnetic data with minimal uncertainty compared to the data obtained in altitude from the space-born magnetometers. Figure 3.1-C shows the Lunar Surface Magnetometer (LSM) freshly set up, with astronaut John Young visible in the background near the ALSEP Central Station.

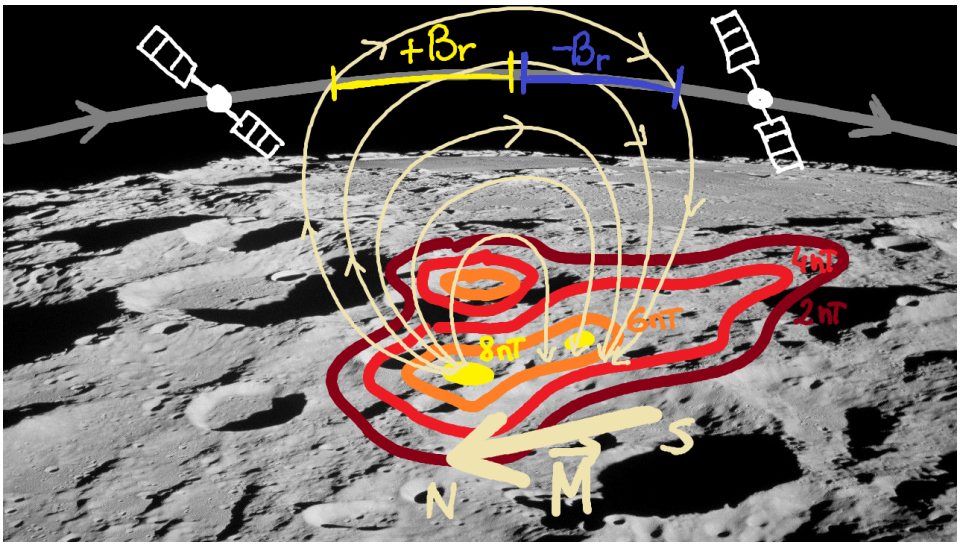

Figure 3.3: A magnetic anomaly is depicted through a contour map with a 2 nT interval, where the magnetization direction (M) generates field lines that exit the North (N) magnetic pole and enter the South (S) magnetic pole. A satellite equipped with a magnetometer records, in this case, first a positive radial magnetic field, followed by a negative radial magnetic field.

3.2. Magnetic maps: data selection & processing

Thanks to the Lunar Prospector and Kaguya missions, comprehensive magnetic field maps with global coverage were produced, offering significant improvements over earlier Apollo data. These missions provided higher resolution, greater sensitivity, and extended observation durations, which were essential for capturing detailed magnetic field variations, including those on the Moon's far side. The resulting maps have been instrumental in refining our understanding of the Moon's crustal magnetization, as demonstrated by works such as Richmond and Hood (2008), Tsunakawa et al. (2015), Ravat et al. (2020), and Hood, Torres, et al. (2021). One of the most recent maps, produced by Tsunakawa et al. (2015), is shown in Figure 2.3, displaying the total magnetic field strength of the Moon at 30 km alti-

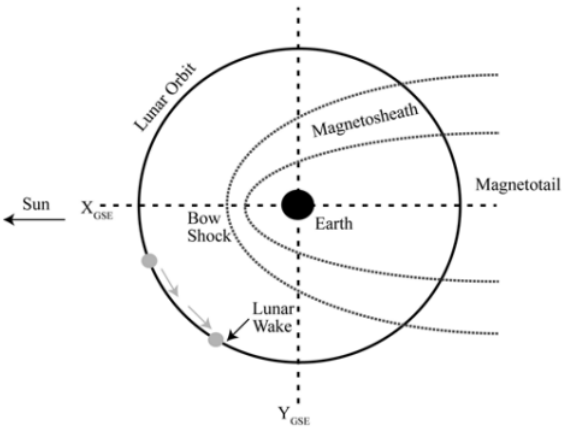

Figure 3.4: Scheme showing the possible positions of the Moon compared to the Earth's magnetosphere (Richmond & Hood, 2008)

tude.

To better understand and interpret such magnetic field maps, it is useful to outline the key steps involved in data selection and processing that contribute to their creation. This process also provides an opportunity to explore the various plasma conditions that arise depending on the relative positions of Moon, Sun, Earth and spacecraft, all of which can significantly impact the magnetic data quality. Information of data selection and processing will follow the method of the investigation by Richmond and Hood (2008), that analyzed LP-MAG (Lunar Prospector - Magellan) data. As a first selection, all low altitude data is taken in consideration, regardless of the relative location of the Moon compared to Earth's magnetosphere and of the spacecraft compared to the Moon. These positions are then cataloged depending on whether the spacecraft is in the night-side, day-side or terminator of the Moon and whether the Moon is in magneto-tail, magneto-sheath or exposed to the solar wind. The plasma conditions of the various types of passes are then analyzed:

- **Quiet plasma conditions**: magnetically quiet external conditions exist when the spacecraft is in the lunar wake or in the geomagnetic tail. Lunar wake creates as the Moon moves through the solar wind, blocking the direct flow of charged particles and creating a "shadow" or void behind itself. This region has significantly lower plasma density compared to the surrounding solar wind and experiences minimal external fields. The geomagnetic tail, or magneto-tail (see Figure3.4), is the elongated extension of the Earth's magnetosphere on the side opposite to the Sun and is formed by the pressure of the solar wind, which stretches the magnetosphere into a long, comet-like tail. Data collected in these 2 conditions, when the spacecraft is in the lunar wake or in the geomagnetic tail, represent the highest quality data, as external fields are largely absent or straight-forwards to remove with post-processing techniques.
- **Magneto-sheath passes**: the magneto-sheath is the boundary layer between the magnetosphere and the interplanetary magnetic field (see detail in Figure3.4). It is a region dominated by rapidly varying and occasionally strong magnetic fields. Because of the complexity of the removal of these fields from the data, such passes are of limited use.
- **Terminator passes**: the lunar terminator is the dividing line between the illuminated day side and the dark night side of the Moon, and terminator passes are considered as those within $\pm 10°$ of lunar dusk and dawn. Halekas et al. (2005) identified a wake boundary signal which, although not strong, alters the magnitude of the crustal anomalies. Comparison between passes can help to detect and remove this unwanted signal.
- **Day-side, solar wind passes**: under such conditions, the interacting fields become the interplanetary magnetic field IMF (which can be removed by visual editing), transient field of solar origin (also removable) and solar wind effects (these cannot be removed). The latter have been shown to interact with crustal anomalies, amplifying or changing the direction of magnetization of the field of interest (Harnett & Winglee, 2003). Due to the limited accuracy on strength and location that such interactions cause, day-side passes cannot be used when constructing a magnetic global map.

From the restricted number of passes selected to construct a magnetic field map, a number of post processes needs to be performed: long-wavelength and short-period external fields need to be removed, the former through a detrending process and the latter by visually examining the passes and identifying measurements that do not repeat on adjacent passes. Finally, altitude continuation needs to be ensured, as altitude of the data varies from different passes.

3.3. Comparison of the Latest Magnetic Maps: Selection and Application for This Project

To date, the main magnetic maps available for use are those generated from the works of Tsunakawa et al. (2015), Ravat et al. (2020) and Hood, Torres, et al. (2021). For simplicity, these maps are here called the Tsunakawa map, the Ravat map and the Hood map. Let's now briefly present the 3 maps and the different methods used to produce them.

The Tsunakawa map implements the Surface Vector Mapping (SVM) method to produce a 3-component global magnetic map at surface height using data from Kaguya and Lunar Prospector from 10 to 45 km altitude. The SVM method divides the Moon into 230 regions and maps magnetic anomalies in each, assuming a constant trade-off parameter u^2 to balance data fit and model smoothness. u^2 is a sort of regularization parameter to optimize spatial resolution. A spherical harmonic expansion then refines u^2 values across the surface. Using these updated values, the anomalies are re-mapped, and the regional maps are combined into a seamless global map of the Moon's magnetic field, showing all three components. Figure 3.5 shows various important parameters for the SVM process: in (a) is the division in regions of the Lunar surface and the distribution of height of sensing of magnetic data (average height of data from passes in that area), on which the global map resolution strongly depends; in (b) the estimated errors of the radial component at surface, with a peak of 4.3 nT, and in (c) the distribution of the trade-off parameter u^2 used for global mapping, which is evidently altitude-dependent. The final global Tsunakawa magnetic map upwards continued at 30 km height for comparison purposes is shown in Figure3.6 (above), along with a zoom-in on the Reiner Gamma region for later discussions.

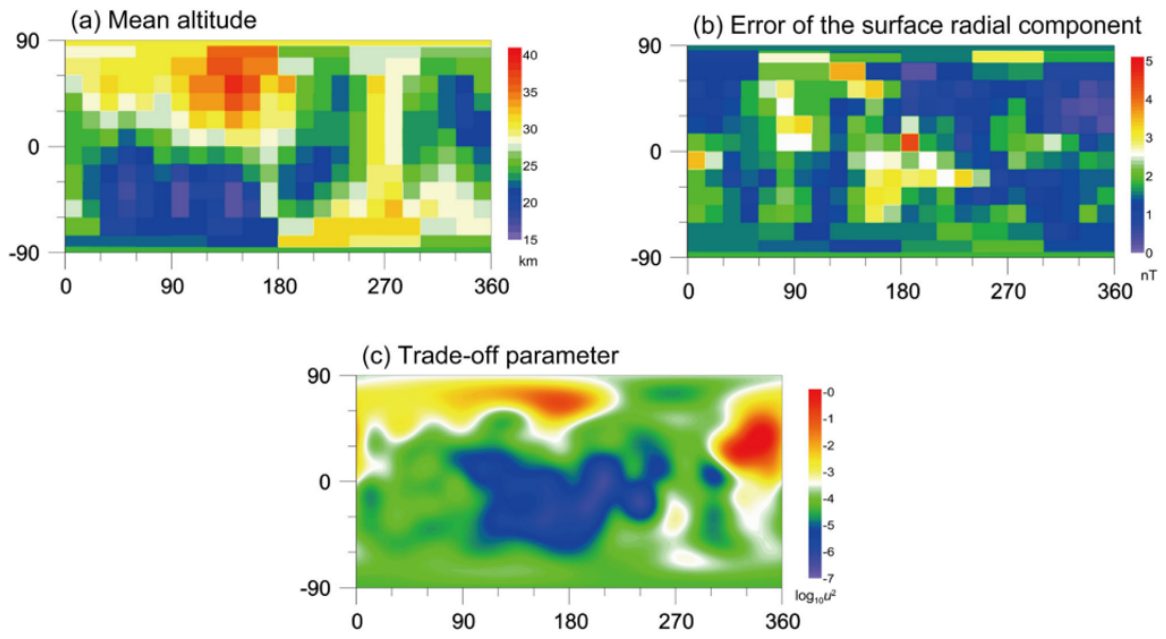

Figure 3.5: Mean altitude, error of the surface radial component and trade-off parameter for the Tsunakawa map

Ravat et al., 2020 create a high-resolution global magnetic field map by leveraging monopole bases, L1-norm regularization, and along-track magnetic field differences using mainly Lunar Prospector highest-quality data. Analyzing the key features of the method, the L1-norm regularization is applied to the surface $|B_r|$ component, and it constrains the model by enforcing sparsity in the solution, meaning that only the most significant magnetic sources are retained, which is particularly suitable and efficient when applied to the Moon's localized magnetic anomalies. The use of monopoles allows creating a denser surface grid compared to using dipoles: this improves the spatial resolution of the model and the ability to detect fine-scale features. Using along-track magnetic field differences instead of relying on full vector magnetic observations simplifies the data processing and also helps filter out noise from external fields. The output map is shown in Figure3.6 (center).

Finally, Hood map, the most recent among the 3, is a large-scale (not global) map of the crustal magnetic fields at 30 km altitude. It ranges from the latitudes 65°S to 65°N, thus not mapping the poles, and uses high-quality data from the Lunar Prospector and Kaguya missions. The focus is placed on obtaining a better representation of weaker anomalies, some of which never mapped before, as can be appreciated from the map's representation in Figure3.6 (below) especially in the near side, but admittedly the map does not always accurately depict stronger magnetic anomalies. Such map is created by

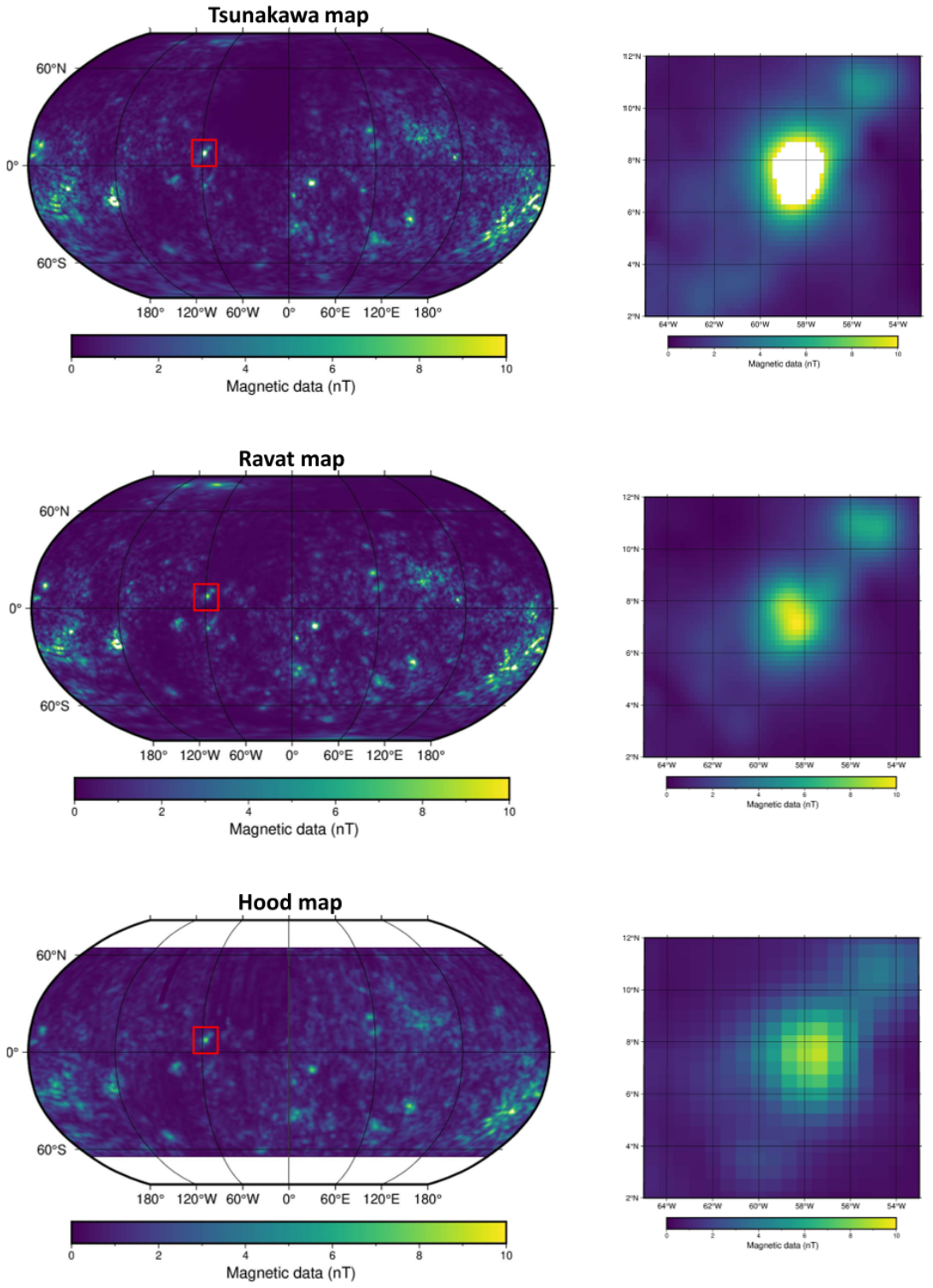

Figure 3.6: Large-scale magnetic maps of the lunar crustal field, upward continued to 30 km, are shown for comparison purposes, along with a zoom-in on the Reiner Gamma anomaly. From top to bottom, the maps are derived from Tsunakawa (2015), Ravat (2021), and Hood (2021). All three maps use a uniform magnetic field intensity scale of 0–10 nT. Notably, the Tsunakawa map displays the highest intensity values, while the Hood map exhibits more conservative values, with overall lower field strengths.

applying an improved and more refined (compared to the other 2 maps) data selection method tailored to specific regions, followed by altitude normalization through the ESD technique. The latter assumes

that the surface magnetic field can be represented with a grid of point-dipoles distributed on a spherical surface and with a defined orientation, separation, and depth. Iterative adjustment of the amplitudes of the dipoles is performed until a minimum variance between model and observations is achieved (see Figure3.6 for the magnetic map with the best-fit results).

The three most recent magnetic maps have been presented. A reference map must now be selected to be used in the majority of the inversions, as conducting inversions with all the maps is neither practical nor feasible within the given time constraints of the project. A number of tools are used to help in the choice, such as:

- maps of the difference in the intensity of the (total) magnetic field at 30 km altitude (difference maps considered are Ravat - Tsunakawa, Ravat - Hood and Tsunakawa - Hood), found in FigureA.1 in the appendix;
- comparison between maps as laid out by the 2 more recent papers, Ravat et al. (2020) and Hood, Torres, et al. (2021): the former compares the Ravat and Tsunakawa maps, while the latter provides a brief comparison of all 3;
- magnetic field profiles at various latitudes;
- comparison of the correlation with the swirl distribution map from Denevi et al., 2016.

A key limitation that immediately renders one of the three maps unsuitable for global use is the lack of pole coverage in the Hood map. Since the poles are one of the main areas of interest for this work, the Hood map's restricted range of 65°S to 65°N is insufficient for the project's needs. Moreover, as the well-represented weak magnetic anomalies are not the preferred target for the Parker inversion method due to a low signal-to-noise ratio, the advantages, and novelties that the Hood map brings wouldn't be exploited, while the weak points would instead be put to light: as discussed in Hood, Torres, et al. (2021), when compared to the Tsunakawa map, in some areas this latter one more accurately depicts the true amplitude of magnetic anomalies. This is the case for the Gerasimovich anomaly for example, the strongest single magnetic anomaly on the Moon: the profiles of the total magnetic field (in nT) for the Hood and Tsunakawa map can be seen in Figure 3.7-c. Moreover, the unfiltered Tsunakawa map possesses a better spatial resolution compared to Hood map. Finally, looking at profiles for a number of other important magnetic anomalies, a rather strange shift in the peak intensities is observed for the Hood map. This can be seen for example for the Reiner Gamma and Hartwig anomaly areas in Figure A.1 a and b, where the orange line representing the Hood map, display a peak shifted respectively by approximately 1° and 0.5° longitudinal.

Once the Hood map is excluded as candidate to be the primary map for inversions, the choice between the Tsunakawa and Ravat maps needs to be taken. The 2 maps show a number of similarities, both in the common high-resolution grid and surface map primary output, but also when looking more in detail in the areas of interest. The latter similarities can be observed when looking at the profiles, such as in Figure3.7, especially visible in cases b, c and d, e (in the annex), where the major and minor peaks show a good correspondence in position and, often, intensity of total magnetic field. Moreover, Ravat et al. (2020) compares the outputs of the 2 methods and identifies some spurious magnetic signals from the Tsunakawa map suggesting better defined anomaly patterns being depicted by the Ravat map, but overall finds no clear and unambiguous improvement in the mapped anomaly features. This prompts to look for other, novel ways to try to distinguish the 2 maps. An attempt is here conducted by studying the outputs of the correlation between the position of swirls and of surface magnetized material. Results, discussions, and implications of this correlation will be done thoroughly in the next chapters: here the focus is placed on trying to use the outputs as a discriminator for what map may be better suited for the project. This idea stemmed from realizing that the magnetized material for Reiner Gamma represent a better fit for the Reiner Gamma swirl for the Tsunakawa map rather than the Ravat map, as can be seen in Figure3.8 (in pink the swirl, in color the magnetized surface dipoles). The focus on Figure 3.8 shall be placed on the correlation between the strongest (the lightest) surface dipoles and the underlying pink delineation of the albedo anomaly/swirl. The magnetized material corresponding to the central body of the anomaly but especially the north-eastern extension appear to be slightly shifted west for the Ravat map, while the fit is much tighter for the Tsunakawa case. Such trend remains also when shifting the center of the circle to the north, south, east and west, proving the results to be consistent. The goal is to extend the analysis to the other known swirls referring to the map from Denevi

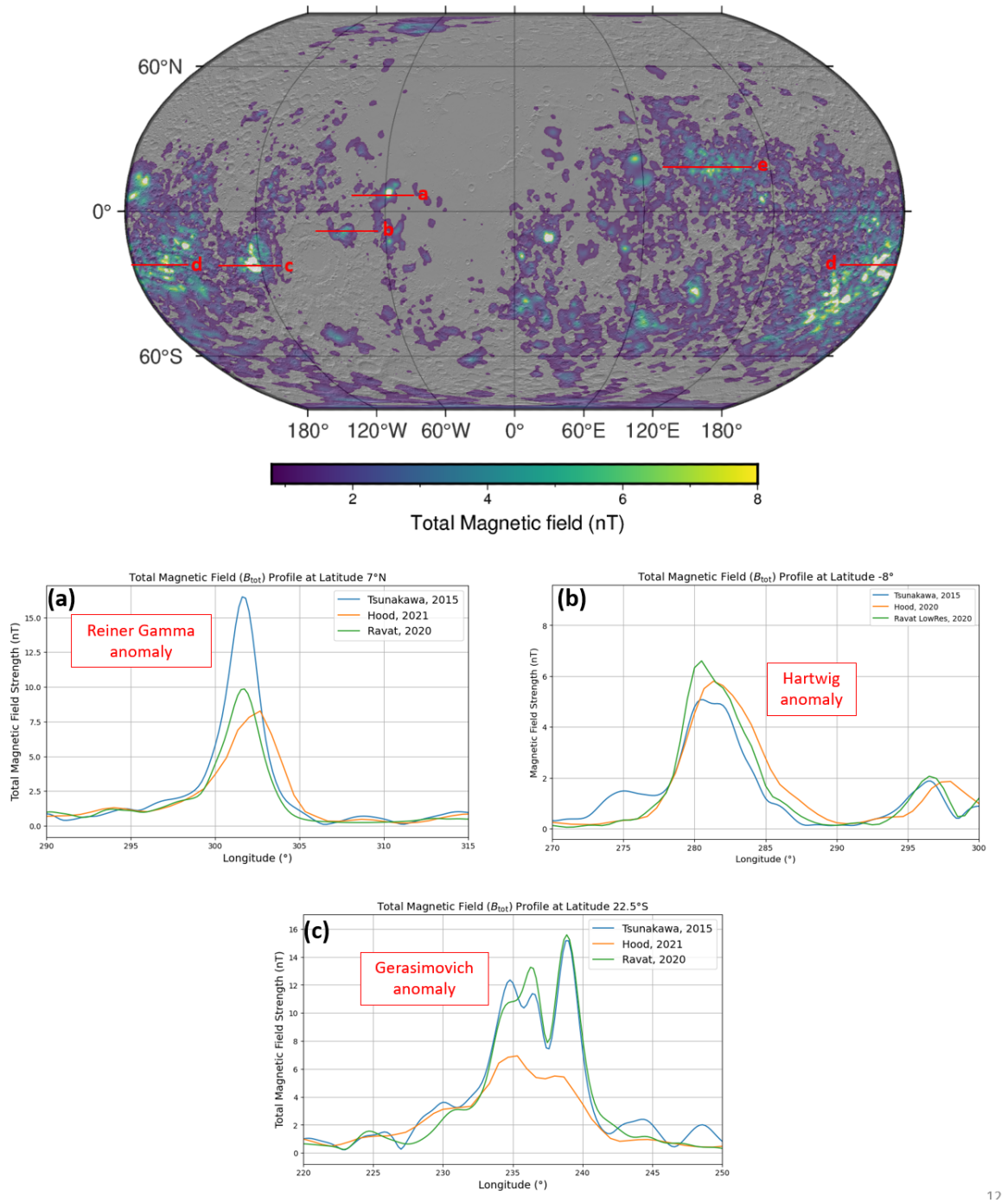

Figure 3.7: Profiles of the Tsunakawa, Hood and Ravat magnetic maps at selected latitude degrees and longitude ranges: 7°N and between 45°W and 70°W in correspondence to the Reiner Gamma anomaly in (a), 8°S and between 60°W and 90°W in correspondence to the Hartwig anomaly in (b), 22.5°S and between 140°W and 170°W in correspondence to the Gerasimovich anomaly in (c). Further cases (d, e) are found in the appendix. On top, the global magnetic map showing the longitudinal extension and latitudinal position of the profiles.

et al. (2016) and seeking to find more “anomalous shifts”. Results and comparison of the 2 maps on the correlation between the more highly magnetized material and the swirl position for the majority of the areas explored proved to be inconclusive, mostly because of a too low resolution. The majority of the isolated lunar swirls investigated are considerably smaller compared to the Reiner Gamma one and present a more amorphous and non-linear shape that, combined with the low resolution, can’t produce

a good material for comparison. Thus, this investigated method cannot be used.

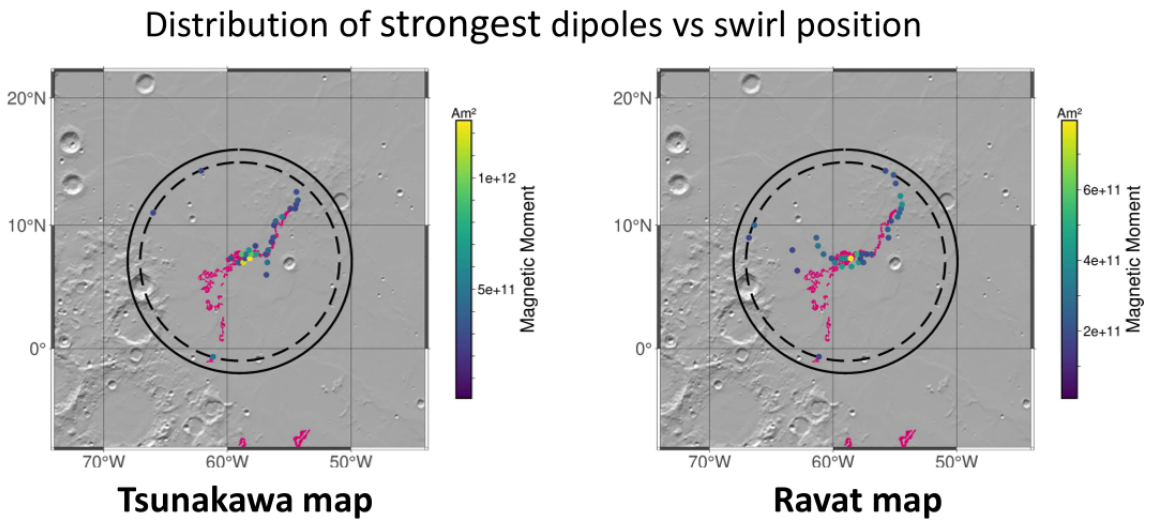

Figure 3.8: Surface disposition dipoles and relative magnetic moments as output from the inversion using the Tsunakawa map (on the left) and the Ravat map (on the right). Underlain is delineated the Reiner Gamma swirl. What is to note and compare is the correlation between the position of the strongest dipoles (lighter color) and the albedo anomaly (swirl).

Since a suitable and systematic method for determining which magnetic map to select is neither readily available nor easy to find, an arbitrary decision is made here to use the Tsunakawa map. This choice allows for comparisons with previous studies that have utilized this map since its availability in 2015. The more recent and less frequently utilized Ravat map is not discarded but reserved for potential use to compare results.

4

Methods

This chapter provides a comprehensive explanation of **Parker's Inversion method**, starting from its original formulation, mathematical considerations and application in Parker (1991), to its implementation in the Fortran code used for this study. While the magnetic datasets and the rationale behind the choice of the magnetic map are discussed in Chapter 3, this section focuses on the construction of the computational grid, the selection of key inversion parameters, and related methodological decisions.

4.1. Inversion methodology

Most methods used to date to constrain surface and subsurface sources of magnetic anomalies have relied on the available geological and geophysical context, using swirls, gravity data, and topographical features as proxy (e.g., Hemingway and Tikoo, 2018, Garrick Bethell and Kelley, 2019, Kelley and Garrick-Bethell, 2020, Oliveira et al., 2017a). In contrast to these studies, this project employs the method described by Parker (1991), referred to here as the Parker's Inversion method, which does not depend on the presence of identifiable signatures in the area of interest. This method was originally developed to determine the best-fitting direction of the Earth's crustal magnetization from seamounts, allowing also the north paleopole position to be inferred under the assumption of a dipolar magnetic field. More recently, the potential and effectiveness of the method to provide for the best-fit surface distribution of dipoles have been assessed and validated (Oliveira et al., 2024). To gain deeper insight into the mathematical foundation and the key considerations behind the development of the inversion method, the following paragraph builds on the theoretical framework presented by Parker (1991).

Inversion methods for the Earth's seamounts in the 70s and 80s struggled to properly deal with the intrinsic non-uniqueness that any inverse problem face when trying to obtain the distribution of the magnetic sources. The widely used uniformly magnetized volume model didn't suit well with the magnetically heterogeneous seamounts, but the direction of magnetization was found to not vary widely if field reversals weren't to be taken into account. Parker (1991) undertakes this route of using a model with uniform direction of magnetization without constraining the intensity, and manages to show how the unidirectional class of solutions has a powerful ability to match magnetic anomaly patterns.

The model magnetization M, which expresses the density of magnetic dipole moments within the magnetic material, is defined for a seamount (or, more generally, any small isolated crustal magnetic anomaly) of volume V as:

$$M(s) = \hat{m} \cdot m(s_i), \qquad m(s_i) > 0 \tag{4.1}$$

where the dipole moment m (related to the magnetization M through the source volume, as in equation 2.3) is a function of the position vector s_i within V, and $\hat{m}$ is the unit direction of magnetization. In Parker (1991), the component of the magnetic field aligned with the geomagnetic field was arbitrarily chosen for the mathematical demonstration and successive application with real data. Similarly, this study models a single magnetic field component, specifically the radial component r, consistent with previous lunar investigations by Oliveira et al. (2017a) and Oliveira and Wieczorek (2017). Sensitivity tests involving the θ (polar) and ϕ (azimuthal) components of the magnetic field have been previously conducted in Oliveira and Wieczorek, 2017, showing that the component choice affects marginally the inversion results. The following mathematical derivations will thus proceed using the radial component. Consequently, the direction vector is defined as $\hat{d}_j = \hat{r}_j$ ($\hat{r}$ the radial direction), where j refers to a specific observation point out of the total of observation points N_o.

The combined effect of the set of magnetic dipoles at positions s_i within the volume V, sums up to the radial magnetic field d, seen at the observation point j:

$$d_j = \sum_{i=1}^{N_d} g_j(s_i) m(s_i), \qquad j = 1, \ldots, N_0 \tag{4.2}$$

where N_o is the number of observations, N_d is the number of dipoles in the crustal volume and g_j corresponds to the contributing effect of a single dipole to d_j, and is defined as:

$$g_j(s_i) = \frac{\mu_0}{4\pi} \left(\frac{3\hat{m} \cdot (r_j - s_i)\hat{d}_j \cdot (r_j - s_i)}{|r_j - s_i|^5} - \frac{\hat{m} \cdot \hat{d}_j}{|r_j - s_i|^3} \right) \tag{4.3}$$

To clarify, Equation 4.2 states that the magnetic anomaly observed at r_j results from the combined effect of multiple unidirectional dipoles distributed within V. Equation 4.3 expresses the contribution of a single unit dipole at s to the anomaly at r_j. Note that the condition of $m(s_i) > 0$ in equation 4.1 is needed, otherwise a magnetization model formulated as equation 4.1 and respecting the constraints of equation 4.2 is always found.

Equations 4.2 and 4.3 can be combined in matrix form as:

$$\vec{d} = G(\hat{m}) \cdot \vec{m} \tag{4.4}$$

Where $\vec{d}$ is the vector of the radial magnetic field observations, $\vec{m}$ is the vector containing the magnitude of the dipole moments (with each element greater or equal to zero), and the matrix G, function of the magnetization direction $\hat{m}$, contains the elements given by Equation 4.3. This simplified equation in matrix form is what is effectively used within the Parker inversion algorithm, and it is solved for $\vec{m}$ having the observational data $\vec{d}$ and having computed G. More on the algorithm in the following section. Let's now suppose to temporarily impose an upper limit on the strength of magnetization (so far unconstrained): $0 \leq m \leq M_0$. Let's also wish to satisfy exactly the demands of equation 4.2, requiring the smallest possible M to do the job (calling it M_0). The theory of ideal bodies (Parker, 1975) can now be directly applied to this problem, for which the magnetic intensity within the volume V is either 0 or M_0 and the regions of positive magnetization are enclosed in smooth boundaries that always intersect the surface of the volume. Thus, the boundaries of the magnetized zones are equipotential surfaces of multipole sources located at the observation sites (Parker, 1991). When removing the upper limit on m, the ideal-body solution is found to degenerate into a set of point sources in the boundary of V, as shown in Parker (1975).

With the equations and mathematical considerations so far presented, the goal is to compare the modeled magnetization obtained through equation 4.4 with the observations $\vec{d}$ checking the goodness of fit to find the best estimate of the uniform magnetization direction after the corresponding best distribution of dipoles. The current problem is inherently three-dimensional, as it involves a volume of dipoles distributed in space. However, this can be simplified to a two-dimensional problem by projecting the dipoles onto a plane. Before demonstrating how Parker achieved this reduction, it is necessary to first define a misfit function that quantifies the discrepancy between the observed and predicted magnetic

field. The chosen form of the misfit function, is the widely used sum of squared discrepancies (SSD):

$$F(m) = \sum_{j=1}^{N_d} [d_j - \sum_{i=1}^{N_d} g_j(s_i) m(s_i)] \tag{4.5}$$

The reduction of the volumetric distribution to a surface distribution of dipoles finally emerges after some mathematical manipulations, revealing that the modeled M that minimizes Equation 4.5 with $m > 0$ is a set of at most N_d dipoles distributed on the surface of the seamount / magnetic anomaly. Although the entire volume V is available for modeling, the optimal solution confines the magnetization to the boundary, specifically the surface. This approach leads to significant savings in complexity and thus computational time. In the current project, the problem is reduced from a three-dimensional (3D) to a two-dimensional (2D) distribution of magnetization, unlike in Parker, 1991, where this simplification was not fully achieved.

4.2. Implementation in Fortran: description of the model

In practice, the continuous surface magnetization distribution is replaced in the model by a collection of point-like dipoles known as equivalent source dipoles (ESDs), where each dipole, maintaining the same magnetization direction as the others, acts as a small magnetic source located at a specific point. The complexity is thus reduced by converting the continuous problem into a discrete one.

The Parker inversion method is implemented in a Fortran code, primarily developed by Oliveira et al. (2024) and based on earlier studies (e.g., Oliveira et al., 2017a, Oliveira and Wieczorek, 2017, Oliveira et al., 2019) that employed Parker's method. More recently, Mark A. Wieczorek independently developed a Python version of the code, which will be used as a benchmark tool for verification and validation in this study.

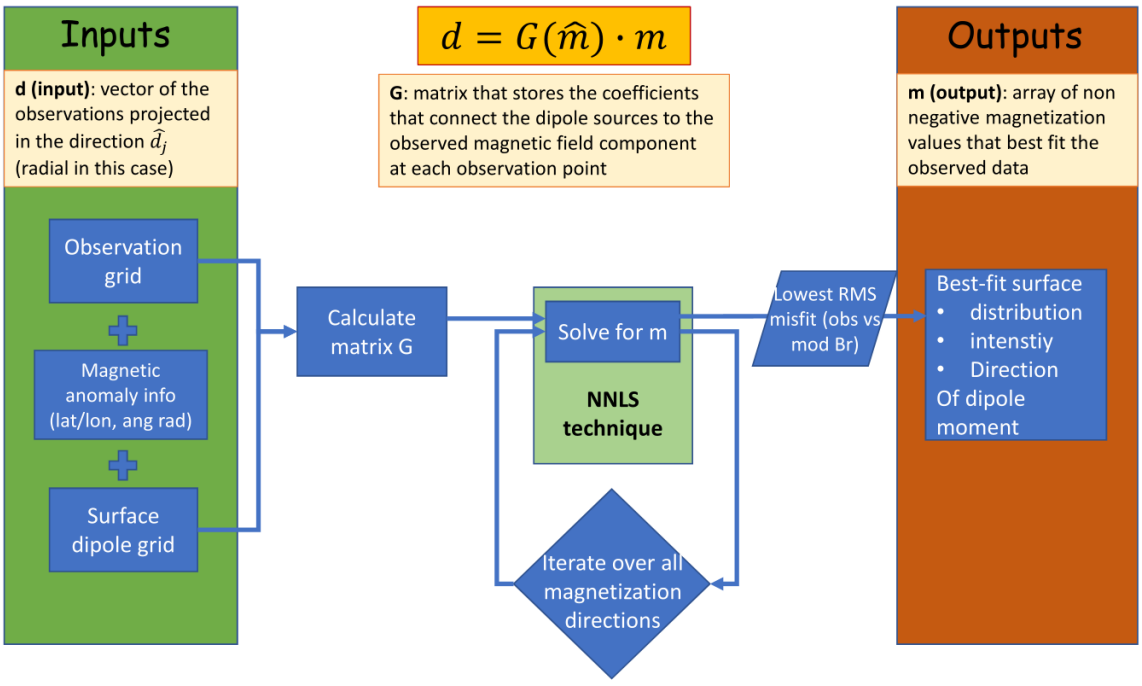

Figure 4.1: Scheme flow chart of the Parker's method.

A schematic version of how the Parker's inversion method is implemented in the Fortran code is shown in Figure 4.1. Let's first explain the steps needed in the routine, and subsequently the choices

of some parameters and some considerations.

The first step is to select an appropriate area of interest, usually targeting a magnetic anomaly (or group of smaller anomalies). The point-like dipoles are then placed on the surface forming a grid, following the homogeneous polar coordinate distribution of points on the sphere from Katanforoush and Shahshahani (2003). The grids are then confined within circles of an arbitrarily chosen angular radius that fully encompasses the magnetic anomaly (or anomalies). To minimize edge effects, the observation area is made slightly larger than the dipole area. Aiming to solve for the magnetic moment array m in equation 4.4, the first mathematical step is to calculate the G matrix, which stores the coefficients that connect the dipole sources to the observed magnetic field component at each observation point. Given d, the observed radial component of the magnetic field, and having calculated G, the system is solved for m using the NNLS (non-negative least squares) routine described in Lawson and Hanson (1974). The NNLS algorithm is applied in a loop that varies the magnetization direction over all directions over a 2-degree equidistant grid (in latitude and longitude, better called here inclination and declination). The best-fit results are those with the lowest RMS misfit. A small explanatory note for the misfit function: the NNLS routine outputs the L^2-norm, which is the square root of the sum of squared discrepancies used in Parker (1991), a choice that doesn't alter the mathematical considerations of the method. The L^2-norm is then normalized to the RMS in the main Parker Inversion code, by dividing it by the number of observations N_o. The relative data is then saved into files that are later used for plotting purposes.

The main output of the inversion is the identification of the locations of dipoles with nonzero magnetic moments, the estimation of their intensities, the computation of the predicted magnetic field, and the evaluation of the root-mean-square (RMS) misfit between the observed and modeled data. The code can also compute the north paleopole position for each pair of inclination and declination angles, using modified equations from Butler (1992). While not the primary focus of the inversion in this investigation, the north paleopole position provides valuable insights about the direction of the ambient dipolar magnetic field in the past, which will be further discussed in chapter 7.

4.3. Considerations on the algorithm and choice of parameters

The selection of parameters for the algorithm is now outlined, acknowledging that exploring all possible configurations lies beyond the scope of this study and would be both time-intensive and dispersive. These choices are made with the goal of standardizing the inversion setup as much as possible to maintain consistency.

Let's begin with a consideration about the choice of the magnetic anomaly/anomalies or area of interest. The target needs to be appropriately selected, as the optimal conditions for the inversion are of relatively good isolation and small size. Small-sized anomalies offer a balanced compromise between computationally manageable inversion run times and adherence to the unidirectionality assumption. As the size of the area increases, the likelihood of a naturally occurring, shared magnetization direction within the crust decreases. To be clear, the assumption of unidirectional magnetization is not likely to happen in nature but can be a reasonable simplification for a small-enough area, and is required for the Parker's method to be applied. The complex and vast far side anomalies, as grouped in the Marginis-King area and at the northern edge of the South Pole-Aitken basin (see Figure 1.4), don't represent a feasible target. Still, this work attempts to isolate a few areas, pushing the inversion method to its limits.

Regarding the dipole grid generation, the point-like dipoles are placed on the surface of a sphere with a radius equal to the Moon's average radius ($R_{Moon} = 1737.1$ km) for simplicity, rather than following the surface topography. The polar coordinate distribution of points on the sphere from Katanforoush and Shahshahani (2003) is preferred over two alternative algorithms ($\sqrt{3}$-subdivision and lattice point methods) due to its more effective minimization of the Coulomb potential, a metric used as a proxy for defining an "even distribution".

The resolution selection for the dipole grid, typically set at 0.33° and 0.2° (corresponding to 540 and 900 latitude partitions, respectively), partially depends on the dimensions of the analyzed area.

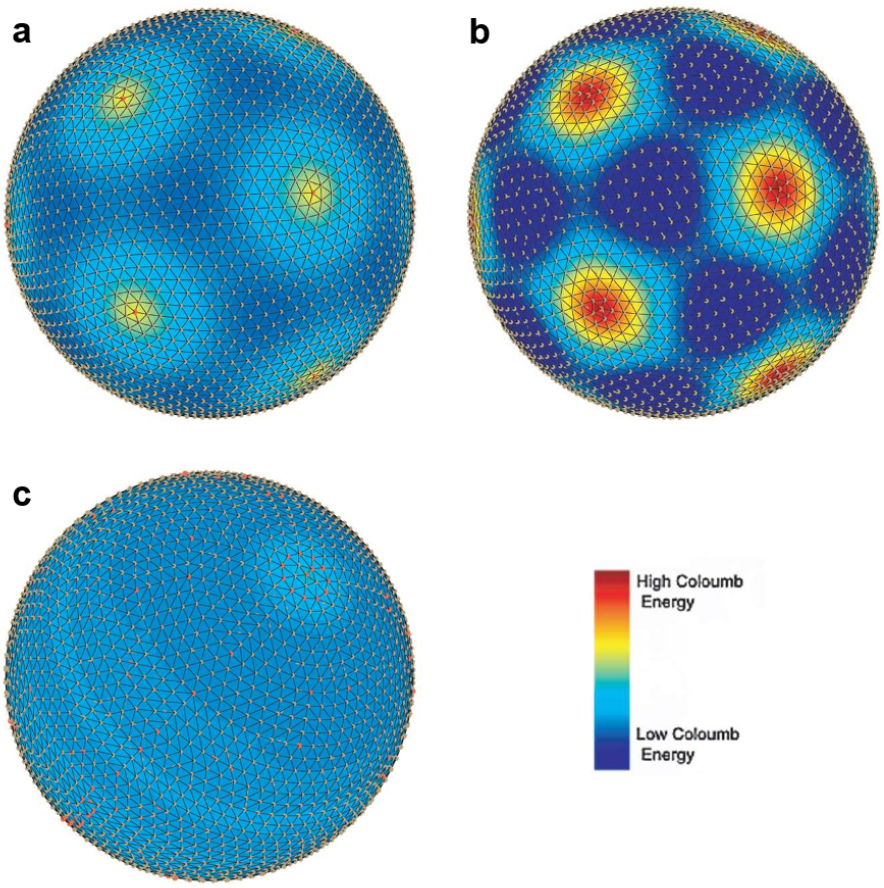

Figure 4.2: Methods of distribution of points on the sphere and Coulomb energy associated to a non-optimized state: a) $\sqrt{3}$-subdivision, b) lattice point methods, c) polar coordinate distribution method. It is evident how, despite the non-optimization, the polar coordinate distribution method is the best choice for an even distribution. Credits for the image: Katanforoush and Shahshahani (2003).

Sensitivity analyses (see chapter 5) show minimal differences in surface dipole distributions and magnetic moment intensities between the two resolutions, though inversions using 900 latitude partitions are more time-intensive. Notably, the chosen dipole-grid resolution is finer than the observation-grid resolution. This approach ensures compliance with one of Parker's method properties: given N_o (the number of magnetic field observations), at most N_o of the N_d surface dipoles will be non-zero. By controlling the dipole-grid resolution, N_d can be chosen to be much larger than N_o, with the NNLS routine automatically determining the non-zero surface dipoles. Furthermore, while some inversions in this study that theoretically should have "broken" the algorithm (observation grid denser than the dipole grid) still yielded plausible results, Oliveira and Wieczorek (2017) identified inconsistencies when analyzing inversions that deviated significantly from the theoretical framework, highlighting the need for careful interpretation of outputs from such anomalous inversions. An example of a different resolution grid applied to the Reiner Gamma magnetic anomaly is found in Appendix-A in Figure A.3.

Moving on to the observation area and dipole area, the angular radius for the dipole grid is rarely chosen to exceed 10 latitudinal degrees (approximately 300 km). Larger sizes, as previously discussed, take longer to compute, violate the unidirectionality assumption more significantly, and include additional magnetic data that may not actually be related to the magnetic anomaly of interest. Therefore, outside the circled area of interest, this project assumes the rest of the lunar crust to be non-magnetized. Typical angular radii used are 8°/9° (for the surface dipole grid and observation grid, respectively) and 10°/11°, although both smaller and slightly larger radii have also been explored (see chapter 5 and 6).

In regard to the north-paleopole estimation, calculation of the uncertainty is done as follows: the 1σ error ellipse for the magnetization direction is defined by those directions having RMS misfit which is equal or lower than the RMS background field, with the background field considered in this case to be the field present between the two circles. This is another reason why the choice of isolated sources is important: the residual unmodeled magnetic field is assumed to be statistically similar to the "background field" that surrounds the anomaly. Thus, from this definition of error, it is valuable to have the strength of the residual field smaller compared to the strength of the magnetic field coming from the anomaly. This approach does present some challenges, such as cases where relatively strong fields are located between circles or when analyzing weak anomalies. On the positive side, the method has already been evaluated in Oliveira and Wieczorek (2017) and Oliveira et al. (2024), demonstrating a degree of stability.

5

Verification and Validation

The verification and validation steps are critical to ensure the reliability, robustness, and accuracy of the Parker inversion method as implemented in this study. Verification focuses on determining whether the algorithm is implemented correctly and operates as intended, while validation assesses whether the results produced by the algorithm are meaningful and aligned with real-world data. Previous studies, such as Oliveira and Wieczorek (2017) and Oliveira et al. (2024), have already carried out some level of verification and validation using this method. However, their focus differed from what is explored here. Since those studies, new tools have become available, including new codes, recently developed magnetic maps, and additional parameters of interest to be tested. These advancements provide an opportunity to revisit and expand the verification and validation process, tailoring it specifically to the goals of this study and ensuring the method remains reliable under these new conditions.

Used verification methods are:

- **Comparison of FORTRAN and Python codes**, with the latter developed by Mark A. Wieczorek and recently completed. In this project, the Python code is used as a benchmark and produces nearly identical results to the FORTRAN code, with minor differences attributable to subtle variations between the two implementations. This comparison confirms a consistent and accurate implementation of the Parker inversion method.
- **Sensitivity Analysis**: the effect of a number of parameters (e.g., angular radius of circle, resolution of dipole grid, shift of circle center, etc.) in the inversion for a single magnetic map (from Tsunakawa et al., 2015) is explored to establish internal consistency in the implementation. Results of a sensitivity analysis on different parameters relatable to this project from Oliveira and Wieczorek (2017) are also shown.

The used validation method is:

- **Comparison Across Different Magnetic Maps**: results from 3 independently developed magnetic maps, namely the here called Tsunakawa map (Tsunakawa et al., 2015), Ravat map (Ravat et al., 2020) and Hood map (Hood, Torres, et al., 2021), are compared. The comparability of the inversion outputs ensures that the method produces meaningful and reliable results for different datasets, thus validating the algorithm by confirming that the outcomes align with real-world variations in the input data.

5.1. VERIFICATION: Comparison of FORTRAN and Python codes

The main differences between the Python code and the FORTRAN code can be summarized as follows:

- First, the coordinate points of the equal-area grids vary slightly: in the FORTRAN code, point-like dipoles are positioned on the sphere's surface using the homogeneous polar coordinate distribution method outlined in Katanforoush and Shahshahani (2003), while the Python code employs a custom approach. These differences could lead to minor variations in the results; however, using a sufficiently high resolution for the grids should reduce these discrepancies.
- Second, the Python script places the dipoles on the physical surface using a planetary shape model, whereas in FORTRAN these are placed on a sphere of constant radius. This may also give rise to small differences.

A number of magnetic anomalies have been analyzed and compared, to verify whether the two codes produce the same results, targeting also problematic areas such as the poles. The example here presented depicts the case of the Reiner Gamma magnetic anomaly, the anomaly of reference in this project and for this verification and validation process.

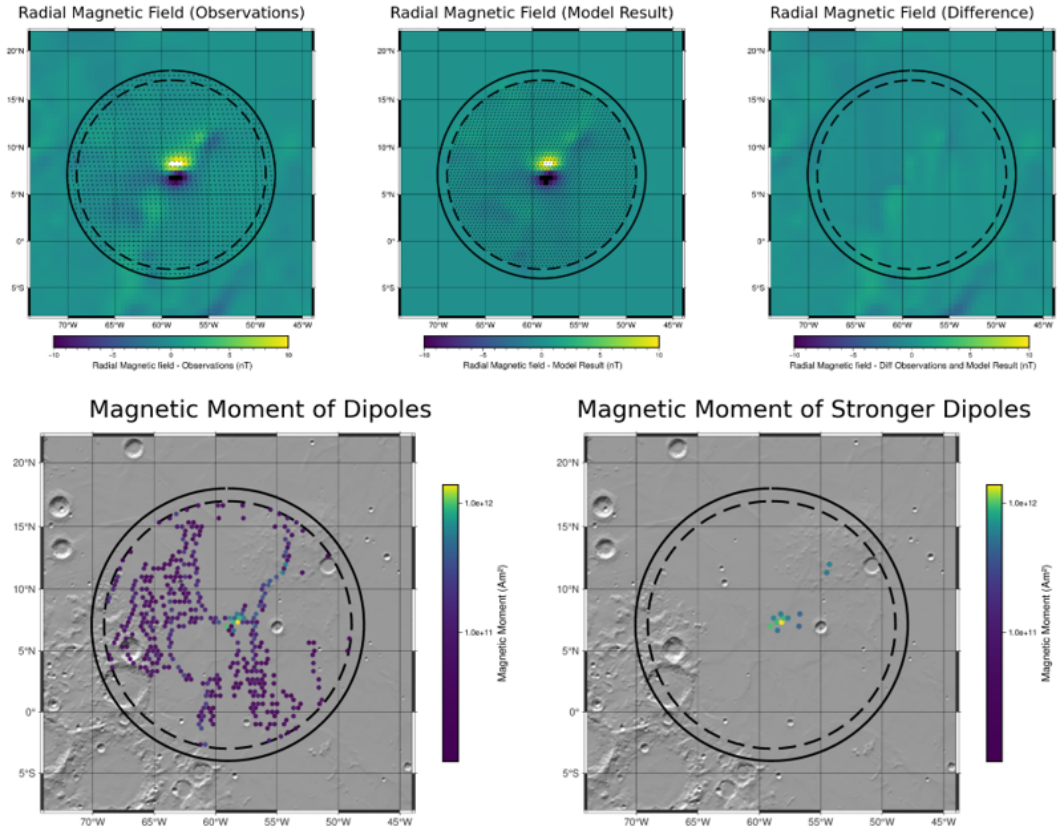

Figure 5.1: Output for the FORTRAN code

In both cases, identical inversion parameters are applied: both codes use a dipole grid with 540 latitude partitions (0.33° resolution) and a 0.5° resolution observation grid. The dipole and observation area angular radii are set to 10° and 11°, respectively, with the center point at latitude 7° and longitude 301°, always using the Tsunakawa map. Comparing visually the 2 mosaics of results (Figure 5.1 for the output with the FORTRAN code and Figure 5.2 for the Python output), what is immediately apparent is the almost complete match between the surface disposition of dipoles. What differs, probably due to the minor differences between the 2 algorithms mentioned above, are the magnitude of the magnetic moments of the stronger point dipoles, with the Python code resulting in higher overall maximum intensities ($1.38e^{12}\ Am^2$ as compared to $1.22e^{12}\ Am^2$). The striking similarities between the outputs ensure a correct and consistent implementation of the Parker inversion method in both codes.

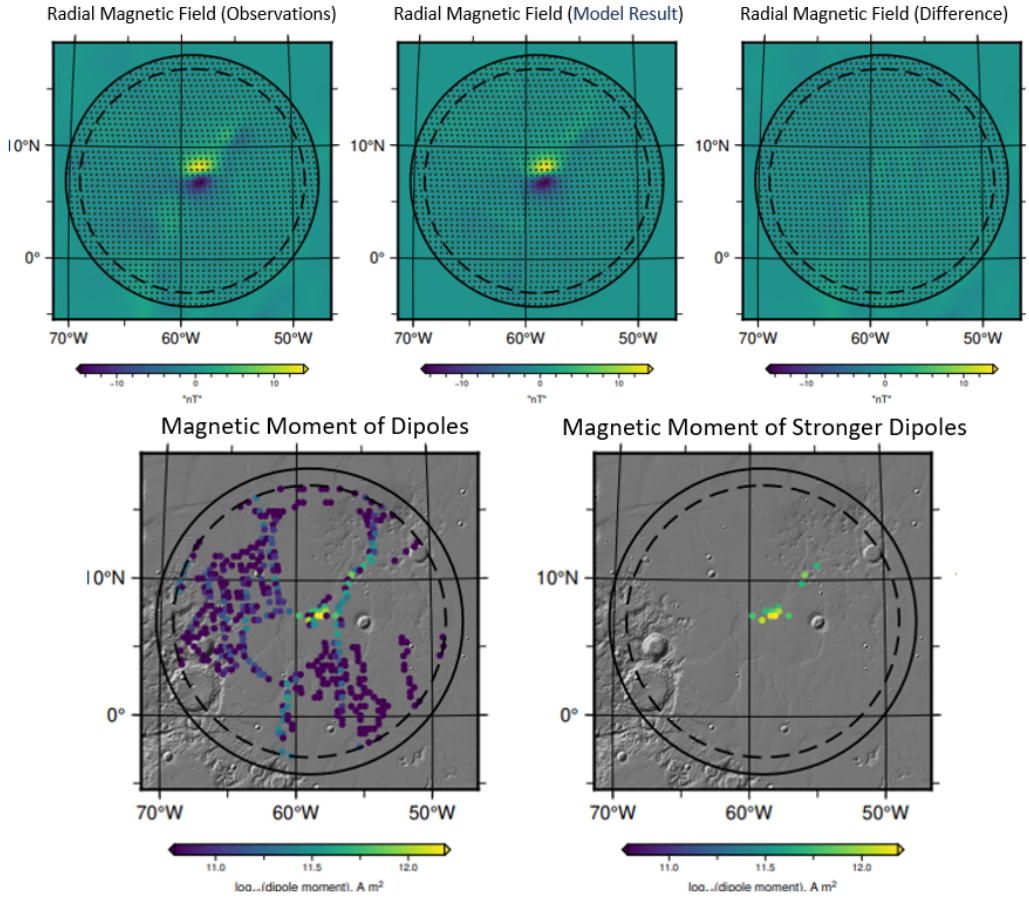

Figure 5.2: Output for the Python code

5.2. VERIFICATION: Sensitivity Analysis

As another crucial verification tool, the sensitivity analysis alters the parameters for the inversion of a single magnetic anomaly, once again selecting Reiner Gamma, and examines the resulting differences, testing the robustness and reliability of the algorithm. The reference magnetic map used is the Tsunakawa map, centered at latitude 7° and longitude 301°. Following is a list of the parameters varied in this sensitivity analysis:

- Equal area observation grid vs. non-equal area observation grid. To briefly explain what this means, the former is mathematically easier to handle during inversions because it produces a rectangular matrix, but is problematic in polar areas. The latter offers more uniform sampling of magnetic data and better handling of polar regions, but is more complex to manage in terms of matrix construction. For the majority of the inversions carried out in this project, the equal area observation grid is used;
- Resolution of the observation grid;
- Angular radii of surface dipole grid and observation grid;
- Central point of the area of interest: shifts of 2° north, east, south, west;
- Resolution of the surface dipole grid;
- Resolution of the inclination/declination angles grid.

Moreover, the analysis also considers additional parameters, as studied by Oliveira and Wieczorek (2017), including:

- The relative dimensions of the angular radii of observation area and dipole area, focusing on the edge effects;

- The use of the θ and ϕ components of the magnetic field;
- The implementation of the surface magnetic field model

In this comprehensive parameter study, the comparison elements include the minimum inversion misfit, the maximum, and cutoff magnetic moment (m_{max} and m_{cutoff}), the largest and average differences between the observed and modeled magnetic fields, the ratio of non-zero dipoles to total dipoles used, as well as the paleopole position and its uncertainty. This data is summarized in table 5.3. Let's now analyze the results, category by category, referring to the plots and figures found in the appendix:

- **Equal area vs. non-equal area observation grid**: ensuring consistency between the outputs of these two cases is crucial to justify the extensive use of the equal-area observation grid, fundamental to analyze the poles. The equal area grid is not the original grid used in the Tsunakawa map and is also not employed in Oliveira et al. (2024). Overall, the 2 grids are very comparable, proven by an average difference between modeled and observed magnetic field respectively of $0.428nT$ and $0.438nT$ and a minor deviation of the north paleopole position of 5.03° from the inversion results (see Figure A.5 in the appendix). Changes in **observation grid resolution** can influence the strongest magnetic moment modeled: a denser distribution of point-like dipoles allows the corresponding magnetic field intensity to be shared among more elements, thereby reducing the maximum modeled magnetic moment m_{max}. This is confirmed by the inversion results: $m_{max} = 4.56 \cdot 10^{11} Am^2$ for 540 latitude partitions (0.33° resolution) and $m_{max} = 4.01 \cdot 10^{11} Am^2$ for 360 latitude partitions (0.5° resolution), resulting in a slightly different cutoff value (always 30% of m_{max}) for the strongest dipoles considered. All other values of interest remain practically unchanged.
- Variations in the **angular radii of observation and dipole grids** are more pronounced compared to the previous category. This is primarily due to the use of smaller circles (e.g., a 4°/5° dipole grid/observation grid combination), which results in higher misfits and larger discrepancies between observed and modeled radial magnetic fields. From a 7°/8° angular radius combination onward, the values stabilize and plateaus as the Reiner Gamma anomaly is fully encompassed within the circle (see Figure A.6 in the appendix). Despite these variations, the maximum angular distance for the best-fit north paleopole position is only 7.86°, a relatively small and acceptable difference. Overall, the analysis suggests that results are more reliable when using larger angular radii.
- Shifting the **center-point location** is done to understand whether the distribution and intensity of the point-like dipoles holds when shifting the center of the area of interest, exposing the inversion to a slightly different region. It's important to avoid cutting through the anomaly, as doing it would have a large impact in the inversion. For this reason, shifts of only 2° are applied. As expected, shifts that bring the anomaly closer to the circle's edge (South and West case) experience slightly higher misfits and differences between model and observations (see figure A.7 in the appendix). The best-fit paleopole positions are only minimally impacted (3.22° is the maximum angular distance among all the cases).
- The **resolution of the dipole grid** has a major impact in the inversion output as it controls how well the model can match the observations: lower resolutions lead to very high misfits and differences, other than increasing by a wide margin the maximum modeled magnetic moment (see figure A.8 in the appendix). Moreover, resolutions lower (or equal) compared to the observation grid resolution (such as for 360 and 180 latitude partitions) technically do not respect the requirements from the theory of the Parker's method. Nonetheless, the overall surface distribution remains comparable, and the inversion doesn't "break" as one might expect. The results of sensitivity test with the spacing of surface dipoles agree with what is found from Oliveira and Wieczorek (2017).
- Changes in the **resolution of the inclination/declination angle pair** produce minimal and unimportant variations

Oliveira and Wieczorek (2017) tests on how various assumptions of the model approach may affect the results, focusing on differences in north paleopole position and relative uncertainty ellipse, and produce the following:

- The **relative difference in amplitude of the 2 circles' angular radius** illustrates how undesirable edge effects, observed in cases where the observation grid circle is the same size as the

General case	Parameter varied	Minimum misfit (nT)	Mmax (Am^2)	Mcutoff = 30% Mmax (Am^2)	Largest difference obs-mod (nT)	Average absolute difference obs-mod [nT]	Non-zero dipoles / Total dipoles [%]	Best fit N paleopole position (lon) [°]	Best fit N paleopole position (lat) [°]	Paleopole uncertainty (nT)
Reference case	Tsunakawa equal-area map, 0.5° obs grid resolution, 0.33° dip grid resolution, lat:7° lon:301°, dip grid = 8° / obs grid = 9°	0.533	1.34E+12	4.02E+11	2.086	0.428	18.58	310.4	-82.9	0.513
Equal area vs non-equal area obs grid	Non-equal area	0.542	1.26E+12	3.78E+11	-1.854	0.438	19.16	350.3	-82.4	0.529
Equal area vs non-equal area obs grid	Equal area	0.533	1.34E+12	4.02E+11	2.086	0.428	18.58	310.4	-82.9	0.513
Obs grid resolution	540 latitude partitions (res of 0.33°)	0.533	1.52E+12	4.56E+11	2.075	0.429	20.69	310.4	-82.9	0.507
Obs grid resolution	360 latitude partitions (res of 0.5°)	0.533	1.34E+12	4.01E+11	2.086	0.428	18.58	310.4	-82.9	0.513
Angular Radii	Dipole grid = 4° / Observation grid = 5°	0.877	1.43E+12	4.29E+11	-3.17	0.663	14.65	279.9	-80.4	1.034
Angular Radii	Dipole grid = 5° / Observation grid = 6°	0.814	2.01E+12	6.03E+11	3.93	0.594	16.45	288	-79.7	1.026
Angular Radii	Dipole grid = 6° / Observation grid = 7°	0.714	1.87E+12	5.61E+11	2.766	0.561	16.65	317.1	-81.7	0.763
Angular Radii	Dipole grid = 7° / Observation grid = 8°	0.611	1.33E+12	3.99E+11	2.068	0.493	17.63	322.1	-83.6	0.579
Angular Radii	Dipole grid = 8° / Observation grid = 9°	0.533	1.34E+12	4.02E+11	2.086	0.428	18.58	310.4	-82.9	0.513
Angular Radii	Dipole grid = 9° / Observation grid = 10°	0.494	1.48E+12	4.44E+11	-1.692	0.389	19.36	314	-84.9	0.501
Angular Radii	Dipole grid = 10° / Observation grid = 11°	0.481	1.38E+12	4.14E+11	-1.772	0.372	18.69	301	-86	0.548
Angular Radii	Dipole grid = 11° / Observation grid = 12°	0.468	1.55E+12	4.65E+11	-1.808	0.358	18.95	322.3	-86.8	0.546
Angular Radii	Dipole grid = 12° / Observation grid = 13°	0.444	1.57E+12	4.71E+11	-2.071	0.332	19.26	322.3	-86.8	0.495
Centerpoint shift	2° East	0.537	1.36E+12	4.08E+11	-1.861	0.412	14.95	303.5	-84	0.527
Centerpoint shift	2° North	0.527	1.39E+12	4.17E+11	-2.184	0.402	19.53	309.8	-82.4	0.51
Centerpoint shift	2° South	0.624	1.96E+12	5.88E+11	3.165	0.481	16.03	301	-84.5	0.757
Centerpoint shift	2° West	0.574	1.83E+12	5.49E+11	2.79	0.444	20.27	314.6	-81.7	0.659
Dip grid resolution	180 latitude partitions (res of 1°)	0.75	3.65E+12	1.095E+12	6.404	0.518	60.59	310.4	-82.9	0.479
Dip grid resolution	360 latitude partitions (res of 0.5°)	0.54	2.06E+12	6.18E+11	1.879	0.434	32.61	310.4	-82.9	0.507
Dip grid resolution	540 latitude partitions (res of 0.33°)	0.533	1.34E+12	4.02E+11	2.086	0.428	18.58	310.4	-82.9	0.513
Dip grid resolution	900 latitude partitions (res of 0.2°)	0.53	1.63E+12	4.89E+11	2.04	0.427	6.99	310.4	-82.9	0.52
Inc/Dec angles grid resolution	**90 latitude partitions (res of 2°)**	0.533	1.34E+12	4.02E+11	2.086	0.428	18.58	310.4	-82.9	0.513
Inc/Dec angles grid resolution	180 latitude partitions (res of 1°)	0.533	1.39E+12	4.17E+11	1.906	0.428	19.03	311.9	-83.9	0.514

Figure 5.3: Data from the sensitivity analysis grouped into category of parameters varied

dipole grid circle and 0.5°/1°/1.5° larger, do not occur in the 1° and 1.5° cases. In fact, the inversion results for the 1.5° case led to nearly identical paleopole positions and uncertainties. This suggests that the use of the observation grid = dipole grid + 1° case is preferable, as it minimizes the risk of capturing magnetic anomalies between the two perimeters compared to the 1.5° case.

- The analysis of inversions using the θ **and** ϕ **magnetic field components** instead of the radial one produce all similar results (test performed on 15 magnetic anomalies listed in table 1 in Oliveira and Wieczorek (2017)). Comparable paleopole positions differ of a maximum of 4° and uncertainty ellipses are largely consistent with those produced from the inversions using the radial component of the magnetic field.
- The use of the **surface magnetic field map** as observations, instead of the 30 km altitude map (which has a lower spatial resolution), produces nearly identical results, with maximum paleopole differences of 10°. Given that the 30 km altitude magnetic map is derived from the surface map, these results are not surprising.

5.3. VALIDATION: Comparison Across Different Magnetic Maps

This section has already been addressed in the Datasets chapter (chapter 3). As a short summary, the investigated maps produce comparable results, despite showing some differences (see figure A.4 in the appendix):

- The output distribution of point-like dipoles is more similar between the Tsunakawa and Ravat maps, as the methods used to create the maps are similar. In contrast, for the Reiner Gamma example, the Hood map produces a distribution of stronger dipoles slightly shifted to the north/north-east and a distribution of weaker dipoles that does not exhibit the features seen in the other two maps (figure 5.4).
- The three maps produce surface dipoles with slightly different (but comparable) maximum magnetic moments m_{max}. This is expected, as the same magnetic features have different intensities across the maps: the Hood map has globally lower magnetic field values due to a more restrictive selection of data from satellite passes and more conservative error/uncertainty estimates. Indeed, looking at the Reiner Gamma example in Figure 5.4 and keeping in mind the profile of the total magnetic field in Figure 3.7, the Hood and Ravat maps present similar magnetic moments, while the Tsunakawa map produces higher values.
- The paleopole position and uncertainty ellipse vary the most of all the parameters investigated in the verification and validation analysis. The impact of the input magnetic field map cannot be understated, and larger discrepancies in the output are expected. The north paleopole positions remain comparable (looking at the examples of Reiner Gamma and Mendel-Rydberg magnetic anomalies), and produce a maximum of 32° of angular distance.

Overall, the outputs demonstrate a good degree of alignment and consistency across the different magnetic maps used as input for the inversions, validating the method's applicability to a variety of real-world datasets.

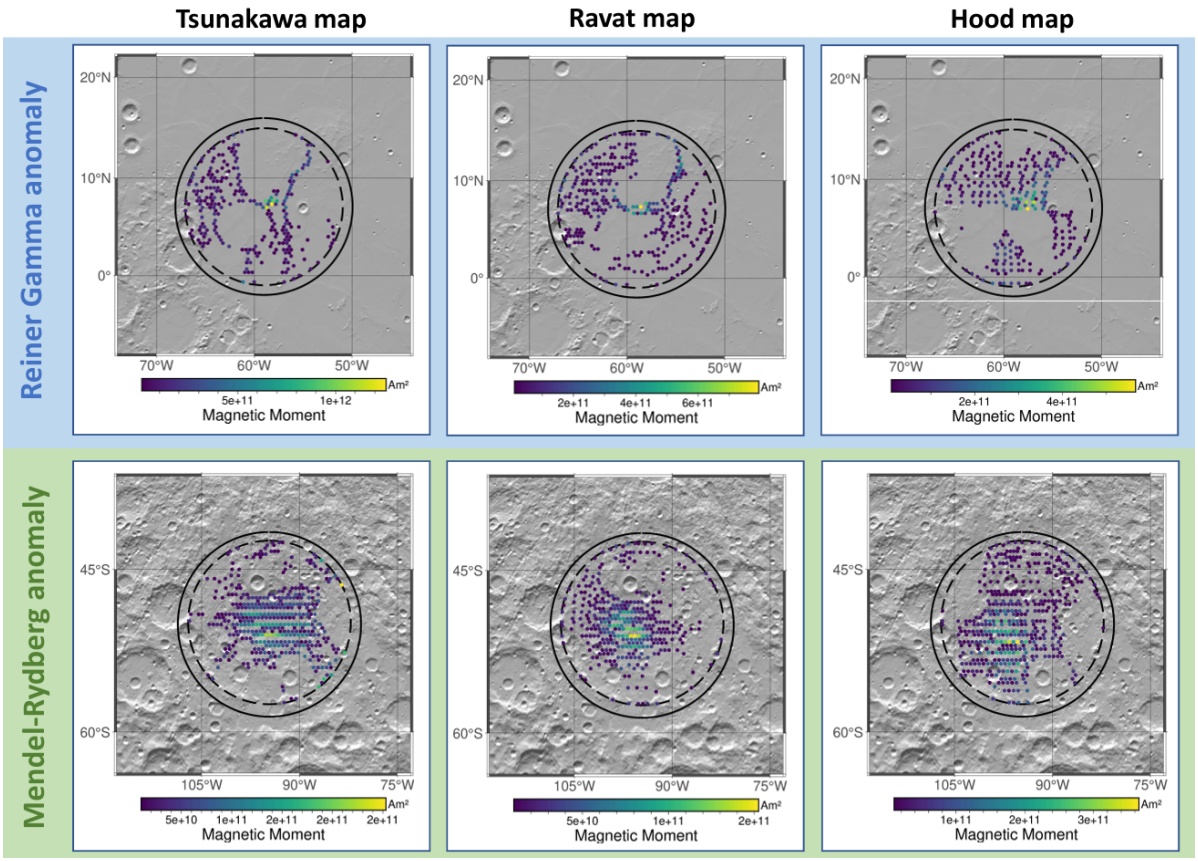

Figure 5.4: Modeled surface distribution and magnetic moment of point-like dipoles for the 3 maps considered in this study: Tsunakawa (Tsunakawa et al., 2015, Ravat (Ravat et al., 2020) and Hood (Hood, Torres, et al., 2021) maps. Examples of the Reiner Gamma (above) and Mendel-Rydberg (below) magnetic anomalies

6
Results

The current chapter presents the geophysical inversion results which are the main outcomes of this project. To help contextualize the findings, the chapter begins with an in-depth analysis of a representative sample output, focusing on the Reiner Gamma magnetic anomaly (Section 6.1). This case serves as a foundation for understanding the subsequent results. In Section 6.2 a selection of 6 cases that exemplify the diverse types of anomalies investigated are presented, out of the 26 regions examined. The remaining inversion results are available in Appendix A (Figures A.9 to A.15). The inversion results will also be compared, looking at a number of output parameters, in some comparative tables and figures.

6.1. Reiner Gamma

Figure 6.1 shows five maps that are representative for a generic extended output of the inversion process for a chosen magnetic anomaly, in this case the Reiner Gamma anomaly. This case uses a "non-equal area" Tsunakawa magnetic map at 30 km altitude, meaning that the distribution of points on the sphere at 30 km isn't spatially regular but can be easily mathematically described by a rectangular matrix, for ease of computation. Using a non-equal-area map, compared to the equal-area version that is more extensively implemented in this project, has a minimal impact on targets at the equatorial latitudes, such as Reiner Gamma (see table in Figure 5.3 in the Sensitivity Analysis). In fact, differences become significant only at more extreme latitudes, allowing for an interchangeable use of the 2 maps for low latitudes.

Starting with the upper row of maps, all three figures feature two circles: an inner circle and an outer circle. The outer circle, represented by a solid line and referred to here as the "observation area", bounds the observed magnetic data on the grid at an altitude of 30 km. In this example, the observation area has a radius of 11°, which is one degree larger than the circle that encloses the point-like dipoles from the surface grid. The small dots within the circles represent the grid points. The dipole grid resolution is set higher than that of the observation grid (0.33° vs. 0.5°) to ensure numerical stability. If the number of dipoles were equal to or fewer than the number of observations, the system could become under-determined, affecting the reliability of the NNLS inversion. Figure 6.1-a presents the observed radial magnetic field, extracted from the global radial magnetic data of the Tsunakawa map (Tsunakawa et al., 2015) for the specified region. In Figure 6.1-b, the inversion algorithm, after selecting the best-fit uniform direction of magnetization for the surface dipoles, produces the best-fit model of the radial magnetic field at an altitude of 30 km. The difference in intensity of the radial magnetic field from model and observations are plotted in Figure 6.1-c.

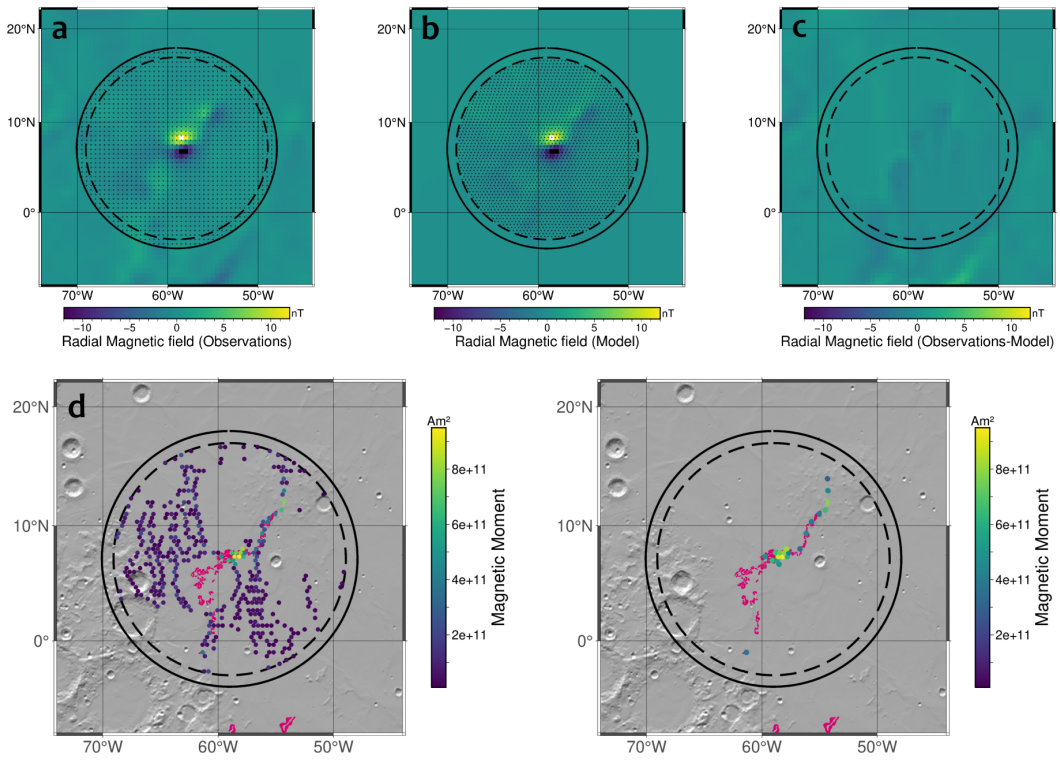

Figure 6.1: Sample output of the Parker Inversion method for the Reiner Gamma magnetic anomaly. Sub-figures on the top row display (a) the observed magnetic field, (b) the modeled magnetic field, and (c) the difference between the two, while (d) and (e) depict the surface distribution and intensity of surface magnetic dipoles, respectively considering dipoles above $m = 10^{10} Am^2$ and those stronger than 30% of m_{max}. The fuchsia markings delineate the shape of the Reiner Gamma swirl/albedo anomaly. Underlying is a relief map.

The surface dipole distribution and the magnetic moments of the dipoles that produce the best-fit scenario are plotted in the Figures 6.1-d and 6.1-e. The magnetic moment m indicates the intensity of the magnetization in the assigned dipoles and reflects on how strongly the surface material is magnetized The surface dipole disposition in Figure 6.1-d shows noticeable “holes” where dipoles are not placed: this is a consequence of the assumption of unidirectionality that is central in the Parker inversion method. Such gaps are found also in Oliveira et al. (2024), section 3.2.3, in which the performance of the Parker’s method is evaluated for two non-unidirectionally magnetized synthetic subsurface magnetic sources, a case that violates the key assumption of unidirectionality of the technique. The study finds that surface magnetization can be delineated when the differences in magnetization direction for the two sources are relatively small (up to around 90° difference). However, as the difference increases, holes and gaps similar to those seen in 6.1-d begin to appear. Consequently, such artifacts are expected when using the Parker Inversion method and also reflect the natural variability of crustal magnetization, as the actual magnetization direction is unlikely to be entirely uniform over a large area. The diverse geological processes and impact events that have shaped the Moon over time naturally contribute to a complex and heterogeneous distribution of magnetization directions, rather than a homogeneous one. Nevertheless, assuming unidirectionality remains a sufficiently valid approximation for the inversion method.

The strength of dipoles is measured using the magnetic moment m, measured in Am^2. In Figure 6.1-d, all the non-zero dipole moments with magnetic moment above $10^{10} Am^2$ (cutting on the weakest ones produced) are shown, to appreciate the overall surface distribution of dipoles. What is observed for the Reiner Gamma case is that the surface dipoles have a higher magnetic moment (thus magnetization) in correspondence of the stronger observed and modeled radial magnetic field (in absolute value) roughly at the center of the circle, extending to the north-east with an interesting linear formation. To note, if the inversion results indicated that the strongest dipole was positioned instead along

the perimeter of the inner circle, this would have suggested the presence of edge effects and a poorly chosen centering of the area of interest, though this is not the case for the output presented here. Looking at the overall distribution for the Reiner Gamma case, the dipoles clearly do not appear in some areas, forming holes. Figure 6.1-e focuses instead on delineating those dipoles with magnetic moment greater than 30% of m_{max}. The 30% of m_{max} threshold is derived from the findings in Oliveira et al. (2024), which demonstrate that dipoles retained using this threshold consistently align with the surface projection of the subsurface synthetic source of magnetized material. The Reiner Gamma histogram in Figure 6.8 shows the strength distribution of the dipoles and, in red, the threshold line is shown. While the choice of this threshold may seem arbitrary, its adoption is grounded in empirical evidence from Oliveira et al. (2024) study.

Finishing the description of Figures 6.1-d and 6.1-e, the fuchsia structure represents the albedo anomaly or swirl connected to the Reiner Gamma area. Only a subset of the analyzed anomalies exhibit swirls within their regions. When swirls are present, they will always be marked on the maps to allow for their assessment. It is evident how the magnetized material appears to follow closely the main central body of the swirl and its elongation in the north-east direction. The magnetized material goes beyond the limits of the north-eastern appendix of the swirl and ends deeper within the Marius Hill volcanic complex. The albedo anomalies in the southwest portion are not associated with any dipoles in this inversion. This is probably related to a different direction of magnetization compared to the central and northern anomalies, as will be discussed in Subsection 7.2.1.

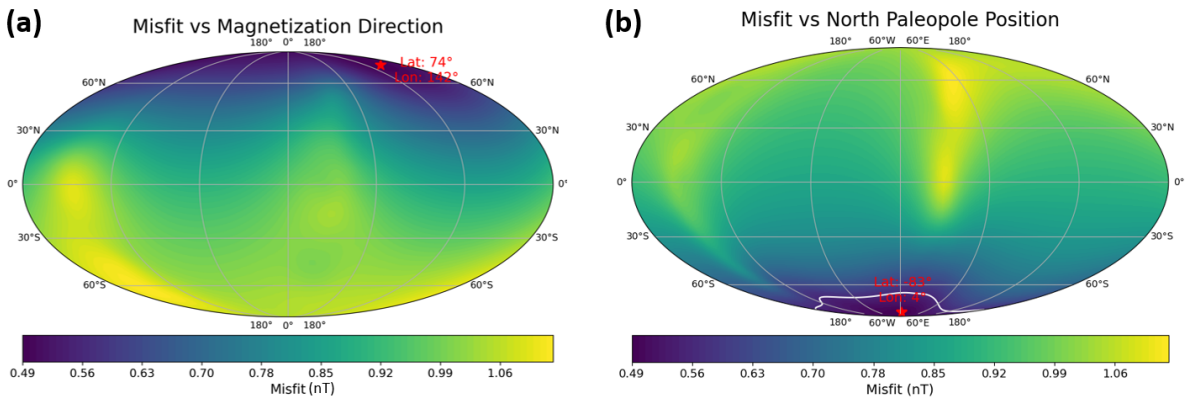

Figure 6.2: Inversion RMS misfit plotted versus the magnetization direction (with a 2° between latitudes and longitudes) and versus the north paleopole position corresponding to each magnetization direction.

To complete the range of outputs available, an interesting map is represented by the misfit vs. paleopole position map, created from the misfit vs. magnetization direction map. These two maps are shown in Figure 6.2. Panel A relates the inversion RMS misfit to the corresponding magnetization direction. The best-fit magnetization direction, marked with a red star, is that with the lowest RMS misfit. For Reiner Gamma, the best fit magnetization direction is tangential to the surface, pointing towards north. From this, making the strong assumption to be in the presence of a dipolar magnetic field, the north paleopole position can be inferred for each output magnetization direction. Panel B is generated accordingly, with the red marker indicating the best-fit north paleopole position of 83°S and 4°E. The average ambient value of 0.558 nT between the circles used to calculate the uncertainty for the position is found to be very close to the inversion RMS misfit of 0.489 nT, resulting in a very contained error ellipse.

6.2. Results for the investigated anomalies

The nomenclature and location of all the investigated anomalies is shown in the map in Figure 6.3, while the data relative to the area of interest used as input for the inversion is found in table 6.1. The

Label	Anomaly name	Center lat [°N]	Center lon [°E]	Angular radius obs [°]	Angular radius dip [°]
a	Hartwig	-8	281	11	10
b	Reiner Gamma	7	301	11	10
c	Rimae Sirsalis	-10.5	304.5	11	10
d	Airy	-18	3.5	9	8
e	Descartes	-10.5	16	9	8
f	Rimae Goclenius-Gutenberg	-7.5	40	9	8
g	Crozier	-15	52	9	8
h	Vega	-45	67	10	9
i	Abel	-30	87.5	9	8
j	Marginis King main	19.5	90.5	10.5	9.5
k	Marginis King Firsov	-1	115	11	10
l	Moscoviense	28	147	10	9
m	Dufay	12	172	8	7
n	SPA/Hopmann	-51.75	160	6.2	5.5
o	SPA/Vertregt	-21.5	173	10.5	9.5
p	SPA/Birkeland	-33	176.2	6.5	5.8
q	SPA/Walker	-22.5	195.5	7.2	6.5
r	Hayford-Krasovskiy	9.5	186	9	8
s	Orientale/Tsander-Mach	13	214	13	12
t	Orientale/Catena Michelson	-2.5	246	7	6
u	Orientale/Kolhörster	11	250	9.5	8.5
v	Orientale/Vallis Bohr	19	270	12	11
w	Gerasimovich	-19	237	12	11
x	Mendel-Rydberg	-49.8	265.4	9	8
y	Sylvester (North Pole)	79	273	11	10
z	South Pole	-89	140	11	10

Table 6.1: Input data for the magnetic anomalies analyzed, consisting of the latitude and longitude of the center point of the area of interest, and the angular radius of the observation and dipole areas.

alphabetic labeling begins with the Hartwig anomaly (approximately 80°W) and progresses in an eastward direction. To note, some names used in this work are newly proposed: such names are derived from nearby features such as craters or rilles, as no official designation was found in the literature. The selection of anomalies for the inversion is guided by the effort to focus on relatively isolated features, while avoiding those with weaker (approximately below 2 nT) signals. Despite these criteria, analyses for more complex regions were also undertaken, such as for the Marginis-King area (anomalies j, k) and the South Pole-Aitken basin area (anomalies m, n, o, p), to broaden the scope of the investigation and test the Parker inversion method to its limits. In total, 26 anomalies are analyzed. Of these, 6 are chosen to be shown in Figures 6.4 and 6.5 as representative of categories of anomalies with certain characteristics (shape, dimension, complexity, correlation with geological features). The rest of the outputs is grouped in Appendix A (Figures A.9 to A.15).

A variety of different morphologies is observed in the output surface disposition of magnetized material when looking at the strongest dipoles, often reflecting the relative shape of the anomaly seen from the magnetic field map at 30 km altitude. The shape of the surface dipole configurations can be categorized into three distinct morphologies: elongated, localized/clustered and diffuse. Hartwig (Figure 6.4-a) is a clear example of the elongated morphology: the surface dipoles extend from south-west to north-east and are all found within an approximately rectangular area. Other examples are Reiner Gamma (b), Rimae Sirsalis (c), Rimae Goclenius-Gutenberg (f), Vega (h) and Abel (i). This group also exhibits diversity in the maximum local radial magnetic field, with higher values for Reiner Gamma (13.6 nT) and Abel (10.7 nT), and lower values for Rimae Goclenius-Gutenberg (3.44 nT). Additionally, there is variation in the predominant component of the radial magnetic field, with examples of anomalies displaying a predominantly positive radial magnetic signal, such as Hartwig and Abel, predominantly negative signals, such as Rimae Sirsalis and Vega, and both positive and negative signals, as seen in Reiner Gamma. Localized/clustered shapes are often found for small and isolated cases of anomalies: Crozier (Figure 6.4-g) is a clear example of that. The majority of the strongest surface dipoles are found within a small angular radius from the center of the anomaly. Airy (d), Descartes (e) and Dufay (m) are all anomalies sharing similar shape of surface distribution of the strongest magnetic dipoles. Of these, Descartes, a relatively contained and isolated magnetic anomaly, presents the strongest radial magnetic field signals in the lunar nearside (16.5 nT). It's important to understand that large and/or more

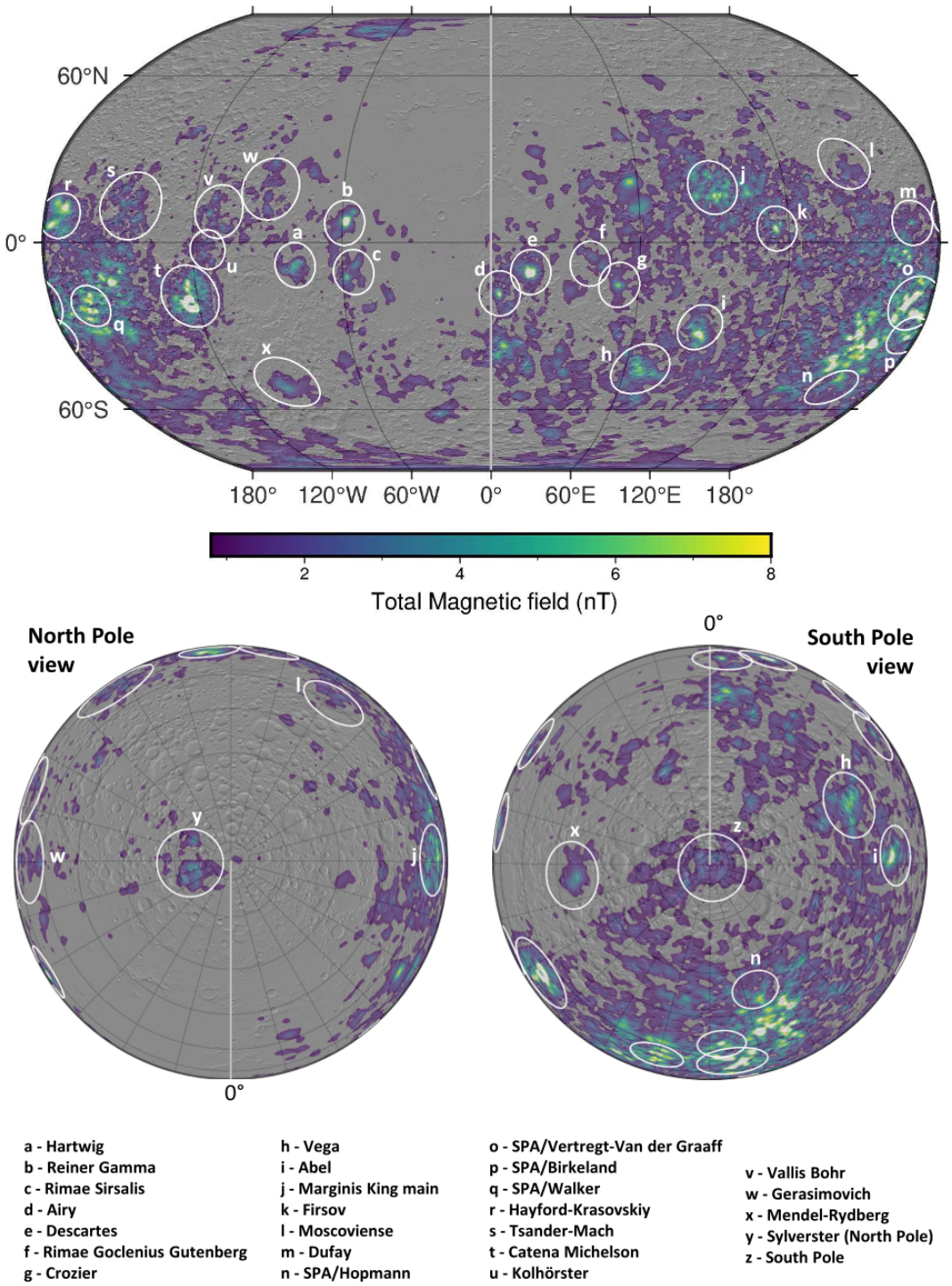

Figure 6.3: Global, North Pole, and South Pole views of the total magnetic field from the Tsunakawa map at an altitude of 30 km, overlaid on a relief map, with labels identifying all analyzed magnetic anomalies.

complex anomalies can be composed of multiple compact and blob-like smaller anomalies. This is the case sometimes for the more diffuse morphologies observed, such as the Marginis-King area shown in Figure 6.5-j and the South Pole-Aitken basin area (anomalies m, n, o, p in the Figures A.11 and A.12 in Appendix A). Another way to differentiate the output distribution of surface dipoles is by analyzing their correlations - typically with large crater structures, rilles, and swirls - or their lack of correlation with any

specific feature. Mendel-Rydberg, shown in Figure 6.4-x is a Nectarian-aged multi-ring impact basin found south of the Orientale basin that shows a central magnetic anomaly with the strongest signals and dipoles observed within the south-western portion of the inner depression. Moscoviense (l) is a similar example, while Rimae Sirsalis (c) shows good correlation with the homonym 400 km-long rille. Swirls, or albedo anomalies, are found in correspondence or proximity of a number of analyzed areas: Crozier (g) shown previously, but also Rimae Sirsalis (c), Airy (d), Rimae Goclenius-Gutenberg (f), Abel (i), Moscoviense (l), Dufay (m) and the more complex Marginis-King and SPA areas present these enigmatic surface features. For these latter 2 cases, the conducted inversions interest non-isolated and non-compact anomalies, pushing the Parker inversion method to its limits and possibly beyond its capabilities. The ambiguous correspondence between the surface distribution of dipoles and the observed magnetic anomaly, as shown in Figure 6.5-j — an inversion area on the far side encompassing multiple strong positive and negative radial anomalies — illustrates one such attempt. Two additional distinctive peculiar examples are shown in this six-case panel: the more isolated North Pole anomalies, of which Sylvester is the most prominent, and the weak but spatially extensive South Pole anomalies (Figures 6.5 y and z). These two polar regions are overall interested in anomalies of medium to low radial intensity and the distribution output is composed of few isolated surface magnetized areas in the case of the North Pole anomalies, whereas a more complex pattern is obtained in the case of the South Pole anomalies. The output data for each case is shown in the table in Figure 6.6. This table collects a series of parameters that can be used to compare the various inversions:

- The first two numerical columns collect the maximum absolute radial magnetic field for each area of interest and the relative maximum magnetic moment resulting from the inversion, respectively. The former is then used for the normalization of the misfit, while the latter is an output parameter that is necessary for the definition of the threshold for the map of the strongest dipoles. It is clear how a positive linear relationship exists between the 2 quantities: high values of radial magnetic field correspond high values of magnetic moments;
- The RMS Misfit column is generally low for weak anomalies and on the higher end for stronger anomalies. Instead, when the ratio of RMS Misfit and the maximum absolute radial magnetic field is considered, the now normalized cases can be compared: it is evident how isolated anomalies represent the best inversion cases, presenting lower values of normalized RMS Misfit, whereas magnetically complex areas such as the SPA regions and the Marginis-King regions are corresponded by higher values;
- The quality of the observed normalized paleopole uncertainty relative to the determined paleopole position is closely correlated with the results for the normalized RMS Misfit. Being calculated as the average radial magnetic field value within the annular region between observation and dipole areas, the best outcomes are once again achieved for the more isolated anomalies, where the risk of capturing interference from strong anomalies within the circles is minimal.

The sixth and seventh numerical columns of the output data table represent the latitude and longitude of the best-fit paleopole position. As a reminder, these values are derived under the assumption of a dipolar magnetic field. Rather than presenting the paleopole positions of the six representative anomalies discussed earlier, selected primarily to showcase the variety of inversion results, this paragraph focuses on the paleopole positions of anomalies that may be linked to the Imbrium impact event, as proposed by Hood, Torres, et al. (2021). Figure 6.7 shows the best-fit paleopole position and the relative uncertainty for the Hartwig, Reiner Gamma, Rimae Sirsalis, Airy, Descartes, Rimae Goclenius-Gutenberg, Crozier, Vega and Abel anomalies. No clustering of paleopole positions is observed, with best-fit results covering all latitudes and longitudes. Uncertainty circles are tighter for stronger and isolated anomalies (especially for Reiner Gamma and Descartes, but also for Abel and Hartwig to a lesser extent) whereas they extend to almost half of the globe in other cases.

Lastly, Figure 6.8 shows the strength distribution of the magnetic moments for all the retained non-zero dipoles for the inversions of the 9 Imbrium-related magnetic anomalies. What can be observed is that the strong anomalies produce fewer dipoles with high magnetic moment and these dominate the 30% of m_{max} retaining threshold: indeed, both for Reiner Gamma and Descartes, the number of retained dipoles is contained also because of this reason.

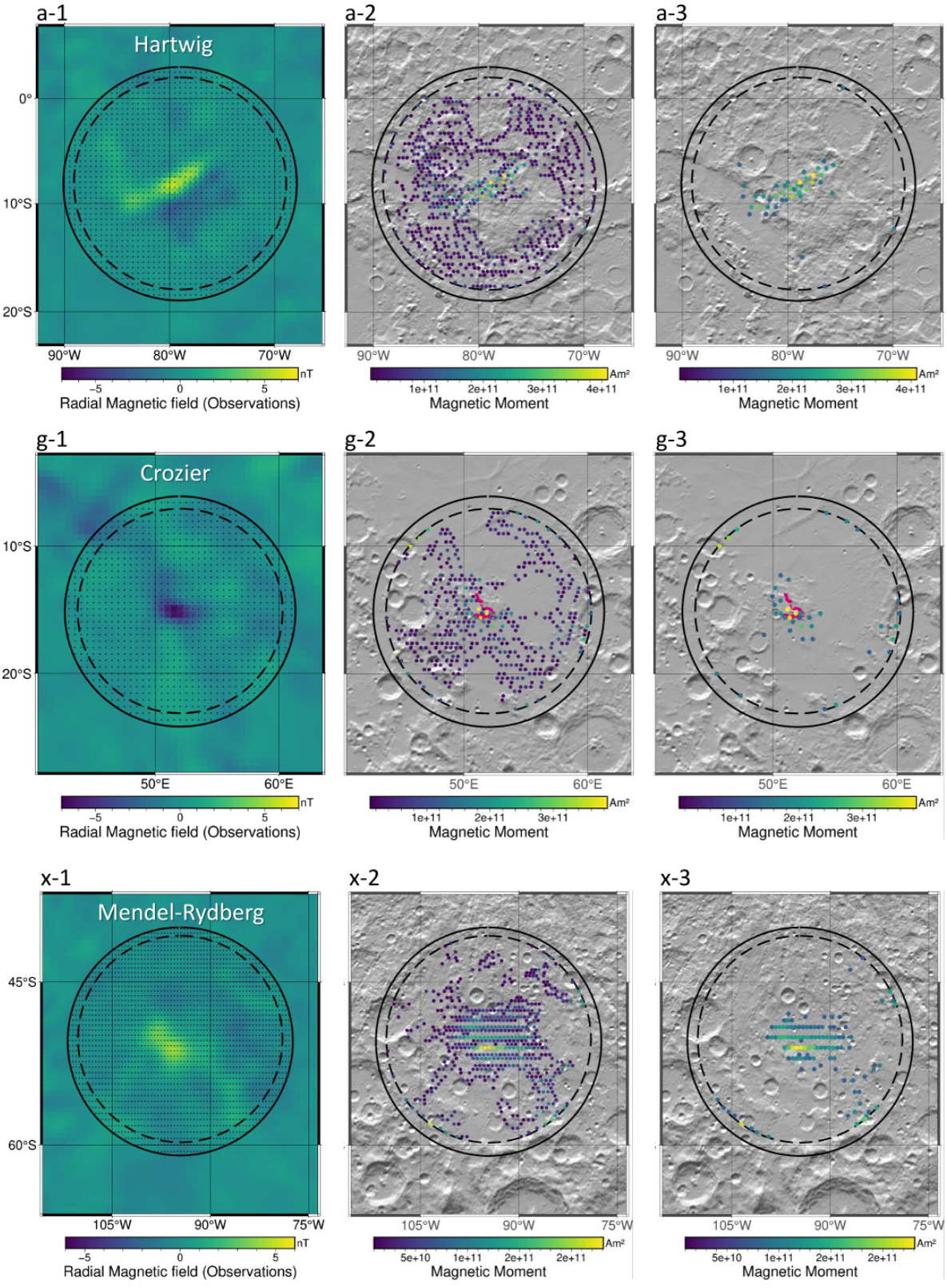

Figure 6.4: This two-Figure panel shows the observed magnetic field [1] and the surface distribution of magnetized material (all dipoles above $10e^{10} Am^2$ [2] and those stronger than 30% of m_{max} [3]) for 6 out of the 26 investigated magnetic anomalies. More cases are found in the appendix, in figures A.9, A.10, A.11, A.12, A.12, A.13, A.14, A.15. The letters correspond to the labeling as seen in Figure 6.3. All the maps are in Mercator projection.

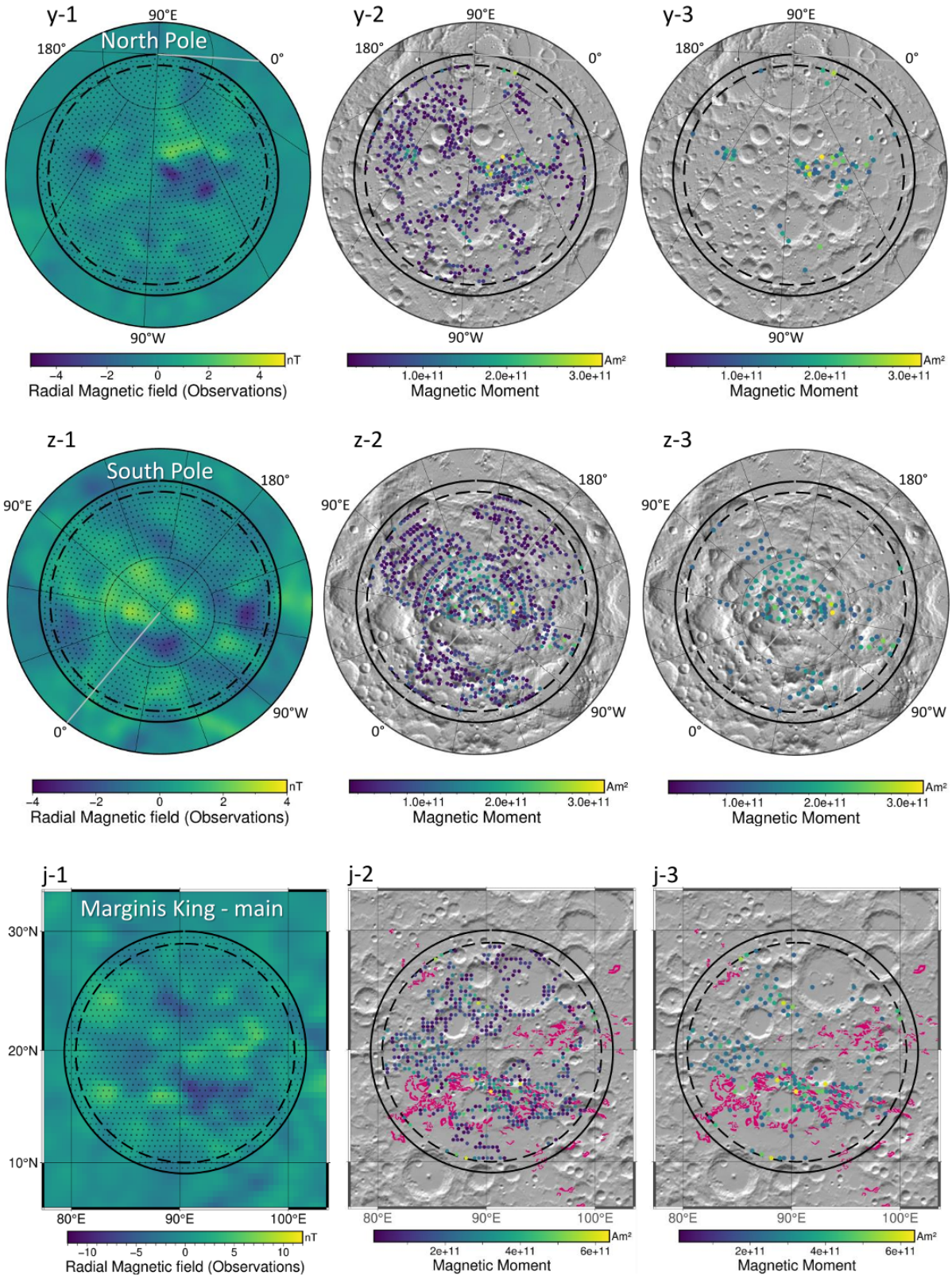

Figure 6.5: Same as Figure 6.4 but for regions y, z and j. Polar regions y and z are shown with the Lambert Azimuthal Equal Distance projection, while for region j the Mercator projection is kept.

Label	Magnetic anomaly	B_rad_abs_max from observations (nT) [1]	M_max (x10^{+1} Am^2)	RMS Misfit (nT) [2]	RMS Misfit normalized (nT) [=2/1]	Non-zero dipoles/Total number of dipoles (%)	Best-fit paleopole latitude (°N)	Best-fit paleopole longitude (°E)	Paleopole uncertainty (nT) [3]	Paleopole uncertainty normalized (nT) [=3/1]
a	Hartwig	5.53	4.1	0.219	0.0396	33.9	-34.3	347	0.362	0.0655
b	Reiner Gamma	13.6	9.50	0.49	0.0360	18.7	-83.5	4.02	0.558	0.041
c	Rimae Sirsalis	6.28	3.48	0.291	0.0463	30.7	-9.67	72.6	0.379	0.0604
d	Airy	8.14	5.74	0.313	0.0385	28.7	-39.6	162°	0.467	0.0574
e	Descartes	16.5	12	0.454	0.0275	22.9	15.9	277	0.653	0.0396
f	Rimae Goclenius-Gutenberg	3.44	2.86	0.256	0.0744	28.0	32.8	197	0.387	0.113
g	Crozier	6.63	3.85	0.289	0.0436	31.0	66.1	187	0.504	0.076
h	Vega	6	4.88	0.639	0.1065	28.1	88.2	67	0.818	0.136
i	Abel	10.7	5.91	0.464	0.0434	30.4	36.5	111	0.683	0.0638
j	Marginis King main	7.84	6.37	1.02	0.130	24.3	-15.9	203	1.11	0.142
k	Marginis King Firsov	10.5	7.44	0.494	0.0470	27.0	30.8	254	0.811	0.0772
l	Moscoviense	2.82	2.72	0.297	0.105	25.5	-74.2	233	0.359	0.127
m	Dufay	5.93	5.24	0.469	0.0791	6.93	31.5	83	0.6	0.101
n	SPA/Hopmann	6.7	9.05	0.761	0.114	6.42	10.5	245	0.976	0.146
o	SPA/Vertregt	16.4	13.4	1.27	0.0774	28.3	-29.8	354	2.08	0.127
p	SPA/Birkeland	11.8	8.04	0.924	0.0783	13.1	10.7	114	1.61	0.136
q	SPA/Walker	10.2	13.4	1.5	0.147	12.1	-51	23.7	2.19	0.215
r	Hayford-Krasovskiy	9.63	12.5	0.694	0.0721	37.1	22.1	99.9	0.558	0.058
s	Orientale/Tsander-Mach	4.4	4.83	0.405	0.0920	21.9	-35	277	0.416	0.0945
t	Orientale/Catena Michelson	2.88	4.31	0.425	0.148	21.1	43.6	349	0.493	0.171
u	Orientale/Kolhörster	4.42	3.62	0.27	0.0611	27.5	-38.9	357	0.414	0.0937
v	Orientale/Vallis Bohr	3.32	3.39	0.278	0.0837	28.2	-61.2	4.31	0.435	0.131
w	Gerasimovich	23.5	26.5	0.852	0.0363	22.9	-59.9	83.8	0.937	0.0399
x	Mendel-Rydberg	4.16	2.53	0.196	0.0471	32.7	-1.06	315	0.13	0.0313
y	Sylvester (North Pole)	3.92	3.14	0.257	0.0656	24.2	-36.8	271	0.329	0.0839
z	South Pole	3.05	3.19	0.414	0.136	31.0	-19.7	216	0.476	0.156

Figure 6.6: This table presents a compilation of output parameters derived from the inversions performed on 26 magnetic anomalies. The color scales applied to the data are based on a relative comparison of the values and are intended to visually distinguish between lower and higher values. These distinctions provide an intuitive guide for interpreting the outputs.

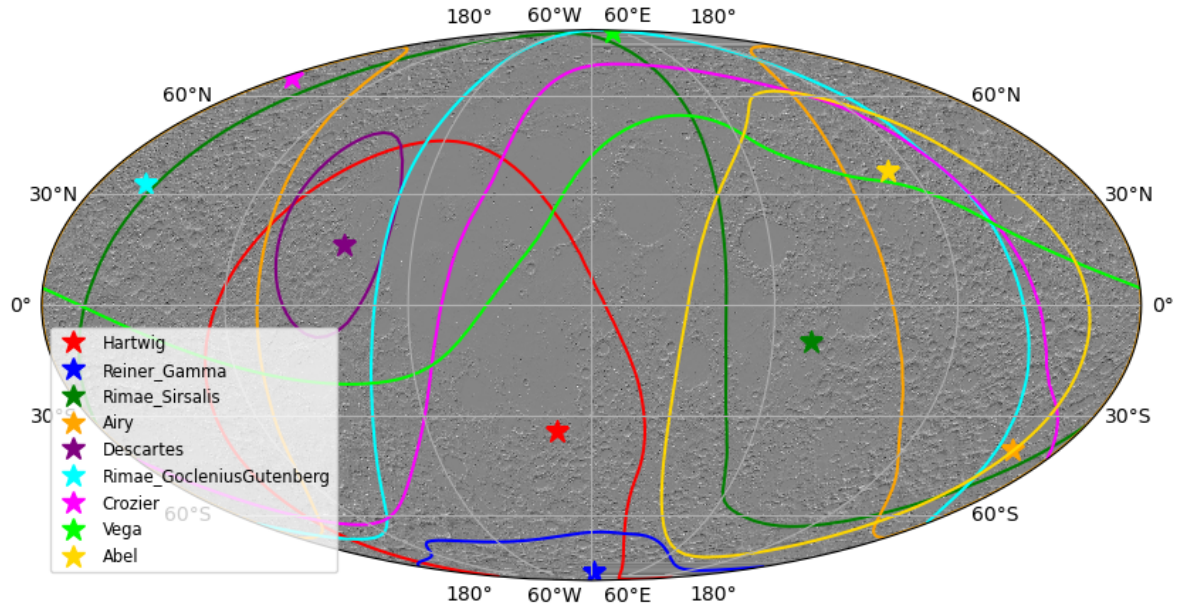

Figure 6.7: Map of best-fit paleopole positions (indicated with stars) and the relative uncertainties (indicated with a line of the same color of the star) for anomalies possibly related to the Imbrium impact (as suggested by Hood, Torres, et al., 2021).

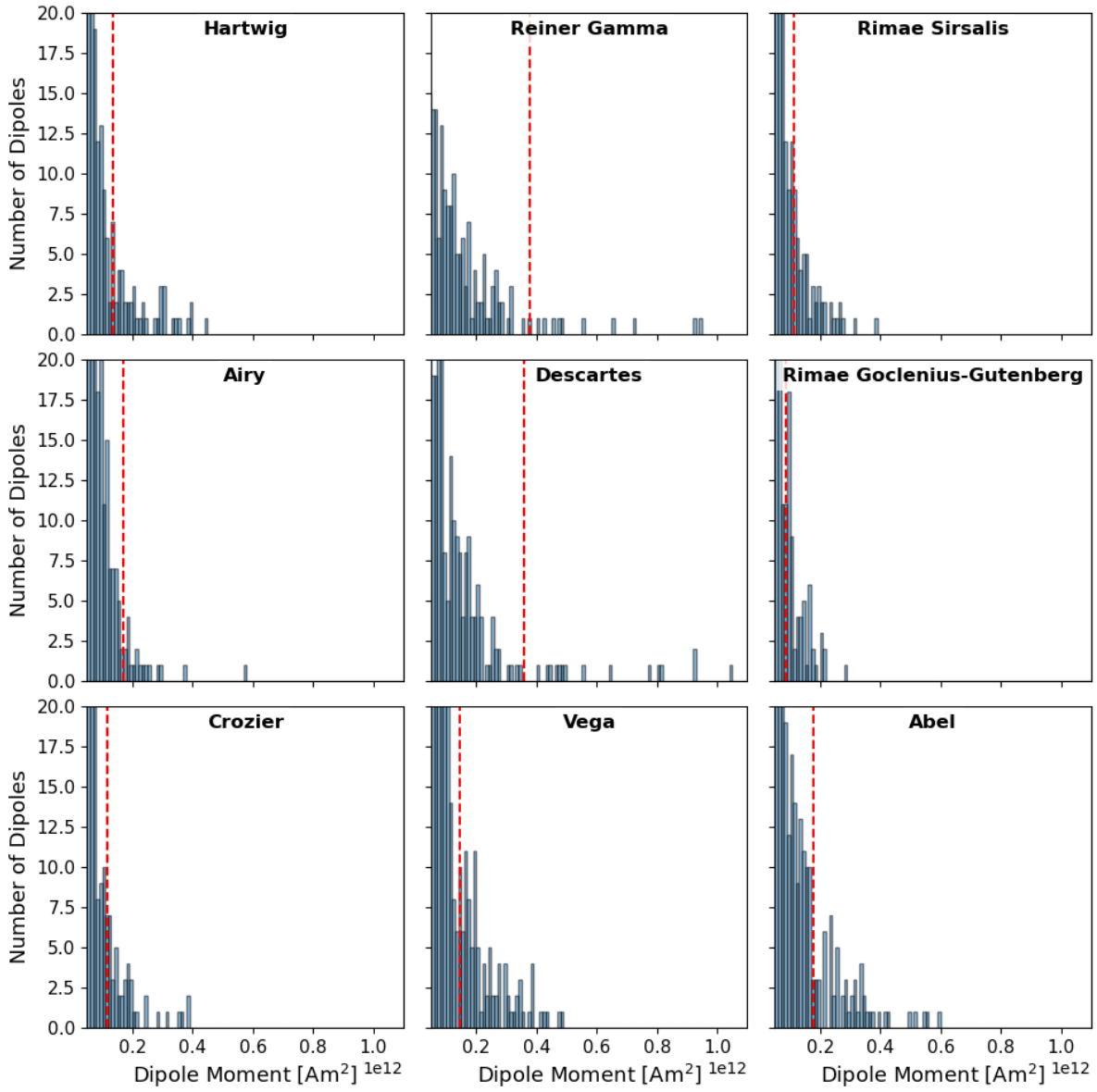

Figure 6.8: Histograms representing the strength distribution of output dipoles for the anomalies related to the Imbrium basin. The red dotted line represent the cutoff value of 30% of m_{max} used to retain the strongest dipoles. The x-axis ranges from $0.5 * 10^{11}$ to $1.1 * 10^{12}$.

7 Discussion

In this Chapter, I explore the meaning of the results obtained in this work, focusing on the large impact processes (ejecta and antipode). I also tackle how magnetization distribution correlates with swirls formations. I complete this discussion by making a general comparison of different processes that might play a role in magnetic anomalies sources formation.

7.1. Are lunar magnetic anomalies sources related to large-impact events?

Large impacts on the Moon have shaped much of its surface geomorphology, leaving behind a legacy of geological features, including craters, basins, and ejecta deposits, while also influencing the surface composition. The peculiar distribution of strong magnetic anomalies - particularly the large and complex structures on the lunar far side - has drawn significant scientific interest since the first global magnetic data became available (e.g., Hood et al., 2001, Richmond et al., 2005). Many of these anomalies are located antipodal to some of the Moon's youngest and largest basins, while others exhibit radial alignment with major impact structures and suggest an ejecta origin. These patterns strongly suggest that impacts have played a key role in shaping the Moon's crustal magnetic field (e.g., Hood and Vickery, 1984, Hood et al., 2001), a hypothesis further examined in this study. This section examines the correlation between surface magnetized material and a potential ejecta or antipodal origin for certain anomalies, which has been hypothesized in previous work (Hood & Artemieva, 2008; Hood, Torres, et al., 2021).

7.1.1. Ejecta Origin: What is the correlation between magnetized material and the Imbrium and Orientale impact basins?

The possible ejecta origin for a number of anomalies in the lunar near-side is evaluated by comparing the orientation of the surface distribution of the magnetized material (in practice distribution of the strongest magnetic dipoles) to the possible position of ejecta from two of the youngest and largest impact basins, Imbrium and Orientale. In particular, great circle paths proposed by Hood, Torres, et al. (2021) as possible ejecta pathways are considered. Figure 7.1 shows the Imbrium impact basin and its antipode with the five proposed circle paths (ejecta pathways). The primary distinction between the results of Hood, Torres, et al., 2021 and this study lies in the focus of the analysis. Contrary to Hood, Torres, et al. (2021), which examined magnetic anomalies signals, this work takes a step further by determining the surface distribution of the magnetized material (in other words, of the magnetic anomalies sources themselves). Magnetic anomalies observed in maps at 30 km altitude often appear as

“amorphous blobs”, making it difficult to accurately evaluate their structure and alignment. The issue is bypassed by determining the surface distribution of the magnetized material, giving strong evidence of possible alignments if any is to be found.Another relevant difference is the selection of different magnetic field maps, specifically the map built by Hood, Torres, et al. (2021) and the map employed in this study. For more details on the magnetic field maps differences, see Chapter 3.

The magnetic anomalies considered in the correlation investigation for the Imbrium impact basin include the trio found southwest of the crater, comprising Reiner Gamma, Rimae Sirsalis, and Hartwig, as well as the group in the southeast, more spread out and consisting of Airy, Descartes, Rimae Goclenius-Gutenberg, Crozier, Abel, and Vega. Figure 7.1 overlays the output surface dipoles from this work onto a semi-transparent Tsunakawa magnetic map and a topography map. To note, the figure implements an area-specific color scale for the dipoles, as a global color scale would cause the higher magnetic moments from the Descartes and Reiner Gamma areas to overshadow those with weaker values. Thus, we focus on the direction of the strongest dipoles for each area independently, enabling clear observation of the directional trends for all areas. For completeness, the version showing a global and unique color scale for the output dipoles is shown in Figure A.16 in Appendix A.

Starting from the trio of anomalies in the southwest (Reiner Gamma, Rimae Sirsalis and Hartwig), it is observed that the strongest dipoles of both the Hartwig and Rimae Sirsalis anomalies follow closely the respective proposed great circle ejecta paths, while Reiner Gamma dipoles slightly deviates towards a more northern direction when looking at its north-eastern extension, but overall fits very well with the position of the great circle. Considering the degree of spatial alignment observed and the proximity of the anomalies between each other, a common ejecta origin is very likely. Several independent studies have proposed a north/northwest to south/southeast trajectory for the Imbrium impactor. Schultz and Crawford (2016) derived this direction by analyzing groove orientation, ejecta concentration, and basin asymmetries. Hood, Torres, et al. (2021) reached the same conclusion by examining the distribution and orientation of magnetic anomalies, while Wieczorek et al. (2012) found that gravity anomalies also align with this trajectory. Given this proposed impact direction and an angled strike, magnetized ejecta should be present - and likely concentrated - southeast of the Imbrium basin.

To assess this hypothesis, we now turn to the magnetic anomalies in the region southeast of the Imbrium basin (see Figure 7.1) and evaluate their consistency with the inferred impact trajectory. It’s important to understand that some of these anomalies, particularly Airy, Descartes, and Abel to a lesser degree, present a compact and clustered shape compared to the more elongated Vega and Rimae Goclenius-Gutenberg anomalies, both when looking to the main body of the total magnetic anomaly at 30 km altitude and when considering the surface dipoles obtained from the inversion. Thus, what can be said for such compact-shape cases is that the dipoles are found to lie in proximity of the proposed great circle paths, but little information about a preferred orientation can be discerned. Two of the three remaining anomalies, Rimae Goclenius-Gutenberg and Crozier, are adjacent to one another, forming a sort of wake-like feature, and share a common orientation that aligns with the corresponding great circle path. Finally, the more southern Vega presents dipoles organized in a preferential orientation that is around 30°/40° tilted to the north compared to the relative circle path.

Overall, a common ejecta origin from the Imbrium crater for all the analyzed anomalies remains plausible and, if true, would support the NW to SW direction of the Imbrium impactor. The differences in correlation with the great circle paths can be attributed to factors such as the variable size, shape, and composition of the ejecta, as well as the interaction with later events such as minor impacts and mare formation, which may have altered the distribution and characteristics of the anomalies. It is important to note that other relatively young Nectarian basins (3.92 to 3.85 Gyrs) could also be potential sources of ejecta for these near-side anomalies. Their formation closely precedes that of the Imbrium and Orientale basins, which are typically classified as early Imbrian (3.85 to 3.8 Gyrs). The primary candidates include the Crisium, Serenitatis, and Nectaris basins, all located between longitudes 0° and 60°E. Serenitatis is a 900 km-wide basin adjacent to Imbrium; Nectaris, more to the east, is a large 850 km-wide crater situated 15° south of the equator; further to the east and 15° north of the equator is Crisium, with a diameter of 750 km. Notably, all three basins, particularly Serenitatis and Crisium, exhibit strong magnetization at their antipodes, suggesting that the impacts had far-reaching effects:

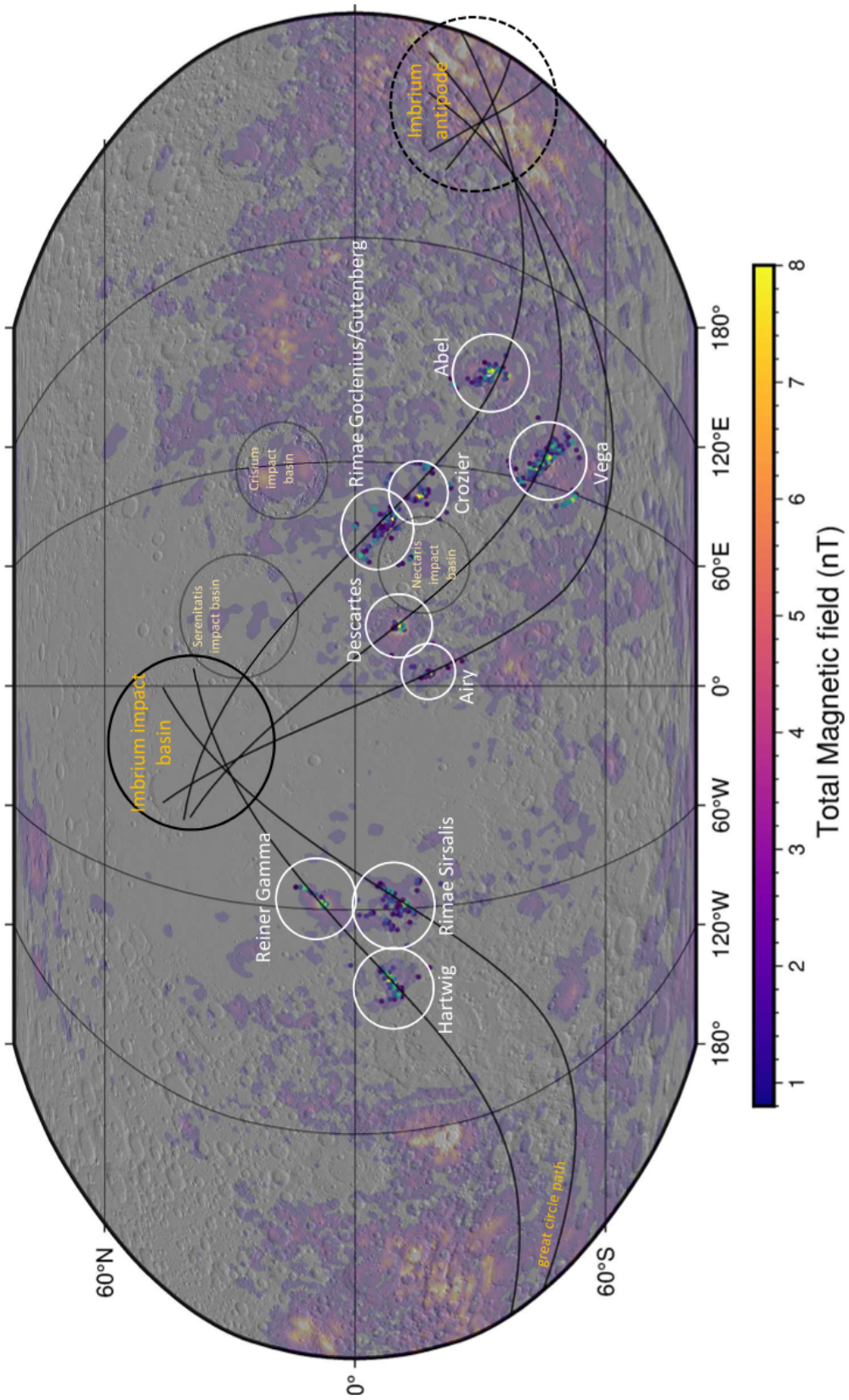

Figure 7.1: Global map showing the direction of the strongest dipoles from inversion outputs for several near-side anomalies as compared to the Imbrium-related great circle paths proposed from Hood, Torres, et al. (2021). Underlain, the Tsunakawa magnetic map and a relief map.

given this, it is plausible that correspondent ejecta also played a significant role in the observed magnetization. Regarding the possible correlation with the magnetized material, the observed alignment of the anomalies could suggest a connection to the Serenitatis basin, given its similarities in size, location, and age to Imbrium. However, its older age, smaller dimensions, and slightly less favorable alignment make Imbrium the more likely source. The Nectaris impact event, on the other hand, could be the source of anomalies such as Descartes, Airy, and possibly some yet-to-be-investigated weaker boreal anomalies. However, the apparent wake-like ejecta patterns associated with the Crozier, Rimae Goclenius-Gutenberg, Abel, and Vega anomalies do not align well with the center of the Nectaris Basin. Instead, they suggest a more western origin, likely from Imbrium or Serenitatis. Finally, the more northern Crisium basin does not appear to align well with most of the analyzed anomalies, except for Abel and Vega.

One other Imbrian-aged basin, more to the west, is particularly interesting for the link of an ejecta origin for anomalies surrounding its crater: the Orientale basin. A similar map and analysis to that conducted for the Imbrium basin is now presented, focusing on potential ejecta pathways radiating from the Orientale impact site. Figure 7.2 is a section of the global map that focuses in the area north/northwest from the basin. The intensities of surface dipoles are once again plotted without sharing a uniform intensity scale. The group of anomalies analyzed comprises Catena Michelson, Kolhörster, Tsander-Mach and Vallis Bohr (all proposed names). The stronger surface dipoles across all four cases lack a well-defined direction, especially for the Tsander-Mach and Kolhörster anomalies. Looking at the proposed great circle paths, the strongest dipoles align more closely with those heading north and northwest, compared to pathways extending more directly westward. Stronger anomalies are observed to the west of the crater, but these are not considered as candidates for Orientale ejecta, as they are more closely associated with the antipodal regions of the Serenitatis and Crisium basins (see the global map of basin antipodes in the next section, Figure 7.3). Reiner Gamma, Hartwig, and, to a lesser extent, Rimae Sirsalis, located just northeast of the basin, also show a radial alignment with the Orientale formation. However, these anomalies were not included in the group potentially linked to the Orientale impact event. This decision is based on the observation that they would be the only strong anomalies radially aligned with Orientale, whereas several others are aligned with Imbrium, suggesting an Imbrium-related origin for these three magnetic sources. Additionally, Rimae Sirsalis, which is likely connected to the other two anomalies, shows a weaker alignment to Orientale. Nevertheless, an Orientale-related origin for this trio of anomalies cannot be entirely excluded.

Overall, despite the general weaker correlation between magnetized material and radial alignment to the Orientale crater (compared to Imbrium), an ejecta origin for the analysed anomalies still remains plausible. Such an origin would support the hypothesis of an impactor striking at an oblique angle from SE to NW, consistent with the hypothesis of Hood, Torres, et al. (2021) based on the orientation of magnetic anomalies from the Hood's map. However, such interpretation contrasts with the direction suggested by Morse et al. (2018), who inferred a SW to NE trajectory by analyzing the bilateral distribution of ballistic and "rich of impact melt" ejecta deposits. The latter proposed trajectory would better align with this study's results if the strong anomalies of Reiner Gamma and Hartwig were to be included in the analysis. An additional piece of evidence supporting the proposed ejecta origin of selected anomalies from Imbrium and Orientale is the statistically significant correlation between these anomalies and the respective craters. This relationship was verified through Monte Carlo simulations that assessed the likelihood of chance alignment, as conducted by Hood, Torres, et al. (2021).

When assessing the radial alignment of anomalies with young, large impact basins, another less-explored hypothesis should be considered: the energy from a major impact may have generated radial tectonic fractures, which later facilitated the intrusion of magma that, once solidified under a steady ambient field, became the source of the anomalies. For example, dike-like magnetic sources have been proposed for the Rimae Sirsalis anomaly (Srnka et al., 1979), produced by the nearby extensional graben thought to be formed from lithospheric stress related to the Imbrium impact (although others better correlate the anomaly to smooth plains interpreted as a basin ejecta unit). The issues that this tectonic hypothesis face include the very low iron content found in recovered basalt samples (approximately 0.08 wt%), which might be insufficient to generate a magnetic anomaly, though Hemingway and Tikoo (2018) suggest it could be enriched to 1%. Additionally, a significant problem related

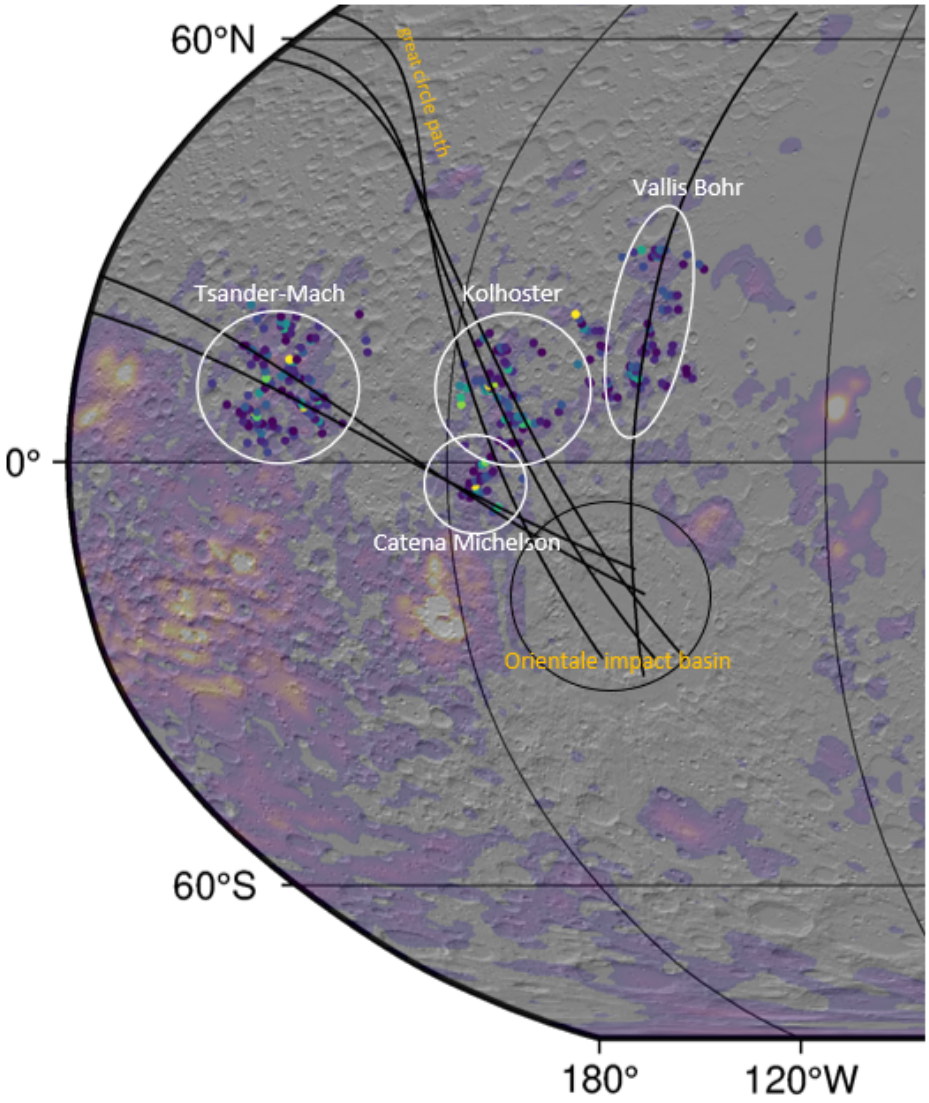

Figure 7.2: Map of the Orientale basin, the anomalies analyzed and their correlation with the proposed ejecta pathways departing from the crater proposed by Hood, Torres, et al. (2021)

to the analysis here conducted is the considerable distance of some investigated anomalies from the impact basin (Vega and Abel for example are located approximately 3250 and 3500 km from the center of the Imbrium crater), making it less plausible that they could have experienced large-scale tectonic alterations at such lengths.

An idea to analyze the plausibility of the tectonic origin is to look at the best-fit north-paleopole position for the interested anomalies. It is important to note that interpreting the paleopole results requires assuming the presence of a global dipolar magnetic field at the time of the impact. As dipolar, this field would have most probably had a core-dynamo origin, and could have been either weak, strong, or even temporarily amplified by the impact event. To observe the map of the best-fit north paleopole position vs. inversion misfit for the Imbrium-related anomalies, let's refer to Figure 6.7 in the Results chapter. Taking the example of the equatorially placed Reiner Gamma anomaly, the best fit magnetization direction is tangential to the surface, pointing toward north (misfit vs. magnetization direction map for Reiner Gamma is shown in Figure 6.2 at the top). This result leads to the geometric inference that the north geomagnetic paleopole is situated near the south geographic pole (using modified equations from Butler, 1992), a finding that, isolated from the others, seems consistent with the hypothesis of an

ancient global core-dynamo aligned with the Moon's rotation axis. Vega is the only other anomaly with a clearly polar best-fit position for the north paleopole, found opposite to the Reiner Gamma one, near the north geographic pole. All the other anomalies show north paleopole positions not aligned with the rotation axis of the Moon. The Descartes anomaly presents a fairly small error ellipse, with the best-fit North paleopole position placed at to 16°N - 83°W, while for most of the other cases, almost half of the planet can fit the data using our definition of uncertainty. What would be expected if the cracks originated from the same Imbrium impact and became magnetized shortly after (by the cooling of intrusive ferromagnetic material under a dipolar magnetic field) would be a cluster of similar positions for the north paleopole for at least the majority of the Imbrian related anomalies, which is not observed. Nevertheless, such hypothesis could still be possible if we consider more complex settings. For example, the fractures (hence the magnetic anomalies) could have originated from different impact events. Another possibility could be that the fractures were created by the Imbrium impact but subjected to intrusive magmatism at different times in lunar history, which could account for the different paleopole positions observed (as the axis of the magnetic field could migrate). However, it is unlikely that they would experience such drastically different orientations for a dipolar magnetic field. One more possibility is that the magnetic field is not dipolar but multipolar. Following this theory, the obtained paleopole position would lose meaning. Therefore, even though the tectonic origin / magmatic intrusion scenario cannot be ruled out, this hypothesis is unlikely in comparison to the ejecta origin.

After investigating the ejecta and tectonic origin, a question that naturally arises is what may be the origin of all the other anomalies that have not been considered and that do not show any particular alignment with major craters. The presence of multiple relatively young impact events (Imbrian and Nectarian aged) from which impact ejecta could have originated (and then magnetized) could explain the origin of most of the nearside anomaly, while for the large and complex areas in the far side, we should look at antipodal magnetization for those same impact basins, as they match surprisingly well with the magnetic anomalies.

7.1.2. Antipodal origin: what is the correlation between magnetized material and areas opposite to large impacts?

If the impact event is large enough, ejecta, together with shock waves and a partially ionized melt cloud can reach and concentrate at the antipodal area from where the collision takes place, generating or amplifying, in some conditions, a magnetic field (Hood & Artemieva, 2008; Hood & Vickery, 1984; Narrett et al., 2024). Results of the correlative study between areas antipodal to large impact craters and the distribution of surface magnetic dipoles are now presented.

Before looking at the antipodes of major basins, let's first briefly discuss the distribution of large craters and their correlation with magnetic anomalies. Figure A.17 in Appendix-A shows the global distribution of lunar impact craters above 200 km in diameter compared to the Tsunakawa magnetic map at 30 km altitude. Overall, most craters show no significant magnetic signatures. However, some do exhibit magnetic features within the main rim, prompting studies such as Oliveira et al. (2017a) and Yang and Wieczorek (2024), which explored their potential connection to the lunar dynamo.

The ability of a lunar impact to induce changes at its antipode depends on several factors, including the impactor's energy, velocity, angle, and composition. As a result, the exact threshold diameter for such effects is not well-defined. However, it is generally assumed that basin-forming impacts - those exceeding 300 km in diameter, as defined in Kiefer (n.d.) - are sufficient to produce antipodal alterations. The 300 km diameter can be considered a conservative value, as some studies simulating large impact effects at the antipodes have used diameters of 100 km as in Wakita et al. (2021), 120 km in Oran et al. (2020) and 240 km in Hood and Artemieva (2008). The map in Figure 7.3 shows the correlation between areas antipodal to large impact craters and basins over the Tsunakawa magnetic field map. A striking observation is that the antipodal regions of Imbrian-aged impacts, as well as some late Nectarian events, correspond to the strongest magnetic formations in the lunar far side: this is especially the case for the Imbrium, Serenitatis, Crisium and Orientale antipodes. Large antipodal areas in the nearside are instead fewer, more sparse and more weakly correlated to magnetic anomalies: it's the

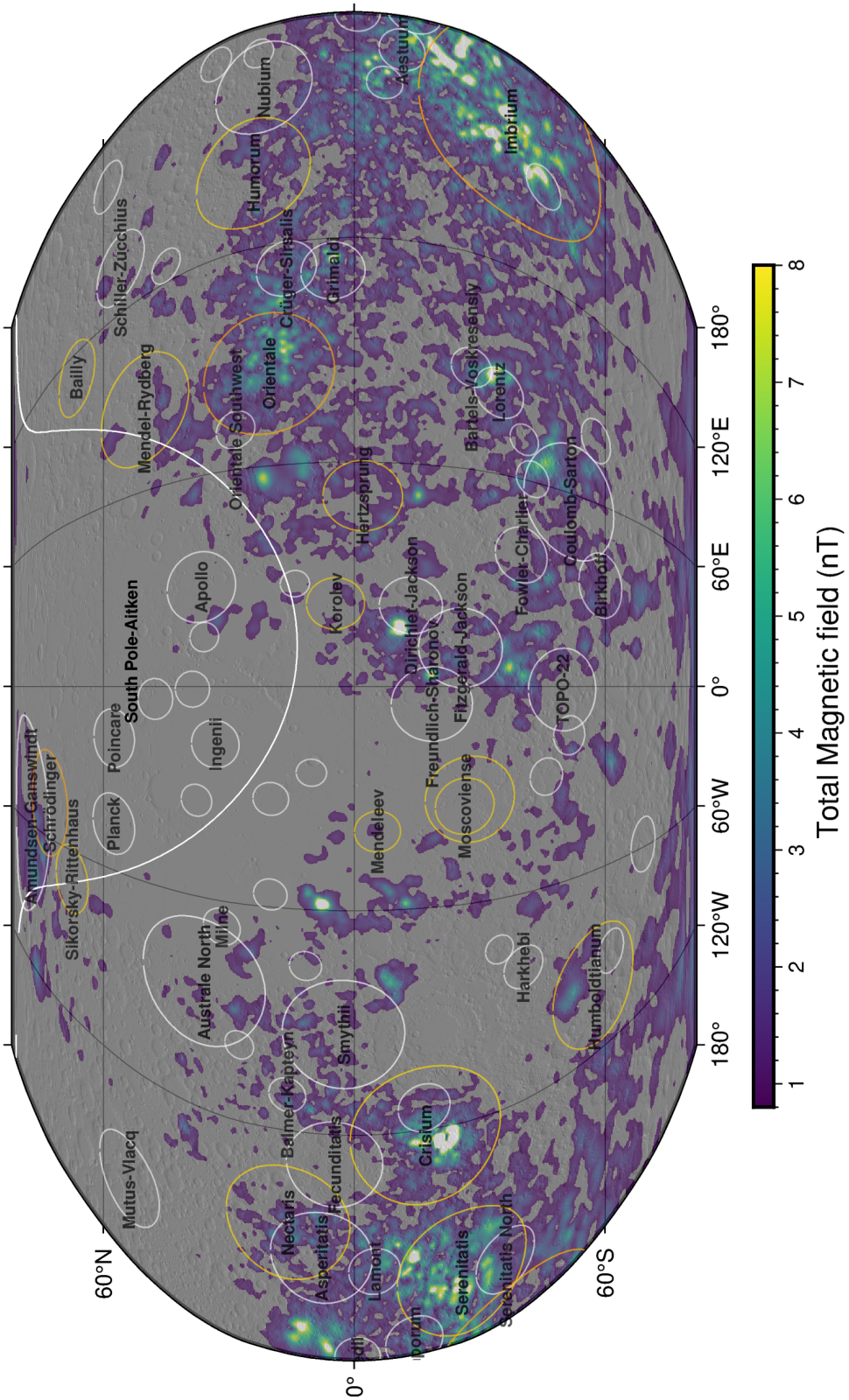

Figure 7.3: Global map of the antipodes of large impact craters and impact basins above 200 km diameter (crater data from Neumann et al., 2015) compared to the Tsunakawa magnetic map at 30 km altitude. Different colors for the craters correspond to the different lunar eras: in white are the Pre Nectarian-aged basins, in yellow are the Nectarian-aged basins and in gold are the Imbrian-aged basins. The magnetic moments of the dipoles are not represented by a unique scale, but a regional one, different anomaly from anomaly: in general, the lighter the color, the stronger the magnetic moment, thus the magnetization.

case for Smythii, Moscoviense, Australe North, Humboldtianum and Schrödinger craters for example. The vast South Pole-Aitken antipodal region, roughly corresponding to the Procellarum KREEP Terrane (PKT), is notably non-magnetized. This observation has led scientists to hypothesize that the thermal conditions within the PKT area (high geothermal flux and concentration of heat-producing elements) are likely unfavorable for the formation or preservation of magnetic anomalies (Grimm, 2012; J. Zhang et al., 2023). Others instead propose that the thin mare basalt layer that characterizes the PKT area doesn't preclude the possibility of magnetic anomalies to form, but could demagnetize the anomalies if the subsurface magmatism penetrated near the anomaly source (Hood et al., 2013).

It's important to understand that large impacts can potentially magnetize the antipodal surface via thermoremanent magnetization (TRM) or shock or pressure remanent magnetization (SRM/PRM). The former requires antipodal heating above the Curie temperature (favored by large impacts, through molten or shock-heated material that accumulates), ferromagnetic minerals (type and abundance are critical factors) and a steady magnetic field. SRM or PRM necessitates the focusing of shock waves that can generate high-pressure conditions in the crust (shock either coming from the impact or from ejecta striking the surface), ferromagnetic material below the Curie temperature and an ambient magnetic field that can be also transiently generated by the impact. While Wakita et al. (2021) and Tikoo et al. (2015) argue that pressure remanent magnetization (PRM) is unlikely to occur during ejecta deposition, due to insufficient pressure, shock waves from the impact can still propagate to the antipodal area, although weakened by energy losses over distance. These processes collectively contribute to the potential for antipodal magnetization in the aftermath of large impacts.

The age of the impacts appears to be another determining factor for the observation of magnetic anomalies of antipodal origin: Figure 7.3 also provides for the classification of craters into Pre-Nectarian, Nectarian, and Imbrian events, highlighting a notable trend: antipodes of Pre-Nectarian impacts rarely exhibit significant magnetization, whereas nearly all identified cases of Imbrian and Nectarian impacts show clear evidence of magnetized material at their antipodal regions. An explanation to the few exceptions to Nectarian-aged craters that do not present magnetized material can be found between their presence within the anomalous PKT area and the superposition by maria that may have demagnetized the areas. Two such exceptions, the Korolev, and Hertzsprung craters, are thought to be cases of demagnetization (Yang & Wieczorek, 2024). Following this reasoning, the impact events may have erased the pre-existing magnetization of the crust, and the lack of subsequent re-magnetization could be attributed to the low iron content of either the impactor or the target area. If antipodal magnetization primarily results from ejecta deposition, this iron deficiency could also explain the absence of detectable magnetic anomalies at the antipodes. This age correlation raises intriguing questions about the events that transpired between the Pre-Nectarian and Nectarian eras. Specifically, what processes led the Pre-Nectarian basins to exhibit little to no evidence of magnetization? Is this due to later geological activity erasing the original magnetization, or did fundamentally different conditions exist during the Pre-Nectarian period?

The regions associated with the analyzed magnetic anomalies will now be further investigated. The first area of focus is the Reiner Gamma, Rimae Sirsalis, and Hartwig area, as shown in Figure 7.4. Notably, this region stands out due to the absence of antipodal correlations with major impact basins in its vicinity. The closest large antipode is found to the north-west of Hartwig, just north of the Orientale crater, and is related to the Smythii crater, an old pre-Nectarian (Whitford-Stark, 1980) impact. Given that the effects of ancient impacts would have had to survive the impact gardening era, alongside local magnetization and demagnetization processes and the poorly understood overlay effects, it is unlikely that the very old Smythii impact event contributed to the formation of the three anomalies. The antipode of Moscoviense, located to the south-east, dates back to the Nectarian age (D. E. Wilhelms et al., 1987) but lies approximately 800 km away from Reiner Gamma, making a direct connection harder to explain, while the antipodes of the smaller Pasteur, Fermi and Mendeleev craters are likely too small to have contributed significantly to the magnetization of the area. Moreover, when examining the near-side anomalies east of the Imbrium crater (not showed here), only a weak correlation with a number of antipodes of older pre-Nectarian basins is observed. This leads to the conclusion that an antipodal origin of magnetization is unlikely for this extensive near-side region. Alternatively, if such an origin did occur, it was likely heavily altered and reshaped by subsequent events.

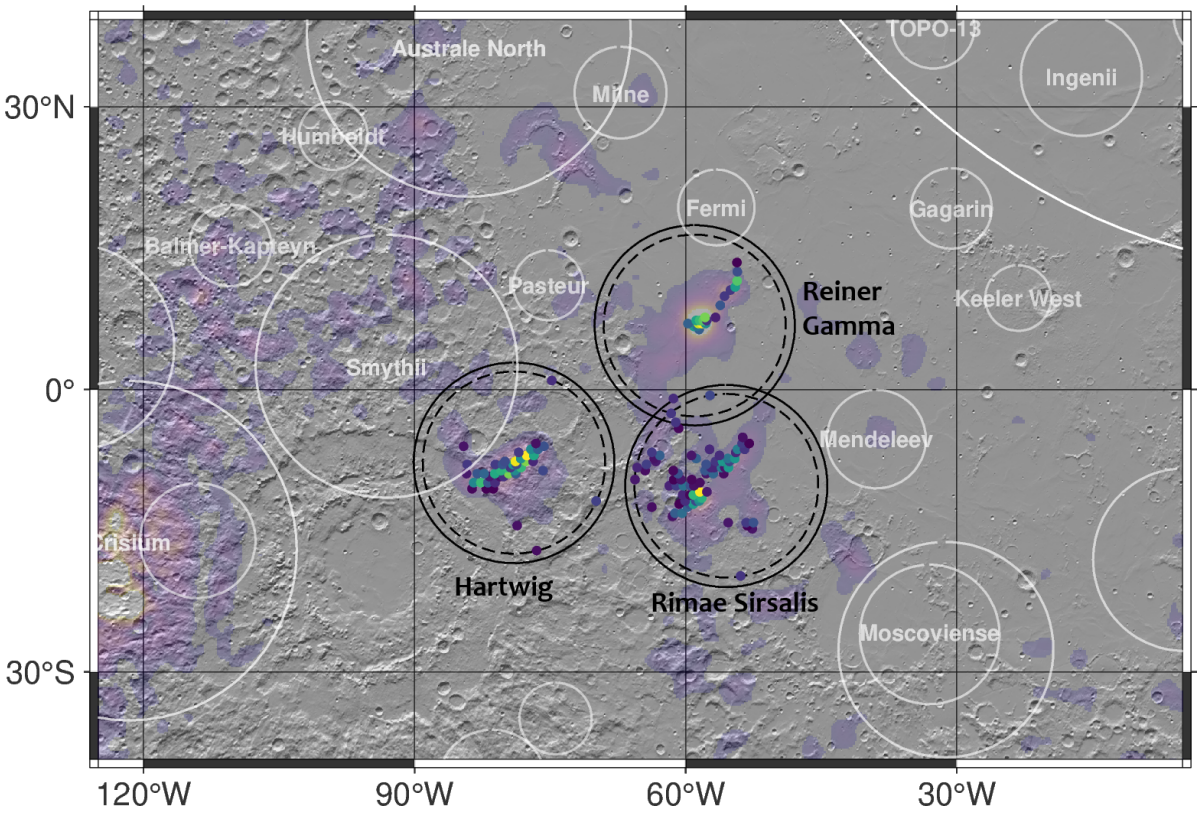

Figure 7.4: Zoom of the global antipodal map (Figure 7.3) in the area south-west of the Imbrium impact, encompassing the Reiner Gamma, Rimae Sirsalis and Hartwig anomalies. White circles represent the antipodes of major lunar craters. The magnetic moments of the dipoles are not represented by a unique scale, but a regional one, different anomaly from anomaly: in general, the lighter the color, the stronger the magnetic moment, thus the magnetization.

One isolated area which is instead well-correlated with major antipodal areas is the North Pole, where the Sylvester anomaly is located. This anomaly coincides with the largest collection of magnetic dipoles (see Figure 7.5), a smaller anomaly is observed around 45° more to the west, while a wake of more weakly magnetized material can be seen at lower latitudes. The region with the strongest magnetization aligns closely with the antipodal area of the (unconfirmed) Amundsen-Ganswindt crater and, with a slight offset, also corresponds to the antipode of the Schrödinger crater. The former is a proposed (D. Wilhelms et al., 1979) pre-Nectarian basin which is partially superposed by the latter, a more recent late-Nectarian / early Imbrian impact event. The correlation of the magnetized material with Schrödinger's antipode is supported by Hood et al. (2022) and the slight offset can be explained by imperfections of the antipodal magnetization process. On the other hand, if the correlation with the antipodal area of the older Amundsen-Ganswindt basin was found to be true, this would prompt for a reconsideration of the role of the more ancient impact events on the magnetization of the lunar crust and for the analysis of the conditions that led a few pre-Nectarian basins to show antipodal magnetization.

In contrast, the South Pole anomalies (see Figure 6.5-z) show no correlation with the antipodes of large basins, which can primarily be attributed to the absence of major craters at the North Pole. No origin has been proposed yet for this group of weak anomalies, but some hypotheses are here proposed:

1. the sources are magnetized ejecta from the nearby Schrödinger (or, with less likelihood, the Amundsen-Ganswindt crater) crater, thus suggesting a northeast to southwest direction for the impactor. Such impactor direction would contrast the geologic evidence of the shape of the continuous ejecta curtain and the rilles direction and positioning, which instead suggest an oblique strike from the south;

2. the sources are magnetized ejecta from the massive and ancient SPA impact event. Wieczorek et al. (2012) previously hypothesized that the SPA oblique impactor delivered iron-rich material to the surface just north of the impact, contributing to the creation of the complex and extensive far side anomalies. However, the possibility of ejecta being deposited, even though to a much lesser extent, near the southern rim - where the South Pole anomalies are found - has not been considered and is plausible;
3. sources are magnetized ejecta from a massive young basin that were deposited outside the expected location due to collisions among the ejecta themselves during the impact event;

Moreover, when analyzing the organization of surface magnetization using Parker's method — closely resembling that of the magnetic field at 30 km altitude — an east-west alignment emerges (see Figure 6.5-z). However, this orientation cannot be directly linked to any specific process or nearby geological formation.

An area that is known to be well correlated with antipodes is the complex far side. Although the local distribution of magnetization may be unreliable due to the challenges the method faces when analyzing such complex magnetic areas, the intensities of the magnetic moments correlate well with the maximum radial magnetic fields observed. For instance, the Gerasimovich anomaly, which is strongly correlated with the Crisium antipode, has a maximum magnetic moment of 26.5 Am^2, twice that of any other anomaly investigated. The next strongest anomalies are also found on the far side, specifically the SPA/Vertregt Van de Graaff and SPA/Walker anomalies (see output table in figure 6.6), linked to the Imbrium antipodal area. This suggests strong surface magnetization and likely distinct formation processes compared to those related to the magnetization of ejecta. For the Marginis-King region and the few isolated boreal anomalies found north of SPA, Figure 7.6 confirms the correspondence between the antipode of the young (Imbrian-aged) and large Orientale basin and the strongest section of the Marginis-King anomaly group. Other than this, the Moscoviense anomaly is located near the antipodes of the large Humorum and Nubium impact basins. Of these, the former is thought to be of Nectarian age, suggesting a closer connection with the anomaly compared to the Nubium basin, classified as Pre-Nectarian in age (data from the US geological survey).

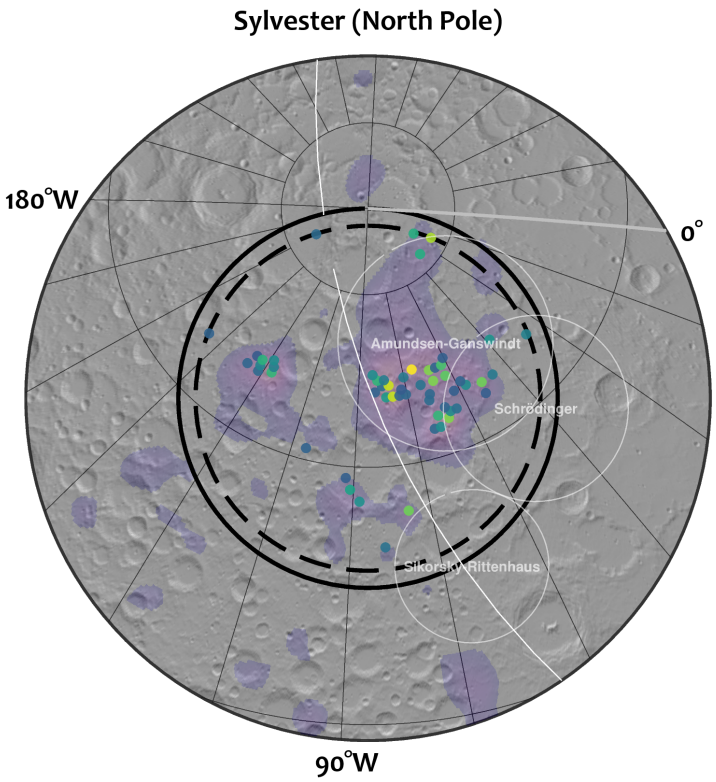

Figure 7.5: Zoom of the global antipodal map (Figure 7.3) in the North Pole area, showing the Sylvester anomaly and some smaller, unidentified anomalies. White circles represent the antipodes of major lunar craters. The magnetic moments of the dipoles are not represented by a unique scale, but a regional one, different anomaly from anomaly: in general, the lighter the color, the stronger the magnetic moment, thus the magnetization.

Interestingly, the strongest dipoles for the Moscoviense magnetic anomaly are also found within the main rim of the large Moscoviense crater, suggesting that the anomaly is intrinsic to the basin itself (Hood, Oliveira, et al., 2021). The surface magnetization relative to the Mendel-Rydberg crater (and anomaly) also shows a similar behavior. The origin of the crater-melt magnetization is thus gener-

ally attributed to thermoremanent magnetization and the presence of a long-standing magnetic field, supporting the hypothesis of a core dynamo. While shock remanent magnetization could also be a concurrent mechanism, it would likely be overshadowed by the dominant effects of the thermal process. Such a "cooling of central melt under a stable magnetic field" scenario provides another example of how impacts may contribute to the formation of magnetic anomalies, one that is not a focus for this project, but that has been for a number of investigations in recent years (e.g., Hood, 2011, Oliveira et al., 2017a, Hood, Oliveira, et al., 2021). It is important thus to note how surface magnetization results support the theory that sees central magnetization of impact melt as a mechanism for magnetization.

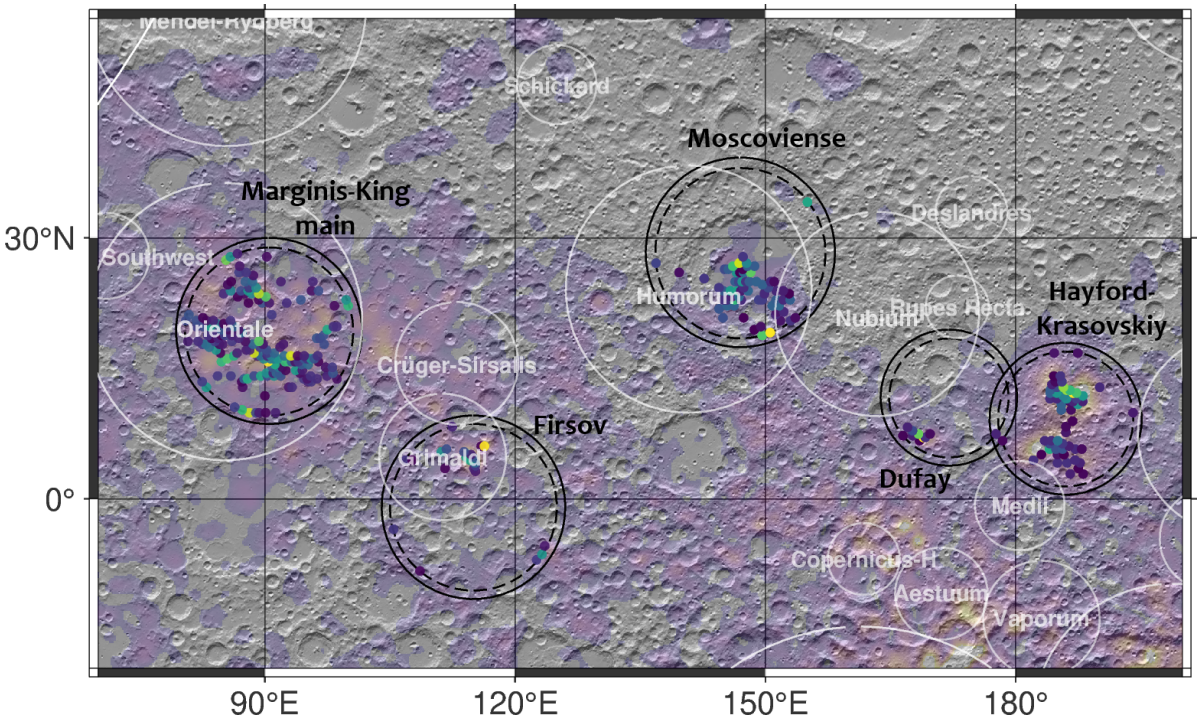

Figure 7.6: Zoom of the global antipodal map (Figure 7.3) in the boreal far side, showing the Marginis-King anomalies and the northern tip of the SPA anomalies. White circles represent the antipodes of major lunar craters. The magnetic moments of the dipoles are not represented by a unique scale, but a regional one, different anomaly from anomaly: in general, the lighter the color, the stronger the magnetic moment, thus the magnetization.

7.2. Are lunar albedo anomalies (swirls) delineating magnetized material?

Lunar swirls are distinct albedo anomalies of uncertain origin, representing a unique feature on the lunar surface. While nearly all lunar swirls are linked to magnetic anomalies, the reverse is not always observed (see Figure 7.7 and refer to Chapter 2 for further information). In this section, we explore the spatial relationship between these albedo anomalies and the surface distribution of magnetized material, focusing on the anomalies outlined in Figure 7.7.

7.2.1. The Reiner Gamma swirl case

The correlation between the prominent Reiner Gamma swirl and the surface magnetized material appears immediately peculiar. Three distinct regions compose the swirl formation: (a) the central structure, found approximately between 58°W-60°W in longitude and 6°N-8°N in latitude; (b) the north-east tail-like extension, a prominent elongated albedo feature; and (c) a group of smaller swirl formations situated to the southwest of the central structure. Concerning the intensity of the total magnetic field, the central region is associated with a magnetic anomaly measuring approximately 20 nT at an altitude

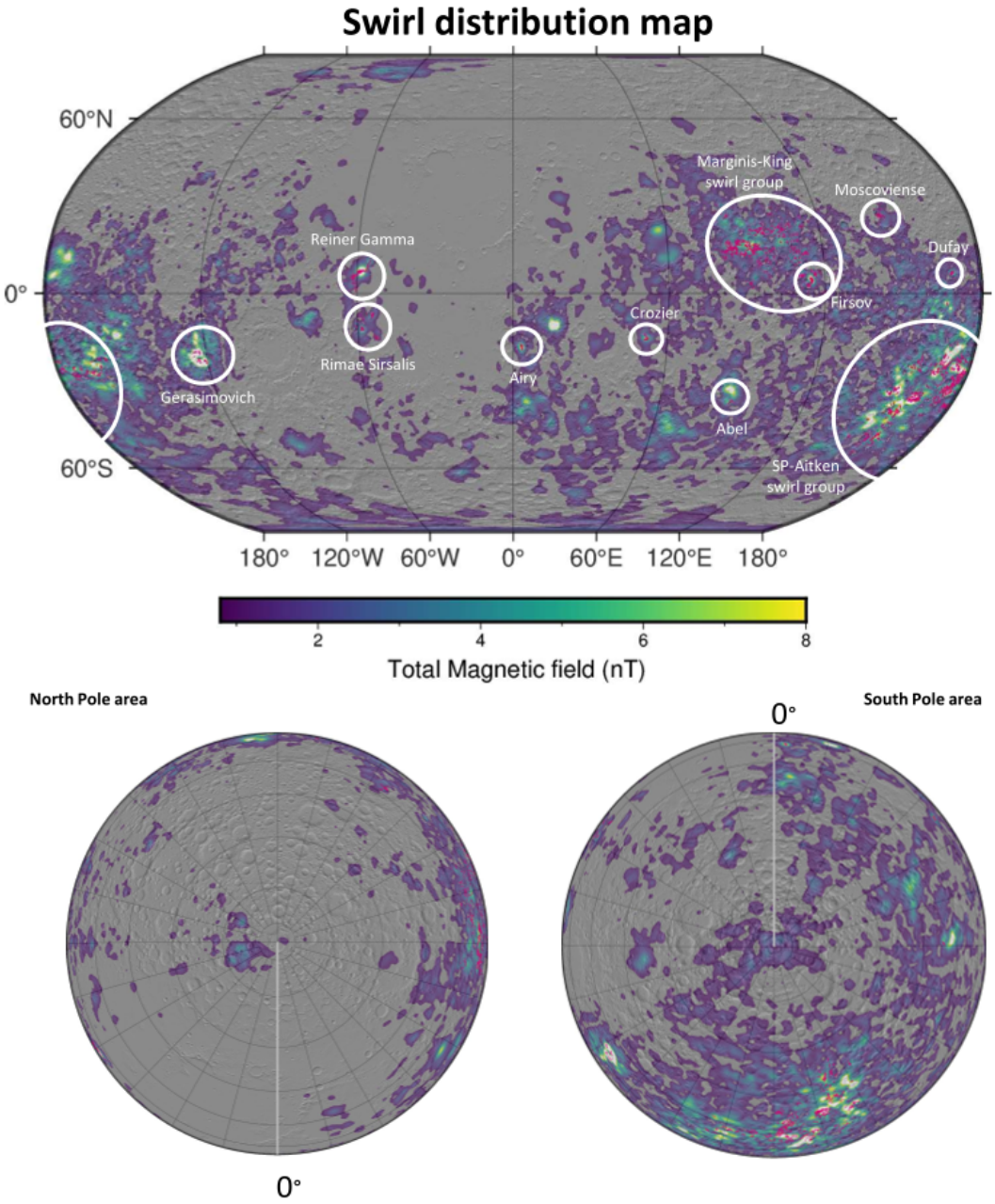

Figure 7.7: Global map showing the position of the lunar swirls (in fuchsia) from Denevi et al., 2016 and the total magnetic field map at 30 km altitude (the range is cut between 0.8 and 8 nT for plotting purposes) from Tsunakawa et al., 2015, with an underlying relief map. Circled in white are the main lunar swirls, with nomenclature referring to literature or generated ad-hoc when missing by looking at nearby geological features (e.g., Firsov, Dufay))

of 30 km, while the tail corresponds to a weaker anomaly of around 7 nT (Tsunakawa et al., 2015). The southwest cluster of smaller swirls exhibits only faint magnetic field signals. Looking at figure 7.8 above, the surface dipoles follow closely the sinuous structure, overlapping with it for most of its central body and north-eastern tail. The highly magnetized dipoles extend beyond the elongated segment and end deeper within the Marius Hill volcanic complex. Such over-extension feature is observed also for inversions with different circle sizes and various circle centerings (performed in the sensitivity analysis), thus it is less likely to be an artifact of the inversion method. One possible explanation is that this area represents a section of the swirl that has undergone optical maturation and is therefore no longer detectable, but still corresponds with magnetized material to some extent. Alternatively, iron abundance is thought to play a role in the presence or absence of a swirl. Variations in iron concentration, such

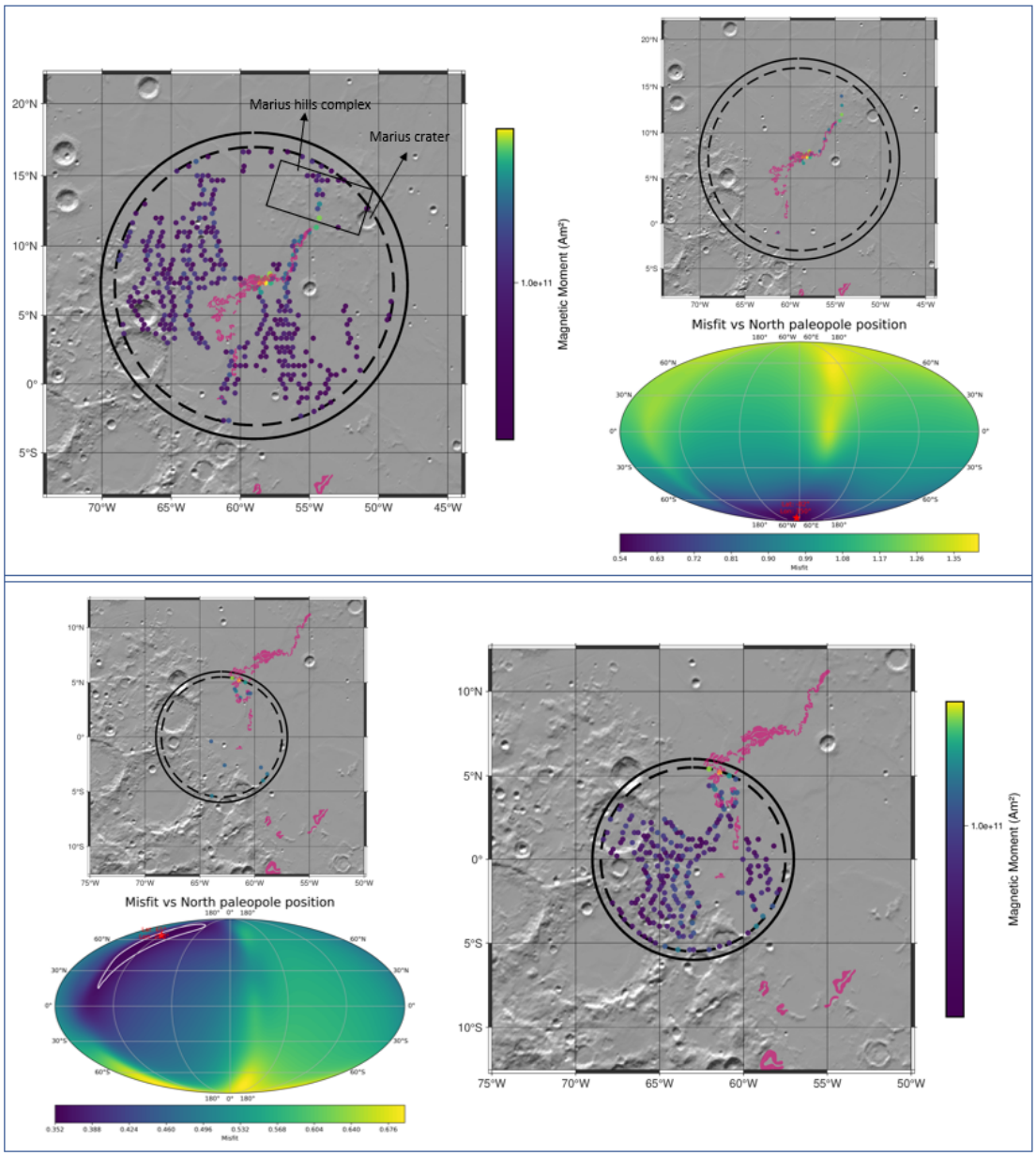

Figure 7.8: Surface distribution of non-zero dipoles above $10^{10} Am^2$ in the large map and above 30% of m_{max} in the smaller map, together with the North paleopole position vs. misfit map. On the top, Reiner Gamma is centered at 7°N and 59°W, on the bottom, the centering is shifted to 0°N and 63°W.

as a localized pocket of low iron, could introduce heterogeneity in the region, potentially disrupting the formation of a swirl with uniform characteristics (D. J. Lawrence et al., 2002). This compositional variability may have interfered with the development of a well-defined swirl in this area.

No retained dipoles are found instead for the south-eastern part of the central body and in the cluster of mini swirls in the south. In particular, no dipoles result from the inversion, and a “hole” of magnetized material is observed, a problematic product of the assumption of unidirectional magnetization. This issue is mitigated by shifting the center of the observation and dipole areas towards south-east, as in figure 7.8-below: with a different area being fed to the inversion and excluding the stronger anomalies in the northeast portion, the output results in an improved distribution of dipoles for the southern area. Notably, dipoles are now identified in regions where gaps previously existed, leading to an enhanced overall correlation between the swirl pattern and the magnetized dipoles. Moreover, looking at the two

best-fit positions of the north paleopole, these differ significantly and are nearly antipodal, despite the proximity of the areas investigated. The problem of this output is that strong dipoles are found on the edge of the circle: this does not represent an ideal inversion area. Another possible explanation for the low correlation between magnetized material and swirl contours in the southern region lies in the weaker intensity of the southern swirls. The magnetic moments in this area are relatively faint, as seen in the large-scale map. Using a lower threshold than the current 30% m_{max} might reveal additional correlations that are currently overlooked. Such threshold would not respect the empirical findings from Oliveira et al. (2024).

This case is a promising example of how the correlation between swirl formations and strong magnetic dipoles derived from Parker's method can significantly improve when combining and patching together results from different positions of the observation areas.

7.2.2. Correlating magnetization with swirls delineations for isolated anomalies

Isolated anomalies presenting swirls are prevalently found in the near-side of the Moon: it's the case of Reiner Gamma, Rimae Sirsalis, Airy, Crozier and Abel. Some are located in the far side, such as Dufay and Moscoviense and some others can be partially isolated from the large and complex anomaly structures (e.g., Firsov). All the analyzed anomalies associated with swirls show a clear spatial correlation between the magnetized material and the respective albedo anomaly delineation, ranging from very strong alignments to slightly less pronounced but still notable overlaps (see outputs in the Results chapter and in the Appendix). Rimae Sirsalis area is composed of 5 swirl formations, three major and two minor, and the retained strongest dipoles match with 4 out of the 5 features (Figure A.9-c). The Airy, Crozier, and Dufay anomalies exhibit isolated swirl structures that align precisely with the locations of the output surface magnetization (Figures A.9-d, 6.4-g and A.11-m respectively). The case of Abel (Figure A.10-i) is intriguing: while the swirl lies near the magnetic anomaly, it is situated outside its main body. The strongest dipoles align closely with the magnetic anomaly, yet only a single dipole — or a few, depending on the resolution of the dipole areas — is located in the immediate vicinity of the swirl. For the case of Moscoviense (Figure A.11-l), the surface magnetization is slightly shifted from the swirl structure, overlapping just partially. Results for Firsov (Figure A.11-k) align with the general good correlation trend but, being placed at the periphery of a complex magnetic and high-density swirl area, bears some struggles encountered when analyzing more complicated areas with the Parker's method.

The strong correlation between surface magnetized material and swirls is compelling. The fact that almost every swirl corresponds to a magnetized area, even though the reverse is not always true, strongly suggests that the existence of swirls must be closely linked to the presence of magnetic anomalies. This isn't a new idea, but never before the spatial distribution and intensity of surface magnetized material has been retrieved to verify it. These results, therefore, further solidify the connection between swirls and magnetic anomalies.

In order to further analyze the degree of correlation and possibly uncover an even tighter relationship between the swirl contours and the magnetized material, enhanced resolution would greatly help. The resolution of the magnetometers on-board of Lunar Prospector and Kaguya was of about 30 km (or 1°) as limited by the orbit-track separation, and have been slightly enhanced when converting the data to spherical harmonics. Although it is possible to significantly enhance the spatial resolution of the spherical distribution of surface dipoles to better explore the correlation between magnetized material and smaller swirls, this effort is largely constrained by the insufficient original resolution. Figure 7.9 illustrates the issue clearly. It also demonstrates how increasing the dipole density (combined with the effects of implementing a smaller angular radius) worsen edge effects: this happens as the strongest magnetic moments are shared among an increasing number of dipoles in the inversion, becoming smaller in amplitude when taken singularly for each dipole. What doesn't change instead are the anomalies found between the observation and dipole areas, which progressively become more dominant in the output as dipole density increases. Future space missions aim to enhance the current spatial resolution of lunar magnetic data. Notably, the Lunar Vertex mission will deploy a lander and rover to obtain high-resolution, localized magnetic measurements for the Reiner Gamma region. However, a comprehensive global mapping of the Moon's magnetic field is not a priority in the near future

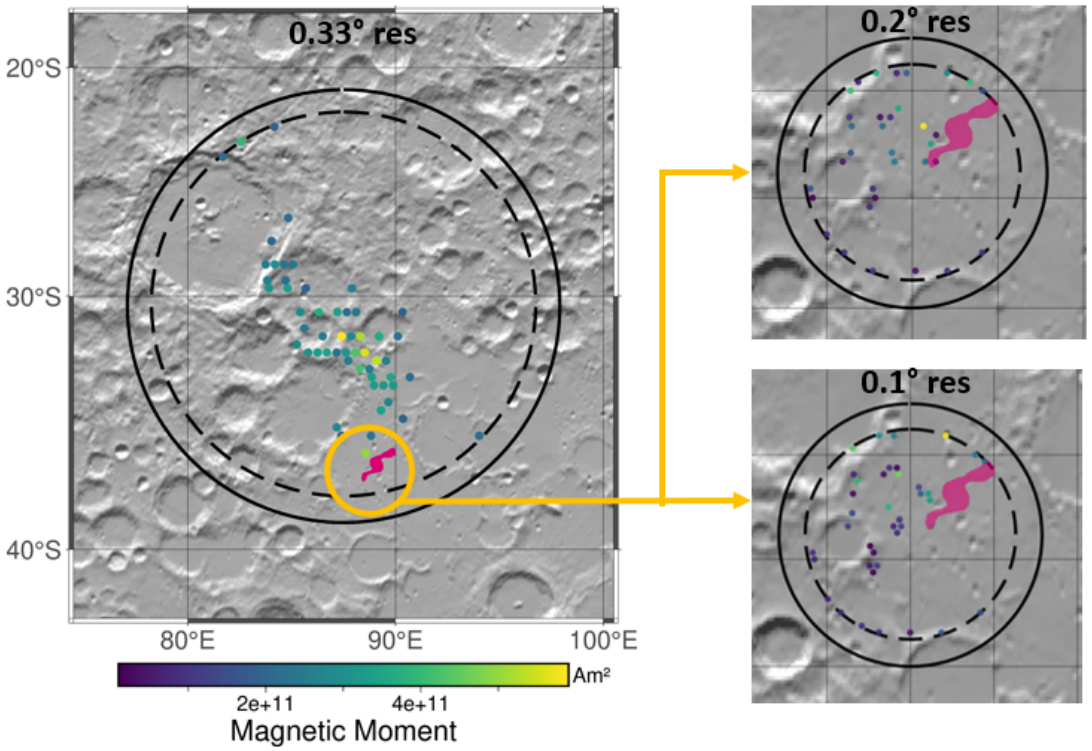

Figure 7.9: Strongest dipoles map for the Abel magnetic anomaly, with focus on increasing the resolution of the surface dipoles for the swirl area to 0.2° and 0.1°.

and will likely take several more years to be pursued.

7.2.3. Correlation with large and complex anomalies

When using the Parker's inversion method to analyze the large and magnetically complex swirl areas of Marginis-King and South Pole Aitken and their neighboring areas in the lunar far side, the correlation observed is rather poor. This is not to be considered a bad outcome and was expected for the following reasons:

- The analysed anomalies are not isolated, thus the inversion algorithm inevitably outputs a poorer best-fit compared to the better suited cases over most of the Lunar near-side. In particular, for a number of areas, edge effects contributed to producing a rather bad fit. Edge effects are also the reason a systematic analysis of the Moon using the Parker inversion method (by dividing the globe into equal areas) is not a good idea;
- The fundamental assumption of Parker's method — that magnetization is unidirectional — is less likely to hold in these magnetically complex and spatially extensive regions. Treating the entire magnetic group as the result of a single event would require modeling with computationally demanding circular source distributions and unidirectional dipoles over an area too large for this approach to be realistic. Since the region must instead be analyzed in smaller patches, the Parker inversion method becomes less suitable for this type of analysis.

The results for the large far side areas, as seen in figure A.18 and A.19 in the appendix, suggest the need for alternative analytical approaches for such regions.

7.2.4. Swirl formation and its connection to magnetic anomalies

Understanding how swirls form and evolve is key to unraveling the origin of lunar magnetic anomalies. Identifying the most plausible swirl formation mechanism could provide valuable insights, though it re-

mains a complex challenge given the data uncovered through the Parker inversion method. However, certain considerations can be made. Over the past decades, two primary hypotheses have been proposed to explain the formation of swirls. The first, known as the cometary model, suggests a relatively recent origin, attributing swirls to the impacts of cometary bodies (Schultz & Srnka, 1980). The second, referred to as the solar wind standoff model (Hood & Schubert, 1980), proposes that magnetic anomalies shield the surface from space weathering, creating the albedo features over time and pointing to a much older origin. Additionally, more unconventional ideas, such as the magnetic or electrostatic sorting of fine grains, have also been suggested (Garrick-Bethell et al., 2011).

A number of key characteristics of the swirl needs to be borne to mind when discussing about their possible origin, such as the apparent disregard of the topographic and geologic variations underneath, the similar spectral signal compared to very young craters, ejecta, and rays (of Copernican age), attributed to the sharing of a lesser degree of space weathering, and the spatial correlation with areas of higher iron and titanium density (compared to the lunar average). The plausibility of the two main hypothesis is now reflected upon, considering also the outcomes of the discussion on the ejecta/antipodal origin of magnetic anomalies.

The idea of the cometary model arose when it was noticed how the area beneath the lunar Apollo modules became smooth and bright due to the scouring effect of the engine exhaust. Comets, similarly, carry a “gas” in the form of a coma, which, upon impact, could potentially scour away loose soil from the surface, creating bright albedo anomalies. The relatively recent nature of the proposed cometary impacts is crucial to explain the lower degree of space weathering observed within the swirls. For this model, the swirls are actually immature: if the swirls were older, they would likely have already darkened. This model also helps account for the fact that swirls are only found in certain near side anomalies: cometary impacts are less frequent than asteroid impacts, so the issue of why only some anomalies exhibit swirls is mitigated. However, the statistically significant radial alignment of several swirl-related anomalies with the Imbrium basin (Hood, Torres, et al., 2021) challenges this idea, suggesting an older, non-cometary origin for many of the near-side anomalies. Further complications arise when considering the far side, which is rich in complex swirls and is likely the result of large impacts, most of which are of Imbrian and Nectarian age and not associated with cometary impacts. In this model, magnetic anomalies and swirls are believed to share a common origin. Magnetic anomalies are hypothesized to result from the magnetization of hot impact material, which is influenced by a transient magnetic field. This field may be generated either by the compression of the comet’s magnetic field or by charge separation between plasma and ejecta. Oran et al. (2020), while primarily simulating the creation and/or amplification of magnetic fields due to solar wind compression following large impacts fails to find transient fields anywhere near the required intensity and observes the strongest magnetizations above the surface. These findings weaken the hypothesis that magnetic fields result from solar wind compression. However, charge separation remains a viable alternative. Although this formation model seeks to explain the origin of both swirls and magnetic anomalies by linking them to a single cometary process, it struggles to account for the evident connections of magnetic anomalies to older impacts and fails to explain why swirls appear to be unique to the Moon. Mercury experiences a much higher rate of cometary impacts than the Moon, yet no distinct swirl-like features have been observed on the small rocky planet. Moreover, the higher iron and titanium density that is linked to most swirl areas isn’t considered.

The solar wind standoff model, also known as the shielding model, proposes instead that pre-existing crustal magnetic anomalies deflect the solar wind, reducing the rate of space weathering and contributing to swirl formation. This theory attributes the origin of swirls to the influence of these magnetic anomalies and their demonstrated ability to generate mini-magnetospheres (Wieser et al., 2010), which deflect solar wind protons and preserve the terrain in an immature state. According to this model, swirls are not inherently young but merely appear less weathered due to reduced solar wind exposure. The origin of magnetic anomalies is not critical to understanding this theory. Magnetic anomalies presenting swirls are found to correlate with areas with iron abundance higher than average (Denevi et al., 2016). Cases of anomalies located in low-iron regions, such as Dufay and Gerasimovich, suggest that while iron favors the formation and preservation of swirls over time, it is not a necessary condition. Since higher iron abundance is typically observed in regions with maria, it is almost certain that this crustal

iron comes from basaltic eruptions that covered the lowlands, rather than being delivered by asteroids. What can be proposed, however, is that anomalies in areas with low surficial iron like Dufay and Gerasimovich may be sourced by iron from deeper ejecta deposits. Moreover, if low-iron regions are found to hinder the formation of swirls, this would challenge the comet formation model, as it suggests that swirl creation might be dependent on local composition, contradicting the idea that the cometary impact process should be independent of such factors. Considering that the shielding efficiency is believed to be between 10 and 50% (Lue et al., 2011), how are swirls still immature to these days? On the base of the similar optical properties shared between swirls and Erasthotenian/Copernican impact craters, Hood et al. (2001) proposed that, occasionally, young impacts could “refresh” the surface by addition of new material as ejecta. This hypothesis is strengthened by the variation of swirl color properties with distance from such young craters. The strong connection observed between surface magnetized material and magnetic anomalies in this project suggests that, at some point, all magnetic anomalies may have been associated with swirls. Given the stochastic nature of this surface “refreshing” mechanism, this could also explain why not all magnetic anomalies currently exhibit swirls, as many may have darkened over time. An alternative explanation could involve a combination of factors, including variable impactor compositions, landing area characteristics (iron-rich or iron-poor), and shielding efficiency. If this model proves to be correct, it would suggest that the solar wind is the dominant driver of space weathering, as micrometeorite sputtering continues unaffected despite the presence of magnetic anomalies.

Promisingly, important data will soon be obtained to finally better comprehend the genesis of swirls. The Lunar Vertex mission is set to launch by (not sooner than) the end of 2025 and will target (also implementing a rover) the still mysterious Reiner Gamma swirl, with the goal of quantifying space weathering in situ and understanding the roles of solar wind exposure versus micrometeoroid sputtering (Blewett et al., 2021).

7.3. The complex origin of magnetic anomalies

This section aims to consolidate the insights gained on the origin of anomalies in the investigated areas into a unified perspective, while also considering other hypotheses from previous works. After that, the core-dynamo vs. transient field debate is tackled through the perspective of this work’s results.

7.3.1. Proposed origins for lunar magnetic anomalies and alternative hypotheses

A clear outcome of the correlative analysis between surface magnetization and impact events is that magnetic anomalies likely result from not just one impact-related process, but at least three: the magnetization of ballistic ejecta from very large impacts, the magnetization at the impact antipode for massive and relatively young (Imbrian and Nectarian-aged) events, and the cooling and subsequent magnetization of impact melt within a crater in a steady magnetic field. Let’s now provide an overall assessment of the origins of the areas of interest investigated in this project, beginning with the near-side anomalies. From this work’s results, the trio of strong anomalies south-west of Imbrium displays an ejecta origin likely from the Imbrium impact event (such finding is supported by the statistical and correlative studies of Halekas et al., 2001, Hood et al., 2001, Hood, Torres, et al., 2021) but could be possibly tied to the Serenitatis crater as well, while no antipodes of major impacts correlate with the area. Some alternative hypotheses have also been proposed: Reiner Gamma has been proposed to originate from a linear dike of magmatic origin due to its proximity to the Marius Hills volcanic rise (Oliveira et al., 2017b; Spudis et al., 2013), or from a melt layer or floor deposits formed by an oblique-impact crater (Garrick Bethell & Kelley, 2019). Rimae Sirsalis association to a magmatic dike swarm has been advanced by (Srnka et al., 1979), while Hartwig remains an anomaly without a widely accepted alternative explanation to date.
Magnetic anomalies east/southeast of Imbrium, between 0 and 100°E (anomalies d to i in Figure 6.3),

are here proposed to share a common ejecta origin from the Imbrium event, while the observed correlation with basin antipodes is weak and mostly tied to ancient Pre-Nectarian events. Connections of some anomalies to the Serenitatis, Nectaris and Crisium events, all found in the area, cannot be excluded. Anomalies in this area haven't been extensively studied in the literature, except for Descartes, located near an Apollo landing site. This strong anomaly has been proposed to be linked to the nearby furrowed and hilly terrain of the Descartes Mountains, which is generally believed to originate from ejecta from Imbrium, Nectaris, or both (Hood et al., 2013; Richmond et al., 2003). Laboratory studies confirm an Imbrium-like age and the presence of KREEP-bearing rocks in Apollo samples from the area, further supporting the ejecta origin theory (Norman et al., 2010).

Notably, only five of the nine analyzed anomalies suggested here to be associated with ejecta deposits (Reiner Gamma, Rimae Sirsalis, Airy, Crozier, and Abel) are correlated with swirls. This could be seen as challenging the idea that all these anomalies share an Imbrian ejecta origin. While this may still be the case, and perhaps multiple impact events contributed, several explanations can be proposed for the variation in swirl correlation despite a common origin. Aside from Airy, the other swirl-associated anomalies show a strong correlation with regions of above-average surface iron abundance, which may have influenced the formation or preservation of albedo anomalies. Additionally, ejecta with varying compositions may have been produced, with some fostering swirl formation while others did not. Finally, according to the impact "refreshing" theory, it is possible that all anomalies were originally accompanied by swirls, but only some received additional material from more recent, smaller impacts, helping preserve their immature status.

The anomalies found north/northwest of the Orientale crater are here suggested to be linked to the Orientale impact event, despite displaying a less pronounced alignment with the crater center compared to the Imbrium case. The alternative hypothesis of an antipodal origin appears less convincing, given the weak correlation with the Smythii, Australe, and Fecunditatis impact basins, all of Pre-Nectarian age. The only clear antipodal match is found in the Tsander-Mach anomaly, the westernmost anomaly associated with Orientale, which aligns well with the Nectarian-aged Nectaris antipode. Given its distance from Orientale and its weak radial correlation with the basin, this anomaly may have instead originated from the Nectaris event, contrary to the findings of Hood, Torres, et al. (2021), which attributed it to ejecta from the Orientale event. Given the magnetically weak nature of these anomalies, few studies investigated into this area and no other origins have been proposed. For both the Imbrium and Orientale basins, a statistically significant correlation has been observed between the orientation of the magnetization and the proposed ejecta sources (Hood, Torres, et al., 2021). This further supports the ejecta origin hypothesis presented in this study.

The lunar far side is evidently linked to an antipodal origin, likely through the deposition of distal ejecta from impact basins or shock/pressure magnetization from the impact event or ejecta re-deposition. Antipodal areas also exhibit furrowed and hilly terrain, geological features of probable tectonic origin found also at the antipodes of other young, large impact basins on Mars and Mercury (e.g., for the Caloris Basin), further reinforcing the antipodal genesis of anomalies related to large Imbrian/Nectarian-aged impact basins. Most of the existing hypotheses agree with an antipodal origin, deeming highly unlikely that cometary impacts would coincidentally occur in regions that are all antipodal to four similarly aged basins and magnetize basin-related terranes (Richmond et al., 2005). The Marginis-King group correlates with the Orientale antipode, the SPA group with the Imbrium antipode and the Gerasimovich anomaly with the Crisium antipode. The SPA anomalies have also been hypothesized to originate from ejecta produced by the massive and ancient SPA oblique impactor (Wieczorek et al., 2012). This theory represents the only instance of a Pre-Nectarian event being proposed as the source of currently observed magnetization, but the sheer size of the event sets it apart from other Pre-Nectarian impacts. Alternatively, the large magnetic area has been interpreted to be a subsurface swarm of magnetized dikes associated with magma ascent and the emplacement of mare basalts on the South Pole-Aitken basin floor (Purucker et al., 2012), a theory that disregards impacts. The North Pole Sylvester anomaly is also here proposed to bear an antipodal origin from the medium-sized and Imbrian-aged Schrödinger crater, with the more closely spatially correlated Amundsen-Ganswindt crater likely being too old to be considered the primary cause/source of the current distribution of the magnetic anomalies (similar conclusion from Hood et al., 2013). The origin of the South Pole anomalies remains particularly enigmatic,

but the complete absence of antipodal areas of any impact basin nearby leads to an ejecta origin being the most probable hypothesis, either from the Schrödinger crater, from the old SPA impactor or from rerouting of ejecta from other major impact events which perhaps collided mid-air.

Other anomalies strike for their existence within major impact craters and are particularly interesting because, due to their probable thermoremanent magnetization, are considered evidence of the existence of a core dynamo. An example is represented by the Mendel-Rydberg and Moscoviense magnetic anomalies, both showing magnetized material located within the inner depression of the relative crater, where the impact melt is thought to have accumulated. Other cases analyzed in Oliveira et al. (2017a) using Parker's inversion method include the magnetic anomalies found at the center of the Humboldtianum, Serenitatis, Nectaris, and Crisium craters, leading to the conclusion that the magnetizations observed likely result from iron-rich projectile materials incorporated into the melt sheet. Most Pre-Nectarian basins, as well as the few Imbrian basins, do not exhibit central magnetization. A possible explanation for older craters is that successive impacts and the deposition of foreign material may have contributed to the weakening, covering, or complete erasure of any preexisting magnetization. For younger basins, key factors that need further investigation to understand the absence of central anomalies include the overall impact energy (influenced by speed, angle, and size of the impactor), the composition of the impactor, and the location of the strike (for instance, Imbrium is situated within the thermally anomalous PKT region). Similarly, for the discussion of antipodal magnetization, the explanation remains a big question mark.

Overall, within this impacts-dominated origin scenario, it can be hypothesized that for most of the lunar magnetic anomalies, one or more of these three processes, combined with younger altering effects, could explain their formation.

7.3.2. Insights from this work on the core-dynamo vs. transient fields debate

How does a putative core-dynamo fit within an impact-driven origin for the magnetic anomalies? Firstly, core-dynamo and impacts most likely both contributed in the generation of magnetic anomalies: this is because, unless magnetic field were transiently created during impacts, both shock remanent magnetization and thermal remanent magnetization necessitate of a steady magnetic field for the rocks to acquire magnetization (a transient magnetic field could be enough for SRM but not for TRM).

In regard to the plausibility of the existence of such a transient magnetic field, let's consider one of the largest single anomalies analyzed, the Gerasimovich anomaly. Transient field generated from plasma amplification would likely present field lines that rapidly change with time and are turbulent in nature, as we can expect that the interaction of the impact plasma cloud with the IMF happens in a short timescale, similarly to plasma time-related properties inside the magnetosphere. A preferred magnetization direction would not exist in such conditions: what is found instead is a rather consistent magnetization direction for the source. This suggests that the anomaly needed quite some time to form, pointing to the existence of a steady magnetic field, core-dynamo generated. Moreover, recent findings by Oran et al. (2020) indicate that transient magnetic fields generated by IMF compression do not reach the necessary intensities to account for the observed magnetic anomalies. The strongest transient field is instead found above the surface, but are still too weak.

A recent study (Narrett et al., 2024) explored and found plausible an intriguing concept: impact-generated plasma amplification of a past weak ($\sim$1 μT) core dynamo-generated magnetic field. This mechanism would better align with the low field intensities predicted by core dynamo models and casts doubt on paleointensity estimates, which have been questioned over the years due to the techniques and methods used during the Apollo era. Further research is needed to explore this emerging theory, and paleointensity estimates based on new samples returned by the Chang'E mission, as well as future missions, will be crucial in either confirming or challenging the Apollo-era estimates.

8

Conclusions

The origin of the weak and heterogeneously magnetized lunar crustal field has been a subject of debate for over 50 years. While some experts provide good evidence for a long-lived core dynamo extending well beyond the Moon's early history, others argue for an entirely external origin, suggesting that impacts generated transient magnetic fields are capable of permanently magnetizing the crust. Despite the importance attributed to external bodies in both theories — either as drivers for the anomaly formation in the first, or as the sole contributors to the current state of the magnetic field in the second — the role of impacts and the extent of their influence remain unclear. To gain a deeper understanding of lunar magnetism, it is essential to better constrain the sources of magnetization in terms of spatial distribution, direction, and intensity. However, studying magnetic anomalies is challenging due to the absence of apparent correlations with geological or geophysical structures, which are typically critical for conventional methods and techniques. Utilizing recent orbital magnetic field data, this project investigates a novel application of the well-established Parker inversion method (Parker, 1991), to constrain the spatial distribution of magnetized material on the lunar surface.

My results strongly indicate a complex origin for the magnetic anomalies, yet highly influenced by impacts. After analyzing 26 magnetic anomalies, those with similar origins were identified and grouped based on both their location and shared characteristics. A correlative analysis between the output magnetized surface dipoles and the radial alignment with two of the Moon's largest and youngest basins, Imbrium and Orientale, reveals that most of the strongest nearside anomalies are well aligned with the centers of these craters. This suggests an ejecta origin for most nearside anomalies and hints at a possible direction of the impactor from NW to SE for Imbrium and from SW to NE for Orientale. A number of complex magnetized areas in the lunar far side and in the north pole correlate well with the antipodal areas of the largest impact basins in the Moon from the Imbrian and Nectarian period, specifically for Imbrium, Orientale, Serenitatis, Crisium, Nectaris, and Schrödinger. They likely represent examples of antipodal magnetization from highly energetic impacts that magnetized the crust opposite to the impact through shock waves, ejecta deposition and an ionized impact melt cloud. Anomalies associated with large - though not the youngest - craters, occasionally exhibit magnetic signatures within their rims, supporting the hypothesis that magnetization originated from the cooling of impact-generated melt. Three primary mechanisms are thus proposed for the origin of the magnetic anomalies: from magnetization of impact ejecta, from magnetization at the impact antipode through the concentration of shock waves and/or distal ejecta and/or plasma clouds, and from magnetization of central impact melt within craters. It is here proposed that the origin of all lunar anomalies can be explained by one of - or a combination of - these three mechanisms.

From the correlative study between lunar swirls and surface magnetization, I find that, in most cases, surface dipoles align closely with the delineations of swirls. The strongest correlations occur for com-

pact and isolated anomalies, whereas the larger and more complex swirl regions on the far side show a weaker correspondence. This suggests that (considering the best-case inversions) swirls precisely trace magnetized regions: nearly every albedo anomaly corresponds to a magnetic anomaly, though the reverse is not always true. However, the large and complex swirl areas on the far side are not suitable targets for the Parker inversion method. Since most observed magnetic anomalies are proposed to be linked to Imbrian- and Nectarian-aged impacts, this challenges the cometary origin hypothesis for swirls (and magnetic anomalies) and instead supports the shielding hypothesis, in which a locally generated mini-magnetosphere protects the surface from space weathering, preventing maturation and darkening. It is possible that most or all magnetic anomalies once had swirls associated to them and that their currently observed absence in certain locations could be attributed to the stochastic nature of surface 'refreshing' from very young impacts, which allowed for the preservation of some swirls and the maturation of others. If true, this theory would prove how solar wind produces the most dominant maturation effects compared to micrometeoroid sputtering, which continues undisturbed everywhere.

The most straightforward explanation for the magnetization process is that it occurred during impact in the presence of a stable core-dynamo field. The thermoremanent magnetization mechanism, which drives both ejecta and central impact melt magnetization, requires in fact a steady ambient magnetic field. Furthermore, the idea of a purely transient impact-generated field seems less likely, given the relatively consistent magnetization directions resulting from the analysis of some large anomalies. This consistency suggests that the anomalies took time to form, implying the presence of a sustained magnetic field.

Future studies could help determine which of the three processes — ejecta, antipodal effects, or central impact melt — plays the most dominant role in lunar magnetization. This could be achieved through simulations and analyses of impactor properties such as size, velocity, inclination, and composition, as well as ejecta distribution and its effects at the antipodes. Notably, simulations of distal ejecta deposition on the Moon remain scarce and warrant further exploration. Additionally, gaining a deeper understanding of how recent impacts and geological processes have reshaped the crustal magnetic landscape, particularly through simulations, could provide further evidence supporting this work's main conclusions. Advancing studies on thermal and shock magnetization and demagnetization within the lunar environment would be especially valuable in this regard. More reliable paleomagnetic analyses of a broader range of lunar samples from upcoming missions could help determine whether current paleointensity estimates are justified or overly criticized. Furthermore, higher-resolution magnetic data from future missions would improve correlative studies with swirls, offering further insights into their formation and evolution. In regard to advancements of the Parker's inversion method, it should be possible to mathematically transition from the surface distribution of dipoles (and magnetization) back to a volumetric distribution (the volume would be the crust), which would give information of the (best-fit) depth of the magnetic sources. In addition, the method, as it stands, can be applied to other planetary bodies for which magnetic field measurements exist at various altitudes, in order to constrain their geological and magnetic evolution and evaluate comparisons with the Moon's case. Mars, in particular, exhibits remanent magnetization and shares similar patterns of potential magnetization processes with the Moon, making it a strong candidate for analysis using the Parker inversion method.

To conclude, Whitaker (1969) captured the essence of lunar magnetism's lingering mysteries while discussing Lunar Orbiter and Apollo 8 images of the swirls at Mare Ingenii and Marginis: "Clearly, more work needs to be done before any firm conclusions can be drawn." This statement remains just as relevant today, driving future exploration and discovery.

References

Acuña, M. H., Connerney, J. E. P., F., N., Ness, Lin, R. P., Mitchell, D., Carlson, C. W., McFadden, J., Anderson, K. A., Rème, H., Mazelle, C., Vignes, D., Wasilewski, P., & Cloutier, P. (1999). Global distribution of crustal magnetization discovered by the mars global surveyor mag/er experiment. *Science*, *284*(5415), 790–793. https://doi.org/10.1126/science.284.5415.790

Ampère, A. (1825). *Mémoire sur la théorie mathématique des phénomènes électrodynamiques : Uniquement déduite de l'expérience, dans lequel se trouvent réunis les mémoires que m. ampère a communiqués à l'académie royale des sciences, dans les séances des 4 et 26 décembre 1820, 10 juni 1822, 22 décembre 1823, 12 septembre 1825, et 21 novembre 1825*. Verlag nicht ermittelbar.

Arkani-Hamed, J., & Boutin, D. (2014). Analysis of isolated magnetic anomalies and magnetic signatures of impact craters: Evidence for a core dynamo in the early history of the moon. *Icarus*, *237*, 262–277. https://doi.org/10.1016/j.icarus.2014.04.046

Bamford, R. A., Alves, E. P., Cruz, F., Kellett, B. J., Fonseca, R. A., Silva, L. O., Trines, R. M. G. M., Halekas, J. S., Kramer, G., Harnett, E., Cairns, R. A., & Bingham, R. (2016). 3d pic simulations of collisionless shocks at lunar magnetic anomalies and their role in forming lunar swilrss. *The Astrophysical Journal*, *830*(2), 146. https://doi.org/10.3847/0004-637x/830/2/146

Binder, A. B. (1998). Lunar prospector: Overview. *Science*, *281*(5382), 1475–1476. https://doi.org/10.1126/science.281.5382.1475

Blewett, D., Halekas, J., Ho, G., Greenhagen, B., Anderson, B., Vines, S., Regoli, L., Jahn, J., Kollmann, P., Denevi, B., Meyer, H., Klima, R., Cahill, J., Hood, L., Tikoo-Schantz, S., Zou, X., Wieczorek, M., Lemelin, M., & Fatemi, S. (2021, December). *Exploring a lunar magnetic anomaly: The lunar vertex PRISM mission*.

Brown, L. W. (1975). Saturn radio emission near 1 mhz. *The Astrophysical Journal*, *198*, L89. https://doi.org/10.1086/181819

Burke, B. F., & Franklin, K. L. (1955). Observations of a variable radio source associated with the planet jupiter. *Journal of Geophysical Research*, *60*(2), 213–217. https://doi.org/10.1029/jz060i002p00213

Butler, R. F. (1992). *Magnetic domains to geologic terranes*. Blackwell.

Carley, R. A., Whaler, K. A., Purucker, M. E., & Halekas, J. S. (2012). Magnetization of the lunar crust. *Journal of Geophysical Research: Planets*, *117*(E8). https://doi.org/10.1029/2011je003944

Cisowski, S. M., Collinson, D. W., Runcorn, S. K., Stephenson, A., & Fuller, M. (1983). A review of lunar paleointensity data and implications for the origin of lunar magnetism. *Journal of Geophysical Research: Solid Earth*, *88*(S02). https://doi.org/10.1029/jb088is02p0a691

Cournède, C., Gattacceca, J., & Rochette, P. (2012). Magnetic study of large apollo samples: Possible evidence for an ancient centered dipolar field on the moon. *Earth and Planetary Science Letters*, *331–332*, 31–42. https://doi.org/10.1016/j.epsl.2012.03.004

Crawford, D. A. (2020). Simulations of magnetic fields produced by asteroid impact: Possible implications for planetary paleomagnetism. *International Journal of Impact Engineering*, *137*, 103464. https://doi.org/10.1016/j.ijimpeng.2019.103464

Denevi, B. W., Robinson, M. S., Boyd, A. K., Blewett, D. T., & Klima, R. L. (2016). The distribution and extent of lunar swirls. *Icarus*, *273*, 53–67. https://doi.org/10.1016/j.icarus.2016.01.017

Dolginov, S. S., Eroshenko, E. G., Zhuzgov, L., & Pushkov, N. (1966). Measurements of the magnetic field in the vicinity of the moon on the ams luna-10. *Dokl Acad Sci USSR*, (Earth Sci Sect 170:18-20).

Duba, A., & Ringwood, A. E. (1973). Electrical conductivity, internal temperatures and thermal evolution of the moon. *The Moon*, *7*(3–4), 356–376. https://doi.org/10.1007/bf00564640

Dwyer, C. A., Stevenson, D. J., & Nimmo, F. (2011). A long-lived lunar dynamo driven by continuous mechanical stirring. *Nature*, *479*(7372), 212–214. https://doi.org/10.1038/nature10564

Dyal, P., & Parkin, C. W. (1971). The apollo 12 magnetometer experiment: Internal lunar properties from transient and steady magnetic field measurements. *Lunar and Planetary Science Conference Proceedings*, *2*, 2391. https://ui.adsabs.harvard.edu/abs/1971LPSC....2.2391D

Elsasser, W. M. (1958). The earth as a dynamo. *Scientific American*, *198*(5), 44–48. https://doi.org/10.1038/scientificamerican0558-44

Evans, A. J., Zuber, M. T., Weiss, B. P., & Tikoo, S. M. (2014). A wet, heterogeneous lunar interior: Lower mantle and core dynamo evolution. *Journal of Geophysical Research: Planets*, *119*(5), 1061–1077. https://doi.org/10.1002/2013je004494

Fuller, M. (1974). Lunar magnetism. *Reviews of Geophysics*, *12*(1), 23–70. https://doi.org/10.1029/rg012i001p00023

Fuller, M., & Cisowski, S. M. (1987). Lunar paleomagnetism. In J. A. Jacobs (Ed.), *Geomagnetism* (pp. 307–455, Vol. 2). Academic Press.

Garcia, M. (2017). *60 years ago, the space age began* [Retrieved August 8, 2022]. Retrieved August 8, 2022, from https://www.nasa.gov/feature/60-years-ago-the-space-age-began

Garg, A. K. (2012, April). *Classical electromagnetism in a nutshell*. Princeton University Press.

Garrick Bethell, I., & Kelley, M. R. (2019). Reiner gamma: A magnetized elliptical disk on the moon. *Geophysical Research Letters*, *46*(10), 5065–5074. https://doi.org/10.1029/2019gl082427

Garrick-Bethell, I., Head, J. W., & Pieters, C. M. (2011). Spectral properties, magnetic fields, and dust transport at lunar swirls. *Icarus*, *212*(2), 480–492. https://doi.org/10.1016/j.icarus.2010.11.036

Garrick-Bethell, I., Weiss, B. P., Shuster, D. L., & Buz, J. (2009). Early lunar magnetism. *Science*, *323*(5912), 356–359. https://doi.org/10.1126/science.1166804

Garrick-Bethell, I., Weiss, B. P., Shuster, D. L., Tikoo, S. M., & Tremblay, M. M. (2017). Further evidence for early lunar magnetism from troctolite 76535. *Journal of Geophysical Research: Planets*, *122*(1), 76–93. https://doi.org/10.1002/2016je005154

Gattacceca, J., Boustie, M., Hood, L., Cuq-Lelandais, J. P., Fuller, M., Bezaeva, N. S., de Resseguier, T., & Berthe, L. (2010). Can the lunar crust be magnetized by shock: Experimental groundtruth. *Earth and Planetary Science Letters*, *299*(1–2), 42–53. https://doi.org/10.1016/j.epsl.2010.08.011

Green, J., Draper, D., Boardsen, S., & Dong, C. (2020). When the moon had a magnetosphere. *Science Advances*, *6*(42). https://doi.org/10.1126/sciadv.abc0865

Grimm, R. E. (2012). Thermal models of the lunar procellarum kreep terrane: Geophysical implications [Abstract 2313.pdf]. *43rd Lunar and Planetary Science Conference*.

Halekas, J. S., Bale, S. D., Mitchell, D. L., & Lin, R. P. (2005). Electrons and magnetic fields in the lunar plasma wake. *Journal of Geophysical Research: Space Physics*, *110*(A7). https://doi.org/10.1029/2004ja010991

Halekas, J. S., Lin, R. P., & Mitchell, D. L. (2003). Magnetic fields of lunar multi□ring impact basins. *Meteoritics & Planetary Science*, *38*(4), 565–578. https://doi.org/10.1111/j.1945-5100.2003.tb00027.x

Halekas, J. S., Mitchell, D. L., Lin, R. P., Frey, S., Hood, L. L., Acuña, M. H., & Binder, A. B. (2001). Mapping of crustal magnetic anomalies on the lunar near side by the lunar prospector electron reflectometer. *Journal of Geophysical Research: Planets*, *106*(E11), 27841–27852. https://doi.org/10.1029/2000je001380

Harnett, E. M., & Winglee, R. M. (2003). 2.5□d fluid simulations of the solar wind interacting with multiple dipoles on the surface of the moon. *Journal of Geophysical Research: Space Physics*, *108*(A2). https://doi.org/10.1029/2002ja009617

Hemingway, D. J., & Tikoo, S. M. (2018). Lunar swirl morphology constrains the geometry, magnetization, and origins of lunar magnetic anomalies. *Journal of Geophysical Research: Planets*, *123*(8), 2223–2241. https://doi.org/10.1029/2018je005604

Hood, L. L. (2011). Central magnetic anomalies of nectarian-aged lunar impact basins: Probable evidence for an early core dynamo. *Icarus*, *211*(2), 1109–1128. https://doi.org/10.1016/j.icarus.2010.08.012

Hood, L. L. (2014). Lunar magnetic anomalies. In *Encyclopedia of lunar science* (pp. 1–8). Springer International Publishing. https://doi.org/10.1007/978-3-319-05546-6_4-1

Hood, L. L., & Artemieva, N. A. (2008). Antipodal effects of lunar basin-forming impacts: Initial 3d simulations and comparisons with observations. *Icarus*, *193*(2), 485–502. https://doi.org/10.1016/j.icarus.2007.08.023

Hood, L. L., Bryant, I., & van der Leeuw, J. (2022). Lunar magnetic anomalies and polar ice. *Geophysical Research Letters*, *49*(22). https://doi.org/10.1029/2022gl100557

Hood, L. L., Oliveira, J. S., Andrews□Hanna, J., Wieczorek, M. A., & Stewart, S. T. (2021). Magnetic anomalies in five lunar impact basins: Implications for impactor trajectories and inverse modeling. *Journal of Geophysical Research: Planets*, *126*(2). https://doi.org/10.1029/2020je006668

Hood, L. L., Richmond, N. C., & Spudis, P. D. (2013). Origin of strong lunar magnetic anomalies: Further mapping and examinations of lroc imagery in regions antipodal to young large impact basins. *Journal of Geophysical Research: Planets*, *118*(6), 1265–1284. https://doi.org/10.1002/jgre.20078

Hood, L. L., & Schubert, G. (1980). Lunar magnetic anomalies and surface optical properties. *Science*, *208*(4439), 49–51. https://doi.org/10.1126/science.208.4439.49

Hood, L. L., Torres, C. B., Oliveira, J. S., Wieczorek, M. A., & Stewart, S. T. (2021). A new large□scale map of the lunar crustal magnetic field and its interpretation. *Journal of Geophysical Research: Planets*, *126*(2). https://doi.org/10.1029/2020je006667

Hood, L. L., & Vickery, A. (1984). Magnetic field amplification and generation in hypervelocity meteoroid impacts with application to lunar paleomagnetism. *J. Geophys. Res.*, *89*(S01), C211.

Hood, L. L., Zakharian, A., Halekas, J., Mitchell, D. L., Lin, R. P., Acuña, M. H., & Binder, A. B. (2001). Initial mapping and interpretation of lunar crustal magnetic anomalies using lunar prospector magnetometer data. *Journal of Geophysical Research: Planets*, *106*(E11), 27825–27839. https://doi.org/10.1029/2000je001366

Katanforoush, A., & Shahshahani, M. (2003). Distributing points on the sphere, i. *Experimental Mathematics*, *12*(2), 199–209. https://doi.org/10.1080/10586458.2003.10504492

Kato, M., Sasaki, S., & Takizawa, Y. (2010). The kaguya mission overview. *Space Science Reviews*, *154*(1–4), 3–19. https://doi.org/10.1007/s11214-010-9678-3

Kelley, M. R., & Garrick-Bethell, I. (2020). Gravity constraints on the age and formation of the moon's reiner gamma magnetic anomaly. *Icarus*, *338*, 113465. https://doi.org/10.1016/j.icarus.2019.113465

Kiefer, W. S. (n.d.). *Lunar orbiter: Impact basin geology* [Accessed: 2025-01-04]. https://www.lpi.usra.edu/lunar/missions/orbiter/lunar_orbiter/impact_basin/?utm_source=chatgpt.com

Konrad, W., & Spohn, T. (1997). Thermal history of the moon: Implications for an early core dynamo and post-accertional magmatism. *Advances in Space Research*, *19*(10), 1511–1521. https://doi.org/10.1016/s0273-1177(97)00364-5

Laneuville, M., Wieczorek, M., Breuer, D., Aubert, J., Morard, G., & Rückriemen, T. (2014). A long-lived lunar dynamo powered by core crystallization. *Earth and Planetary Science Letters*, *401*, 251–260. https://doi.org/10.1016/j.epsl.2014.05.057

Larmor, J. (1919). How could a rotating body such as the sun become a magnet? *Reports of the British Association*, *87*, 159–160.

Latham, G., Ewing, M., Dorman, J., Nakamura, Y., Press, F., Toksöz, N., Sutton, G., Duennebier, F., & Lammlein, D. (1973). Lunar structure and dynamics - results from the apollo passive seismic experiment. *The Moon*, *7*(3–4), 396–421. https://doi.org/10.1007/bf00564643

Lawrence, D. J., Feldman, W. C., Elphic, R. C., Little, R. C., Prettyman, T. H., Maurice, S., Lucey, P. G., & Binder, A. B. (2002). Iron abundances on the lunar surface as measured by the lunar prospector gamma□ray and neutron spectrometers. *Journal of Geophysical Research: Planets*, *107*(E12). https://doi.org/10.1029/2001je001530

Lawrence, K., Johnson, C., Tauxe, L., & Gee, J. (2008). Lunar paleointensity measurements: Implications for lunar magnetic evolution. *Physics of the Earth and Planetary Interiors*, *168*(1–2), 71–87. https://doi.org/10.1016/j.pepi.2008.05.007

Lawson, C. L., & Hanson, R. J. (1974). *Solving least squares problems*. Society for Industrial; Applied Mathematics. https://doi.org/10.1137/1.9781611971217

Le Bars, M., Cébron, D., & Le Gal, P. (2015). Flows driven by libration, precession, and tides. *Annual Review of Fluid Mechanics*, *47*(1), 163–193. https://doi.org/10.1146/annurev-fluid-010814-014556

Le Bars, M., Wieczorek, M. A., Karatekin, Ö., Cébron, D., & Laneuville, M. (2011). An impact-driven dynamo for the early moon. *Nature*, *479*(7372), 215–218. https://doi.org/10.1038/nature10565

Lin, R., Anderson, K., & Hood, L. (1988). Lunar surface magnetic field concentrations antipodal to young large impact basins. *Icarus*, *74*(3), 529–541. https://doi.org/10.1016/0019-1035(88)90119-4

Lue, C., Futaana, Y., Barabash, S., Wieser, M., Holmström, M., Bhardwaj, A., Dhanya, M. B., & Wurz, P. (2011). Strong influence of lunar crustal fields on the solar wind flow. *Geophysical Research Letters*, *38*(3). https://doi.org/10.1029/2010gl046215

Meyer, J., & Wisdom, J. (2011). Precession of the lunar core. *Icarus*, *211*(1), 921–924. https://doi.org/10.1016/j.icarus.2010.09.016

Mighani, S., Wang, H., Shuster, D. L., Borlina, C. S., Nichols, C. I. O., & Weiss, B. P. (2020). The end of the lunar dynamo. *Science Advances*, *6*(1). https://doi.org/10.1126/sciadv.aax0883

Morse, Z. R., Osinski, G. R., & Tornabene, L. L. (2018). New morphological mapping and interpretation of ejecta deposits from orientale basin on the moon. *Icarus*, *299*, 253–271. https://doi.org/10.1016/j.icarus.2017.08.010

Nakamura, Y., Latham, G., Lammlein, D., Ewing, M., Duennebier, F., & Dorman, J. (1974). Deep lunar interior inferred from recent seismic data. *Geophysical Research Letters*, *1*(3), 137–140. https://doi.org/10.1029/gl001i003p00137

Narrett, I. S., Oran, R., Chen, Y., Miljković, K., Toth, G., & Weiss, B. P. (2024). Lunar crustal magnetization from impact-generated plasma amplification of the lunar dynamo [Abstract #1515]. *Proceedings of the 55th Lunar and Planetary Science Conference (LPSC)*.

NASA NSSDC. (2020). *Chang'e 5 - spacecraft details* [Retrieved February 28, 2025]. https://web.archive.org/web/20201130150906/https://nssdc.gsfc.nasa.gov/nmc/spacecraft/display.action?id=CHANG-E-5

NASA NSSDC. (2024a). *Apollo 11 command and service module (csm)* [Retrieved February 27, 2025]. https://nssdc.gsfc.nasa.gov/nmc/spacecraft/display.action?id=1969-059A

NASA NSSDC. (2024b). *Chang'e 6 - spacecraft details* [Retrieved February 28, 2025]. https://nssdc.gsfc.nasa.gov/nmc/spacecraft/display.action?id=CHANG-E-6

NASA NSSDC. (2024c). *Explorer 35 - spacecraft details* [Retrieved February 27, 2025]. https://nssdc.gsfc.nasa.gov/nmc/spacecraft/display.action?id=1967-070A

NASA NSSDC. (2024d). *Luna 10 - details* [Retrieved February 27, 2025]. https://nssdc.gsfc.nasa.gov/nmc/spacecraft/display.action?id=1966-027A

NASA NSSDC. (2024e). *Luna 2 - trajectory details* [Retrieved February 27, 2025]. https://nssdc.gsfc.nasa.gov/nmc/spacecraft/displayTrajectory.action?id=1959-014A

Nayak, M., Hemingway, D., & Garrick-Bethell, I. (2017). Magnetization in the south pole-aitken basin: Implications for the lunar dynamo and true polar wander. *Icarus*, *286*, 153–192. https://doi.org/10.1016/j.icarus.2016.09.038

Ness, N. F., Behannon, K. W., Lepping, R. P., & Whang, Y. C. (1975). The magnetic field of mercury, 1. *Journal of Geophysical Research*, *80*(19), 2708–2716. https://doi.org/10.1029/ja080i019p02708

Neumann, G. A., Zuber, M. T., Wieczorek, M. A., Head, J. W., Baker, D. M. H., Solomon, S. C., Smith, D. E., Lemoine, F. G., Mazarico, E., Sabaka, T. J., Goossens, S. J., Melosh, H. J., Phillips, R. J., Asmar, S. W., Konopliv, A. S., Williams, J. G., Sori, M. M., Soderblom, J. M., Miljković, K., … Kiefer, W. S. (2015). Lunar impact basins revealed by gravity recovery and interior laboratory measurements. *Science Advances*, *1*(9). https://doi.org/10.1126/sciadv.1500852

Norman, M., Duncan, R., & Huard, J. (2010). Imbrium provenance for the apollo 16 descartes terrain: Argon ages and geochemistry of lunar breccias 67016 and 67455. *Geochimica et Cosmochimica Acta*, *74*(2), 763–783. https://doi.org/10.1016/j.gca.2009.10.024

Oliveira, J. S., Hood, L. L., & Langlais, B. (2019). Constraining the early history of mercury and its core dynamo by studying the crustal magnetic field. *Journal of Geophysical Research: Planets*, *124*(9), 2382–2396. https://doi.org/10.1029/2019je005938

Oliveira, J. S., Vervelidou, F., Wieczorek, M. A., & Díaz Michelena, M. (2024). Constraints on the spatial distribution of lunar crustal magnetic sources from orbital magnetic field data. *Journal of Geophysical Research: Planets*, *129*(2). https://doi.org/10.1029/2023je008125

Oliveira, J. S., & Wieczorek, M. A. (2017). Testing the axial dipole hypothesis for the moon by modeling the direction of crustal magnetization. *J. Geophys. Res. Planets*, *122*(2), 383–399.

Oliveira, J. S., Wieczorek, M. A., & Kletetschka, G. (2017a). Iron abundances in lunar impact basin melt sheets from orbital magnetic field data. *Journal of Geophysical Research: Planets*, *122*(12), 2429–2444. https://doi.org/10.1002/2017je005397

Oliveira, J. S., Wieczorek, M. A., & Kletetschka, G. (2017b). Iron abundances in lunar impact basin melt sheets from orbital magnetic field data. *Journal of Geophysical Research: Planets*, *122*(12), 2429–2444. https://doi.org/10.1002/2017je005397

Oran, R., Weiss, B. P., Shprits, Y., Miljković, K., & Tóth, G. (2020). Was the moon magnetized by impact plasmas? *Science Advances*, *6*(40). https://doi.org/10.1126/sciadv.abb1475

Parker, R. L. (1975). The theory of ideal bodies for gravity interpretation. *Geophysical Journal International*, *42*(2), 315–334. https://doi.org/10.1111/j.1365-246x.1975.tb05864.x

Parker, R. L. (1991). A theory of ideal bodies for seamount magnetism. *Journal of Geophysical Research: Solid Earth*, *96*(B10), 16101–16112. https://doi.org/10.1029/91jb01497

Pieters, C. M., Moriarty III, D. P., & Garrick-Bethell, I. (2014). Atypical regolith processes hold the key to enigmatic lunar swirls [Supported through NASA SSERVI.]. *45th Lunar and Planetary Science Conference*.

Purucker, M. E., Head, J. W., & Wilson, L. (2012). Magnetic signature of the lunar south Pole□Aitken basin: Character, origin, and age. *J. Geophys. Res.*, *117*(E5).

Qian, Y., Xiao, L., Head, J. W., van der Bogert, C. H., Hiesinger, H., & Wilson, L. (2021). Young lunar mare basalts in the chang'e-5 sample return region, northern oceanus procellarum. *Earth and Planetary Science Letters*, *555*, 116702. https://doi.org/10.1016/j.epsl.2020.116702

Ravat, D., Purucker, M. E., & Olsen, N. (2020). Lunar magnetic field models from lunar prospector and selene/kaguya along□track magnetic field gradients. *Journal of Geophysical Research: Planets*, *125*(7). https://doi.org/10.1029/2019je006187

Richmond, N. C., & Hood, L. L. (2008). A preliminary global map of the vector lunar crustal magnetic field based on lunar prospector magnetometer data. *Journal of Geophysical Research: Planets*, *113*(E2). https://doi.org/10.1029/2007je002933

Richmond, N. C., Hood, L. L., Halekas, J. S., Mitchell, D. L., Lin, R. P., Acuña, M., & Binder, A. B. (2003). Correlation of a strong lunar magnetic anomaly with a high□albedo region of the descartes mountains. *Geophysical Research Letters*, *30*(7). https://doi.org/10.1029/2003gl016938

Richmond, N. C., Hood, L. L., Mitchell, D. L., Lin, R. P., Acuña, M. H., & Binder, A. B. (2005). Correlations between magnetic anomalies and surface geology antipodal to lunar impact basins. *Journal of Geophysical Research: Planets*, *110*(E5). https://doi.org/10.1029/2005je002405

Righter, K., Go, B., Pando, K., Danielson, L., Ross, D., Rahman, Z., & Keller, L. (2017). Phase equilibria of a low s and c lunar core: Implications for an early lunar dynamo and physical state of the current core. *Earth and Planetary Science Letters*, *463*, 323–332. https://doi.org/10.1016/j.epsl.2017.02.003

Rochette, P., Gattacceca, J., Ivanov, A., Nazarov, M., & Bezaeva, N. (2010). Magnetic properties of lunar materials: Meteorites, luna and apollo returned samples. *Earth and Planetary Science Letters*, *292*(3–4), 383–391. https://doi.org/10.1016/j.epsl.2010.02.007

Runcorn, S. K. (1983). Lunar magnetism, polar displacements and primeval satellites in the earth–moon system. *Nature*, *304*(5927), 589–596. https://doi.org/10.1038/304589a0

Scheinberg, A. L., Soderlund, K. M., & Elkins-Tanton, L. T. (2018). A basal magma ocean dynamo to explain the early lunar magnetic field. *Earth and Planetary Science Letters*, *492*, 144–151. https://doi.org/10.1016/j.epsl.2018.04.015

Schultz, P. H., & Crawford, D. A. (2016). Origin and implications of non-radial imbrium sculpture on the moon. *Nature*, *535*(7612), 391–394. https://doi.org/10.1038/nature18278

Schultz, P. H., & Srnka, L. J. (1980). Cometary collisions on the moon and mercury. *Nature*, *284*(5751), 22–26. https://doi.org/10.1038/284022a0

Shea, E. K., Weiss, B. P., Cassata, W. S., Shuster, D. L., Tikoo, S. M., Gattacceca, J., Grove, T. L., & Fuller, M. D. (2012). A long-lived lunar core dynamo. *Science*, *335*(6067), 453–456. https://doi.org/10.1126/science.1215359

Siddiqi, A., & Office, U. S. N. H. P. (2018). *Beyond earth: A chronicle of deep space exploration, 1958-2016*. National Aeronautics; Space Administration, Office of Communications, NASA History Division. https://books.google.de/books?id=t0OlNUruyi8C

Sonett, C. P. (1982). Electromagnetic induction in the moon. *Reviews of Geophysics*, *20*(3), 411–455. https://doi.org/10.1029/rg020i003p00411

Sonett, C. P., Colburn, D. S., & Currie, R. G. (1967). The intrinsic magnetic field of the moon. *Journal of Geophysical Research*, *72*(21), 5503–5507. https://doi.org/10.1029/jz072i021p05503

Spohn, T. (2001). The longevity of lunar volcanism: Implications of thermal evolution calculations with 2d and 3d mantle convection models. *Icarus*, *149*(1), 54–65. https://doi.org/10.1006/icar.2000.6514

Spudis, P. D. (2012). *The moon's antipodal magnetism mystery* [Retrieved March 3, 2025]. https://www.smithsonianmag.com/air-space-magazine/the-moons-antipodal-magnetism-mystery-1050195/

Spudis, P. D., McGovern, P. J., & Kiefer, W. S. (2013). Large shield volcanoes on the moon. *Journal of Geophysical Research: Planets*, *118*(5), 1063–1081. https://doi.org/10.1002/jgre.20059

Srnka, L., Hoyt, J., Harvey, J., & McCoy, J. (1979). A study of the rima sirsalis lunar magnetic anomaly. *Physics of the Earth and Planetary Interiors*, *20*(2–4), 281–290. https://doi.org/10.1016/0031-9201(79)90051-7

Suavet, C., Weiss, B. P., Cassata, W. S., Shuster, D. L., Gattacceca, J., Chan, L., Garrick-Bethell, I., Head, J. W., Grove, T. L., & Fuller, M. D. (2013). Persistence and origin of the lunar core dynamo. *Proceedings of the National Academy of Sciences*, *110*(21), 8453–8458. https://doi.org/10.1073/pnas.1300341110

Takahashi, F., Tsunakawa, H., Shimizu, H., Shibuya, H., & Matsushima, M. (2014). Reorientation of the early lunar pole. *Nature Geoscience*, *7*(6), 409–412. https://doi.org/10.1038/ngeo2150

Tarduno, J. A., Cottrell, R. D., Lawrence, K., Bono, R. K., Huang, W., Johnson, C. L., Blackman, E. G., Smirnov, A. V., Nakajima, M., Neal, C. R., Zhou, T., Ibanez-Mejia, M., Oda, H., & Crummins, B. (2021). Absence of a long-lived lunar paleomagnetosphere. *Science Advances*, *7*(32). https://doi.org/10.1126/sciadv.abi7647

Tikoo, S. M., Weiss, B. P., Shuster, D. L., Suavet, C., Wang, H., & Grove, T. L. (2017). A two-billion-year history for the lunar dynamo. *Science Advances*, *3*(8). https://doi.org/10.1126/sciadv.1700207

Tikoo, S. M., Gattacceca, J., Swanson□Hysell, N. L., Weiss, B. P., Suavet, C., & Cournède, C. (2015). Preservation and detectability of shock□induced magnetization. *Journal of Geophysical Research: Planets*, *120*(9), 1461–1475. https://doi.org/10.1002/2015je004840

Tsunakawa, H., Takahashi, F., Shimizu, H., Shibuya, H., & Matsushima, M. (2015). Surface vector mapping of magnetic anomalies over the moon using kaguya and lunar prospector observations. *Journal of Geophysical Research: Planets*, *120*(6), 1160–1185. https://doi.org/10.1002/2014je004785

Urey, H. C., & Korff, S. A. (1952). The planets: Their origin and development. *Physics Today*, *5*(8), 12–12. https://doi.org/10.1063/1.3067687

US, M. S. C. (1971). Apollo lunar surface experiments package: Alsep training handout, apollo 16 crew briefing.

Vacquier, V. (1962). A machine method for computing the magnitude and direction of magnetization of a uniformly magnetized body from its shape and a magnetic survey. *Proc. Penedum Earth Magnetism Symposium*, 123.

Wakita, S., Johnson, B. C., Garrick-Bethell, I., Kelley, M. R., Maxwell, R. E., & Davison, T. M. (2021). Impactor material records the ancient lunar magnetic field in antipodal anomalies. *Nature Communications*, *12*(1). https://doi.org/10.1038/s41467-021-26860-1

Wang, H., Weiss, B. P., Bai, X., Downey, B. G., Wang, J., Wang, J., Suavet, C., Fu, R. R., & Zucolotto, M. E. (2017). Lifetime of the solar nebula constrained by meteorite paleomagnetism. *Science*, *355*(6325), 623–627. https://doi.org/10.1126/science.aaf5043

Weber, R. C., Lin, P., Garnero, E. J., Williams, Q., & Lognonné, P. (2011). Seismic detection of the lunar core. *Science*, *331*(6015), 309–312. https://doi.org/10.1126/science.1199375

Whitford-Stark, J. L. (1980). Lunar surface morphology and stratigraphy: A remote sensing synthesis [Available at: https://adsabs.harvard.edu/full/1980JBAA…90..312W]. *Journal of the British Astronomical Association*, *90*, 312.

Wieczorek, M. A. (2018). Strength, depth, and geometry of magnetic sources in the crust of the moon from localized power spectrum analysis. *Journal of Geophysical Research: Planets*, *123*(1), 291–316. https://doi.org/10.1002/2017je005418

Wieczorek, M. A., Weiss, B. P., Breuer, D., Cébron, D., Fuller, M., Garrick-Bethell, I., Gattacceca, J., Halekas, J. S., Hemingway, D. J., Hood, L. L., Laneuville, M., Nimmo, F., Oran, R., Purucker, M. E., Rückriemen, T., Soderlund, K. M., & Tikoo, S. M. (2023). Lunar magnetism. *Reviews in Mineralogy and Geochemistry*, *89*(1), 207–241. https://doi.org/10.2138/rmg.2023.89.05

Wieczorek, M. A., Weiss, B. P., & Stewart, S. T. (2012). An impactor origin for lunar magnetic anomalies. *Science*, *335*(6073), 1212–1215.

Wieser, M., Barabash, S., Futaana, Y., Holmström, M., Bhardwaj, A., Sridharan, R., Dhanya, M. B., Schaufelberger, A., Wurz, P., & Asamura, K. (2010). First observation of a mini□magnetosphere above a lunar magnetic anomaly using energetic neutral atoms. *Geophysical Research Letters*, *37*(5). https://doi.org/10.1029/2009gl041721

Wilhelms, D., Howard, K., & Wilshire, H. (1979). Geologic map of the south side of the moon.

Wilhelms, D. E., McCauley, J. F., & Trask, N. J. (1987). *The geologic history of the moon*. https://doi.org/10.3133/pp1348

Williams, J. G., Boggs, D. H., Yoder, C. F., Ratcliff, J. T., & Dickey, J. O. (2001). Lunar rotational dissipation in solid body and molten core. *Journal of Geophysical Research: Planets*, *106*(E11), 27933–27968. https://doi.org/10.1029/2000je001396

Williams, J. G., Konopliv, A. S., Boggs, D. H., Park, R. S., Yuan, D., Lemoine, F. G., Goossens, S., Mazarico, E., Nimmo, F., Weber, R. C., Asmar, S. W., Melosh, H. J., Neumann, G. A., Phillips, R. J., Smith, D. E., Solomon, S. C., Watkins, M. M., Wieczorek, M. A., Andrews-Hanna, J. C., … Zuber, M. T. (2014). Lunar interior properties from the grail mission: Lunar interior properties. *Journal of Geophysical Research: Planets*, *119*(7), 1546–1578. https://doi.org/10.1002/2013je004559

Williams, J. G., Turyshev, S. G., Boggs, D. H., & Ratcliff, J. T. (2006). Lunar laser ranging science: Gravitational physics and lunar interior and geodesy. *Advances in Space Research*, *37*(1), 67–71. https://doi.org/10.1016/j.asr.2005.05.013

Williams, Q. (2009). Bottom-up versus top-down solidification of the cores of small solar system bodies: Constraints on paradoxical cores. *Earth and Planetary Science Letters*, *284*(3–4), 564–569. https://doi.org/10.1016/j.epsl.2009.05.019

Yang, X., & Wieczorek, M. (2024). Magnetic signatures of lunar impact craters. *Icarus*, *415*, 116049. https://doi.org/10.1016/j.icarus.2024.116049

Zeigler, R. A., Mosie, A. B., Corrigan, C., Costello, L. J., Kent, J. J., Krysher, C. H., Watts, L. A., & McCubbin, F. M. (2019). The apollo sample collection: 50 years of solar system insight. *Elements*, *15*(4), 286–287. https://doi.org/10.2138/gselements.15.4.286

Zhang, J., Head, J., Liu, J., & Potter, R. (2023). Lunar procellarum kreep terrane (pkt) stratigraphy and structure with depth: Evidence for significantly decreased th concentrations and thermal evolution consequences. *Remote Sensing*, *15*(7), 1861. https://doi.org/10.3390/rs15071861

Zhang, N., Parmentier, E. M., & Liang, Y. (2013). A 3□d numerical study of the thermal evolution of the moon after cumulate mantle overturn: The importance of rheology and core solidification. *Journal of Geophysical Research: Planets*, *118*(9), 1789–1804. https://doi.org/10.1002/jgre.20121

A

Appendix

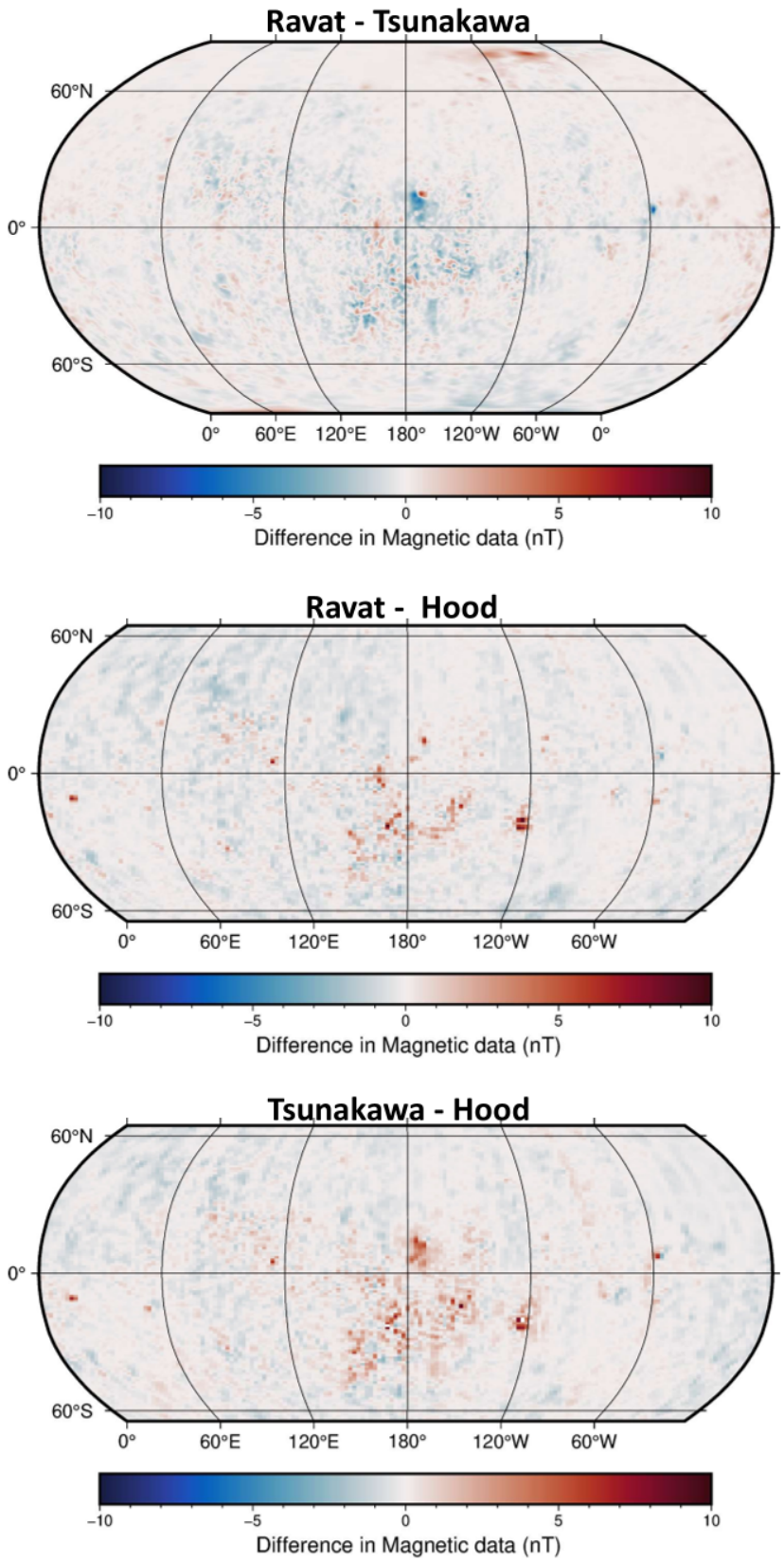

Figure A.1: Maps comparing the Tsunakawa, Ravat and Hood maps, showing the differences in total magnetic field intensities. From top to bottom, the Tsunakawa map is subtracted to the Ravat map, the Hood map is subtracted to the Ravat map, and the Hood map is subtracted to the Tsunakawa map.

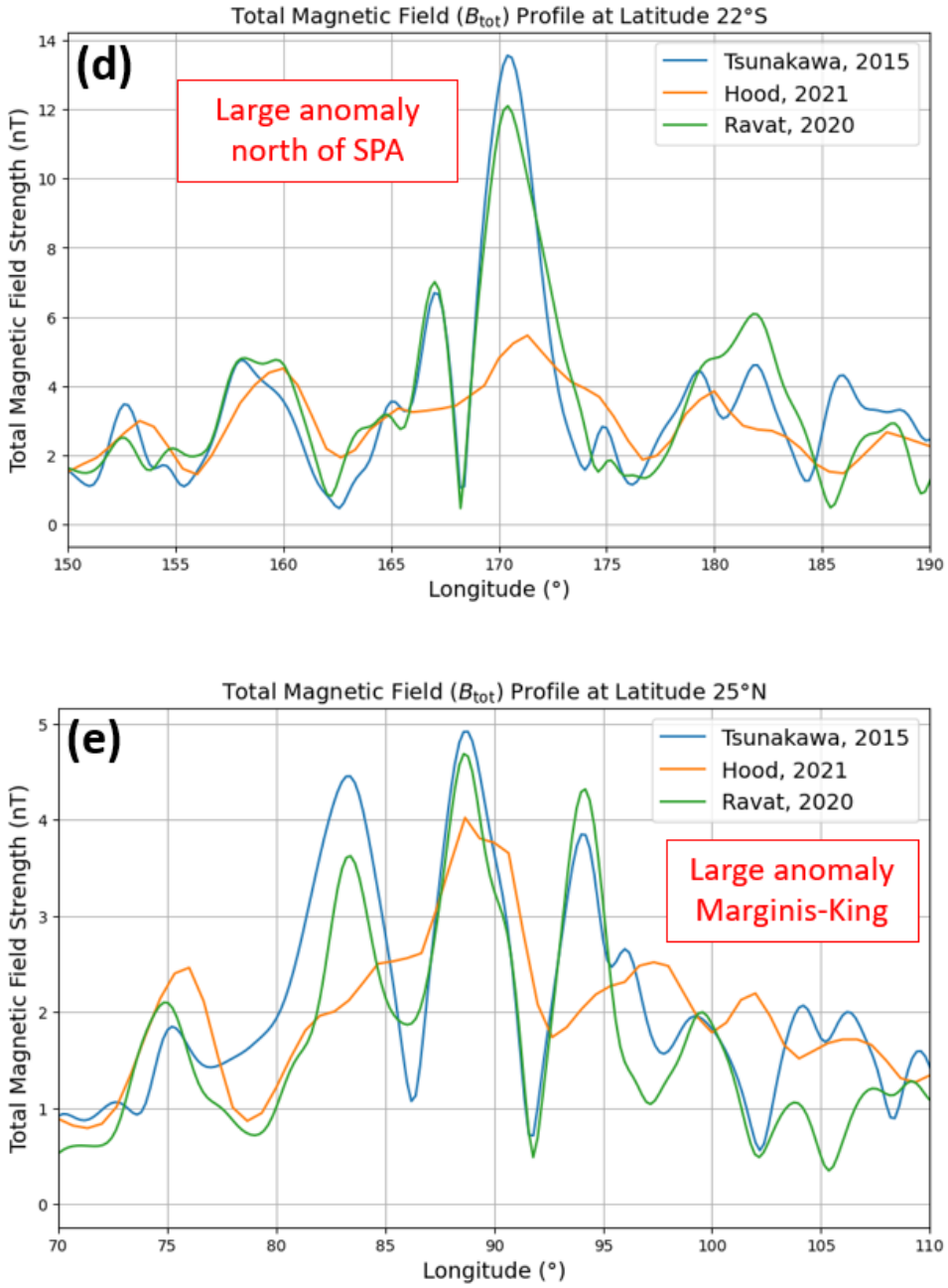

Figure A.2: Additional profiles (to figure 3.7) of the Tsunakawa, Hood and Ravat magnetic maps at selected latitude degrees and longitude ranges: 22°S and between 150°E and 190°E in correspondence with the large magnetic anomaly north of SPA basin and antipodal to the Imbrium impact basin in (d), 25°N and between 70°E and 110°E in correspondence with the large magnetic anomaly in the Marginis-King area and antipodal to the Orientale impact basin in (e). To see the longitudinal extension and latitudinal position of the profiles in a global map refer to figure 3.7.

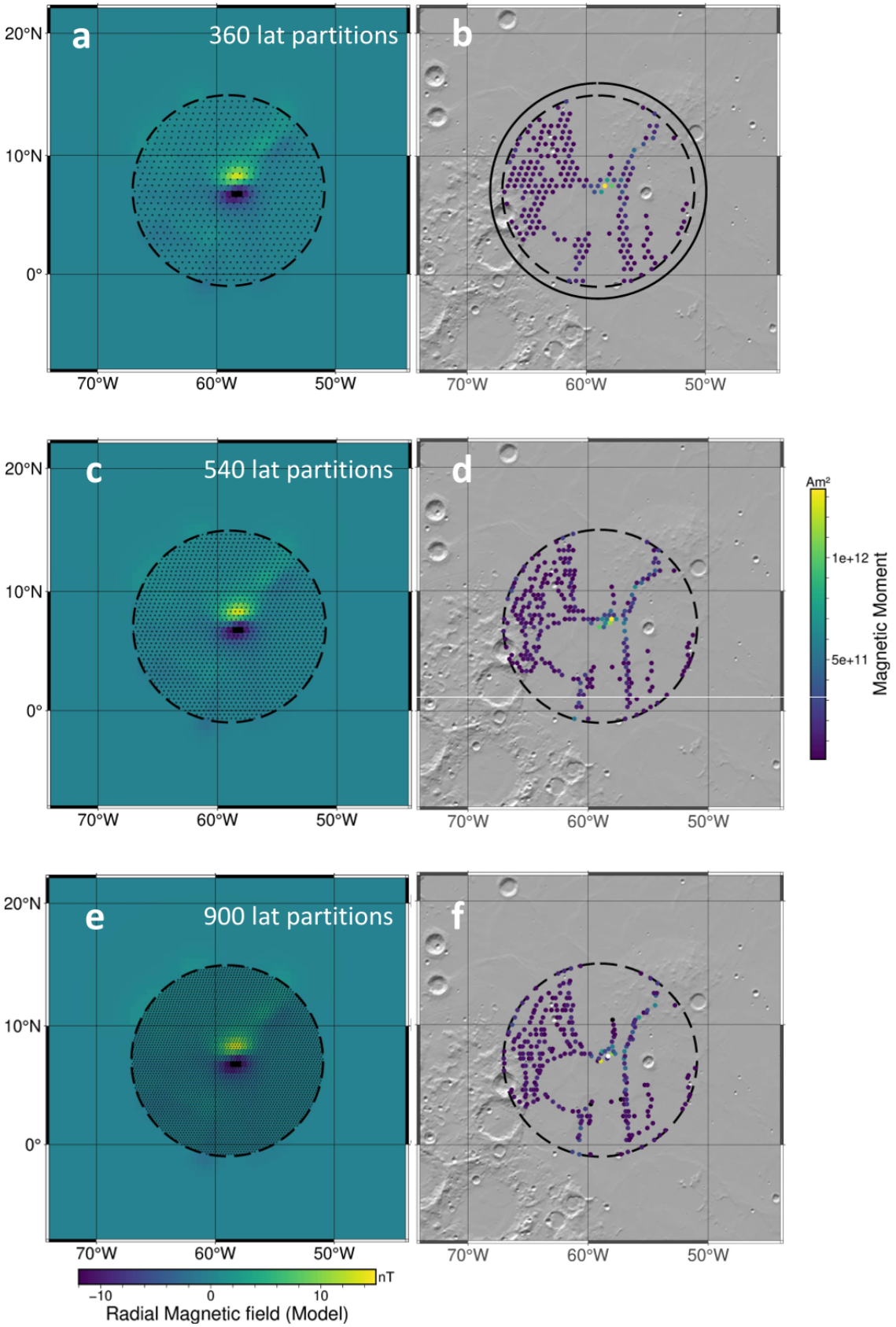

Figure A.3: Figure showing the modeled radial magnetic field (a, c, e) and the surface distribution of dipoles (b, d, f) for varying number of latitude partitions using the polar coordinate distribution method to evenly place points on the sphere. From top to bottom, 360 latitude partitions (approx 0.5° latitudinal separation between points), 540 latitude partitions (approx 0.33°) and 900 latitude partitions (approx 0.2°). The inversions use a dipole circle angular radius of 9°, observation circle angular radius of 9°.

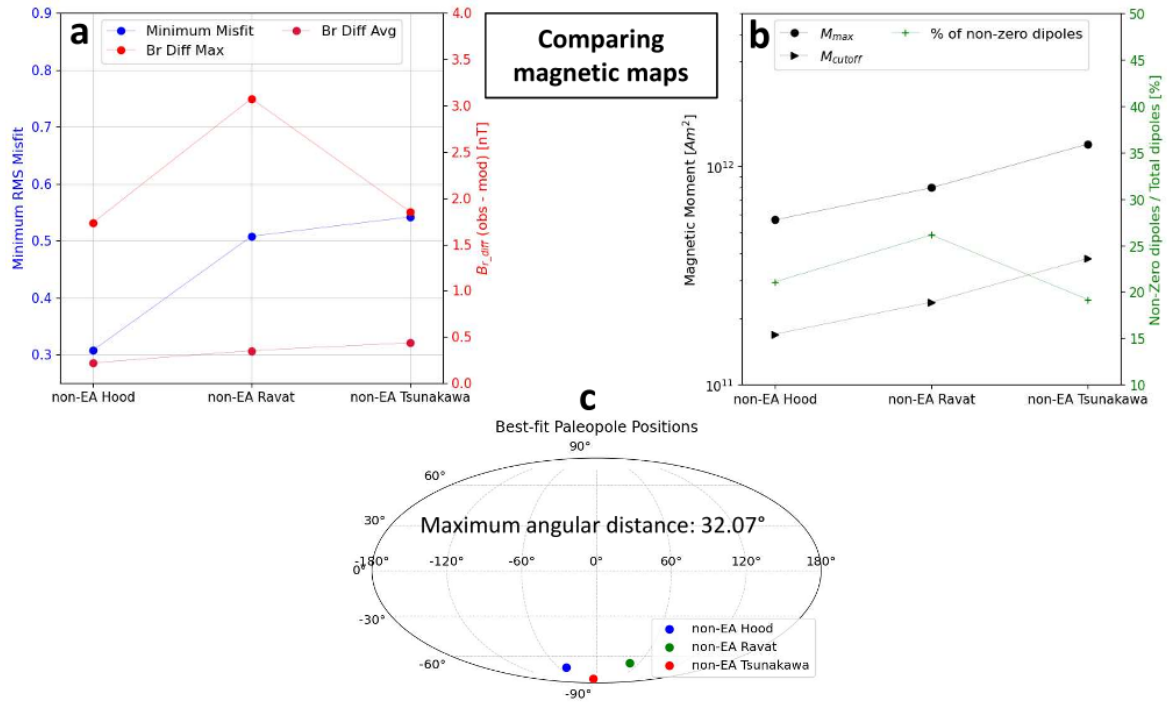

Figure A.4: Sensitivity plots analyzing inversion results for the standardized Reiner Gamma anomaly area using different magnetic maps, evaluating: (a) the minimum RMS misfit and the differences in radial magnetic field intensity, (b) the maximum and cutoff magnetic moments along with the percentage of non-zero dipoles, and (c) the best-fit paleopole positions. Data refers to the table in figure 5.3.

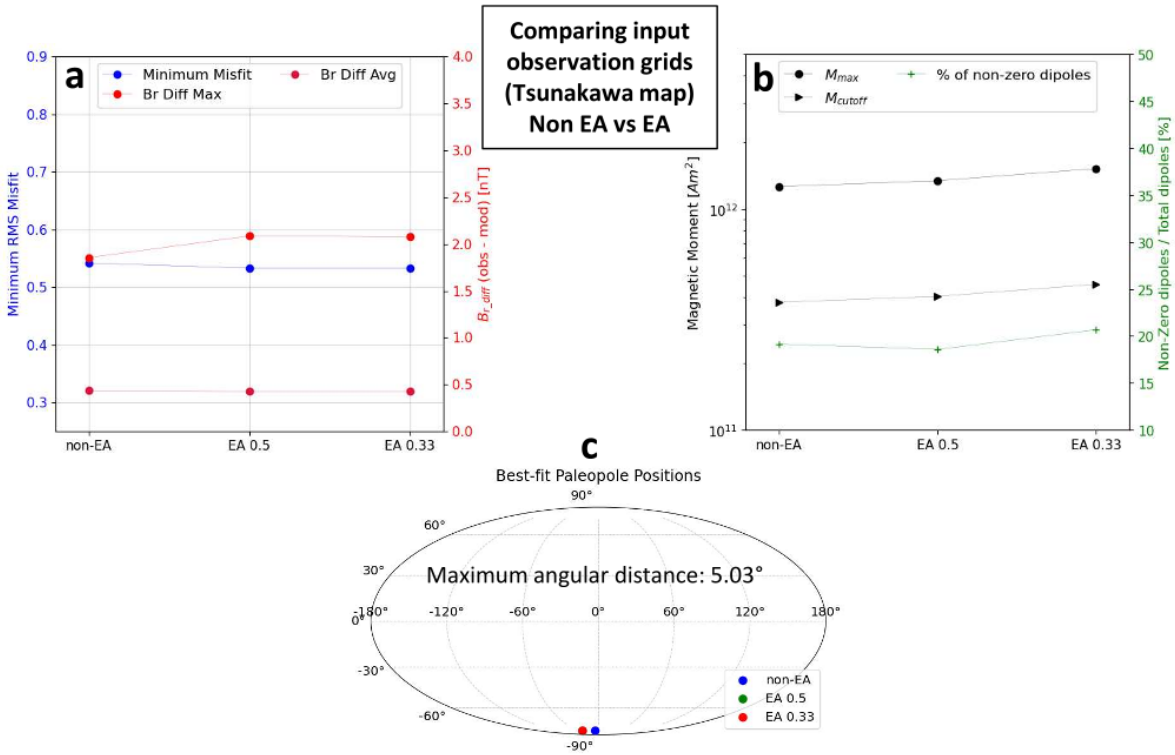

Figure A.5: Sensitivity plots analyzing inversion results for the standardized Reiner Gamma anomaly area comparing non-EA vs EA (res 0.5°) vs EA (res 0.33°) versions of the observation grid. More details on the a,b,c plots in figure A.4.

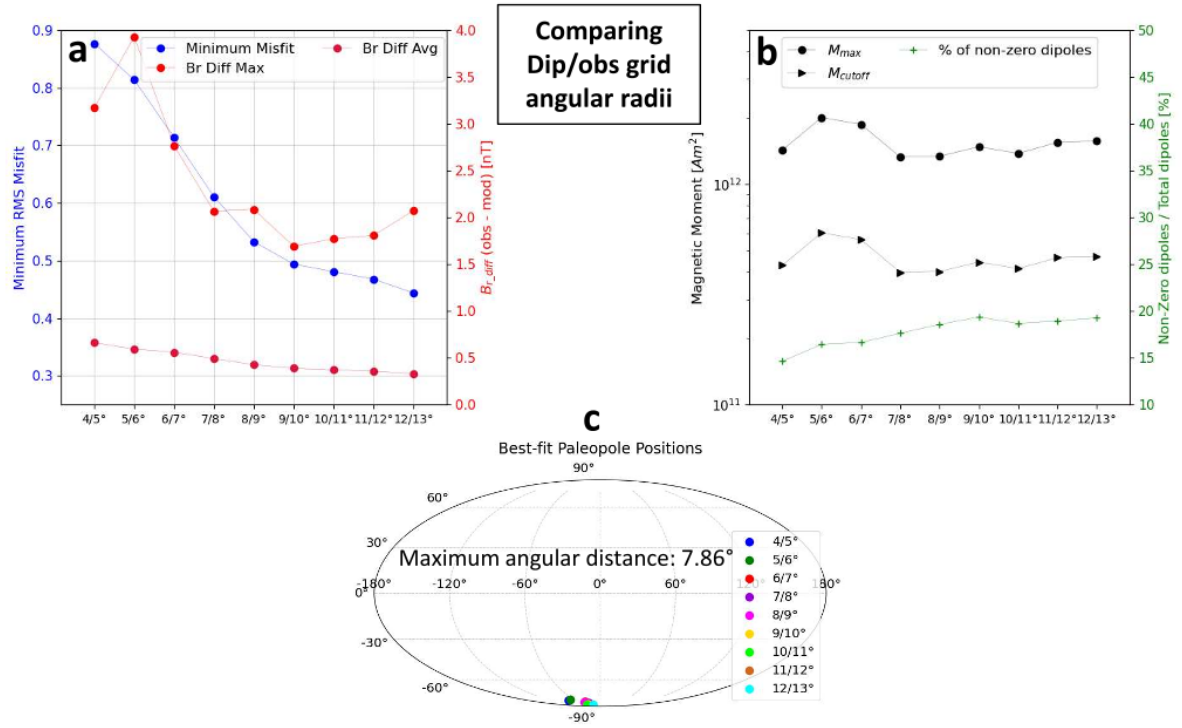

Figure A.6: Sensitivity plots analyzing inversion results for the standardized Reiner Gamma anomaly area comparing different angular radii for the dipole and observation grid. More details on the a,b,c plots in figure A.4.

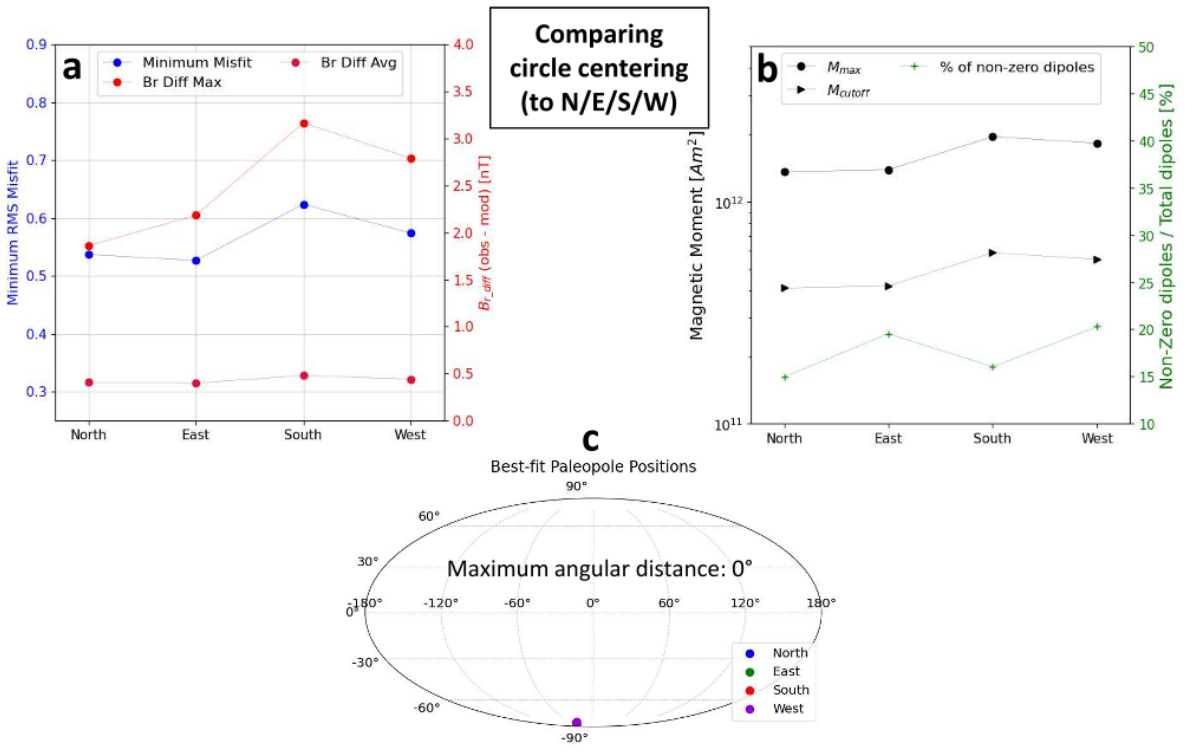

Figure A.7: Sensitivity plots analyzing inversion results for the standardized Reiner Gamma anomaly area comparing different centerings of the circles (more to the N/E/S/W). More details on the a,b,c plots in figure A.4.

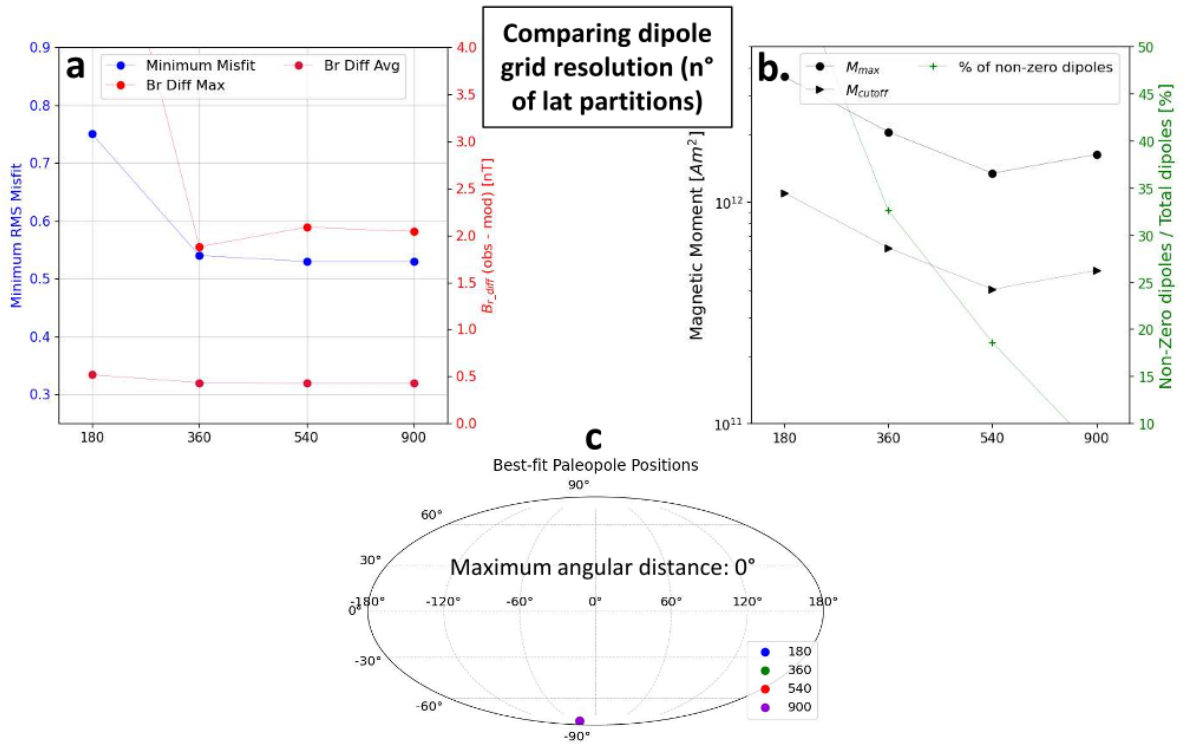

Figure A.8: Sensitivity plots analyzing inversion results for the standardized Reiner Gamma anomaly area comparing different resolution (number of latitude partitions) of the dipole grid. More details on the a,b,c plots in figure A.4.

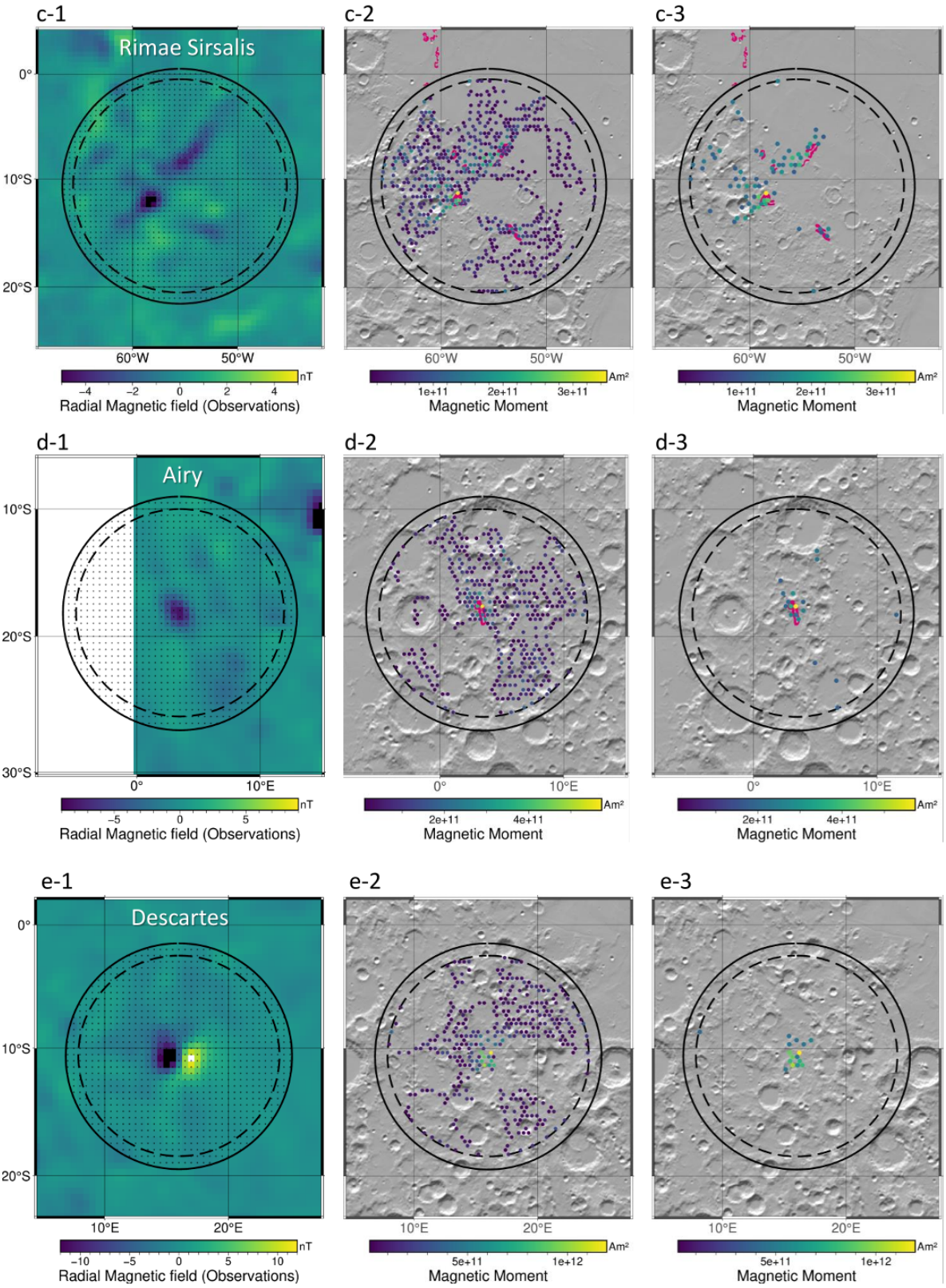

Figure A.9: Other results of the inversion of magnetic anomalies, showing the observed magnetic field [1] and the surface distribution of magnetized material (all dipoles above $10e^{10}Am^2$ [2] and those stronger than 30% of m_{max} [3]).

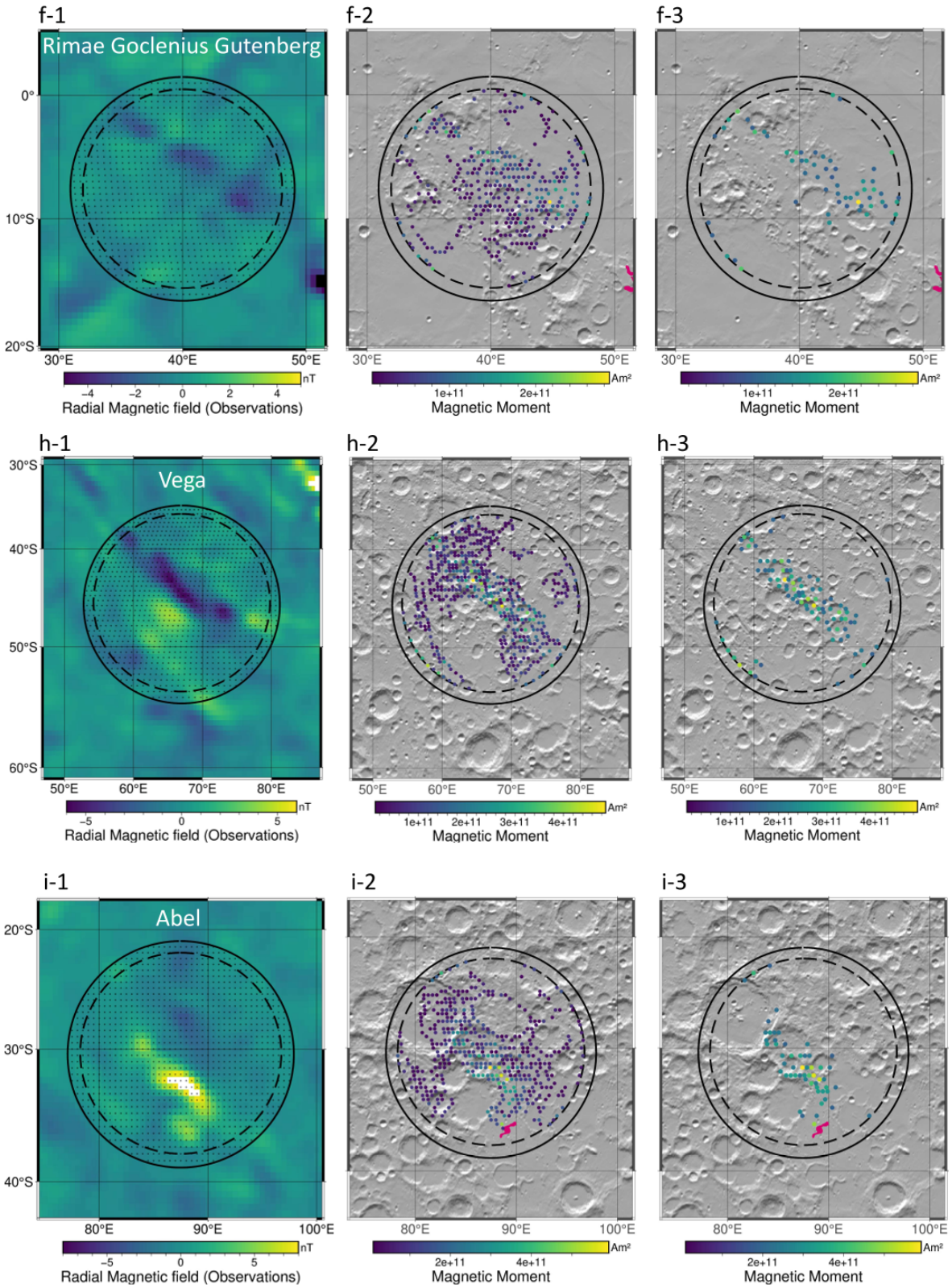

Figure A.10: Refer to figure A.9.

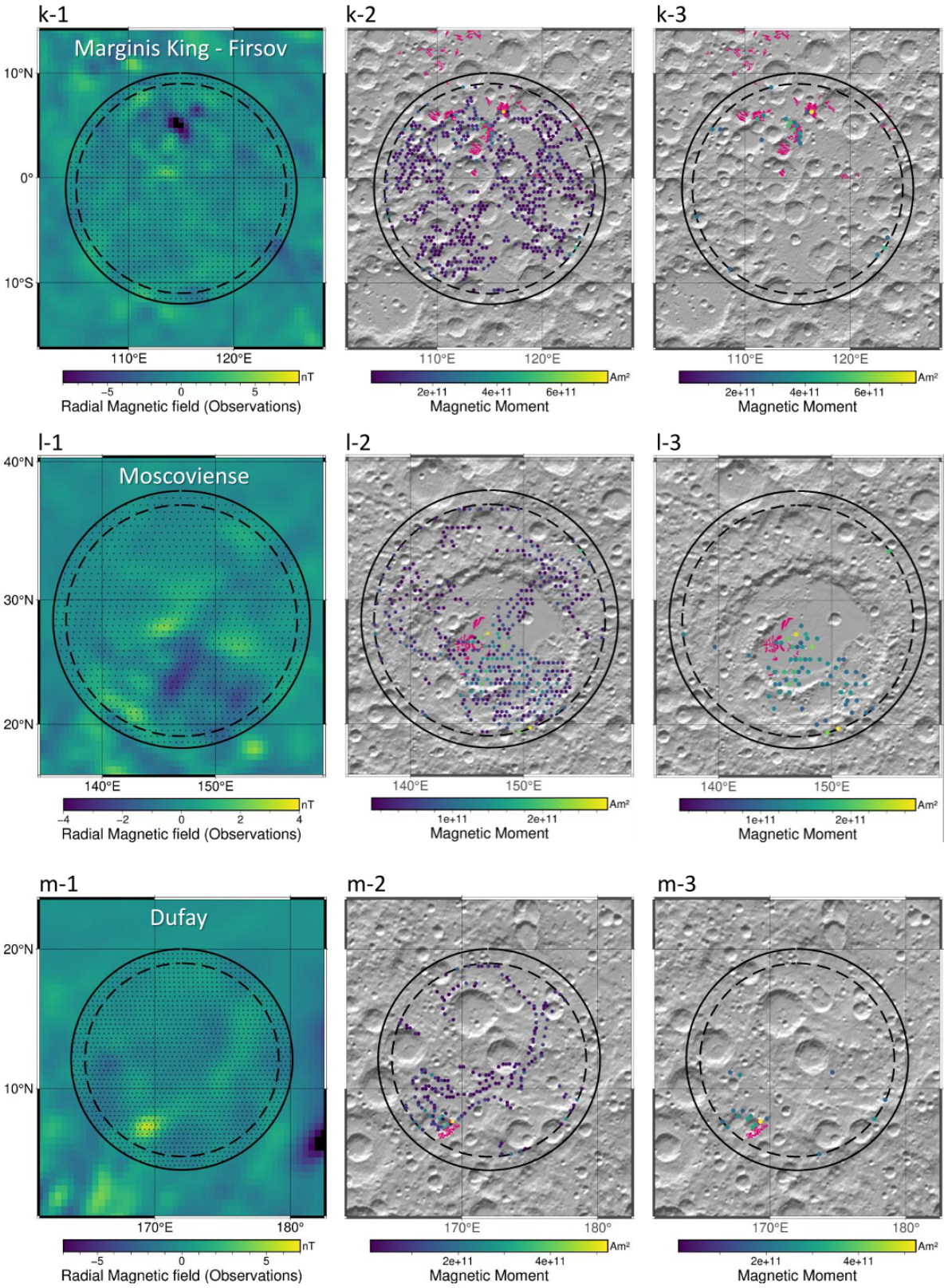

Figure A.11: Refer to figure A.9.

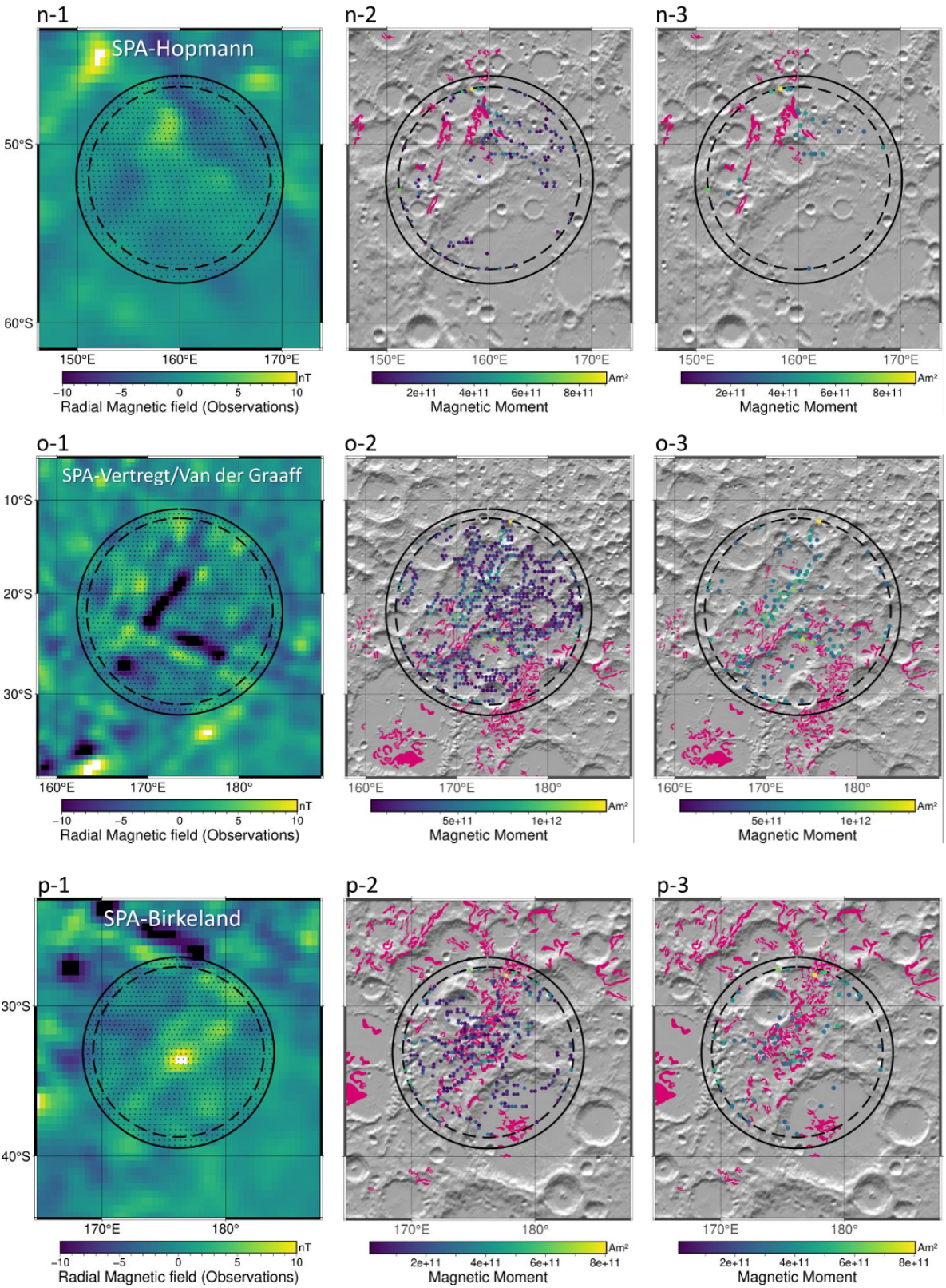

Figure A.12: Refer to figure A.9.

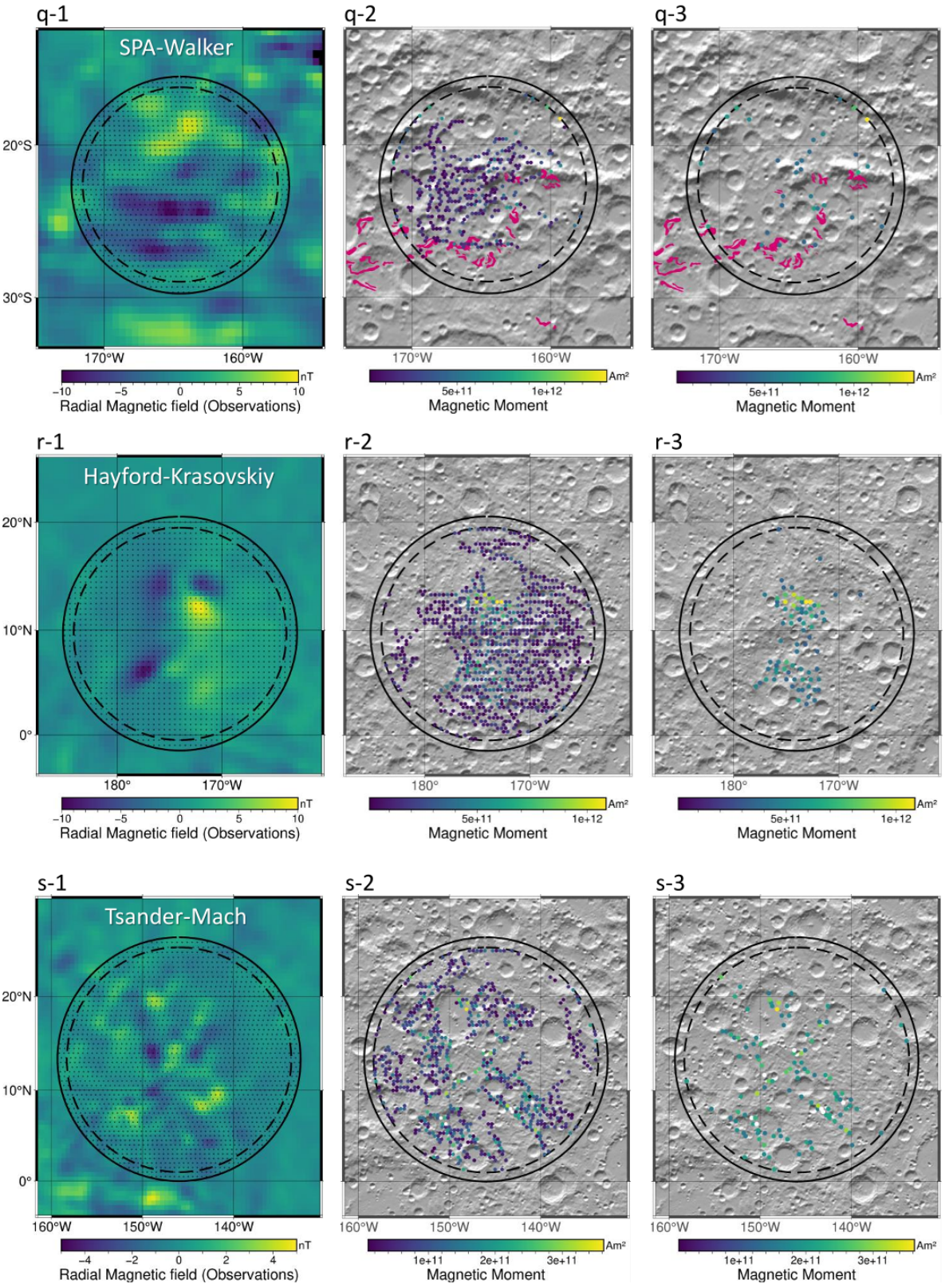

Figure A.13: Refer to figure A.9.

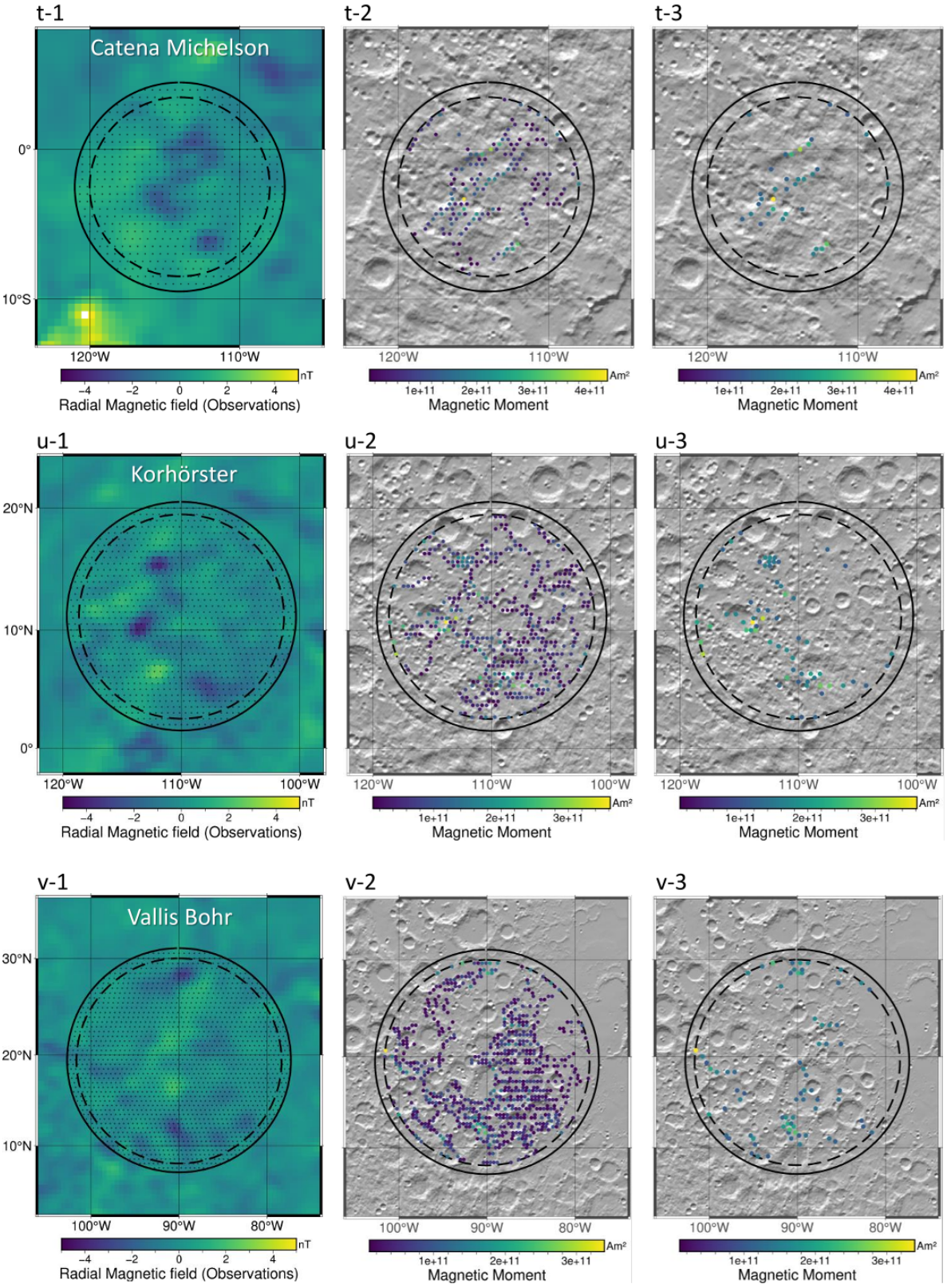

Figure A.14: Refer to figure A.9.

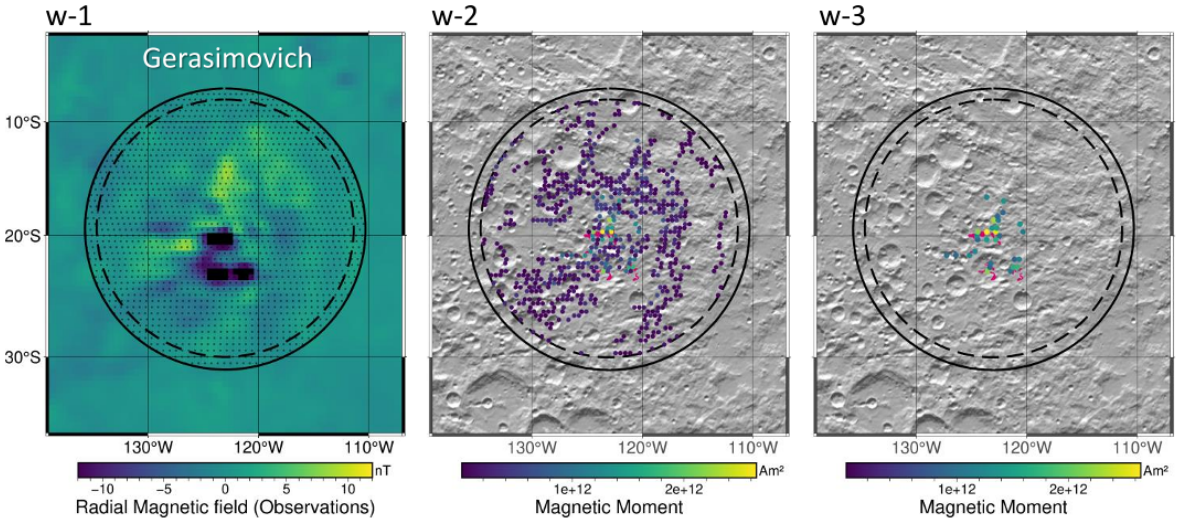

Figure A.15: Refer to figure A.9.

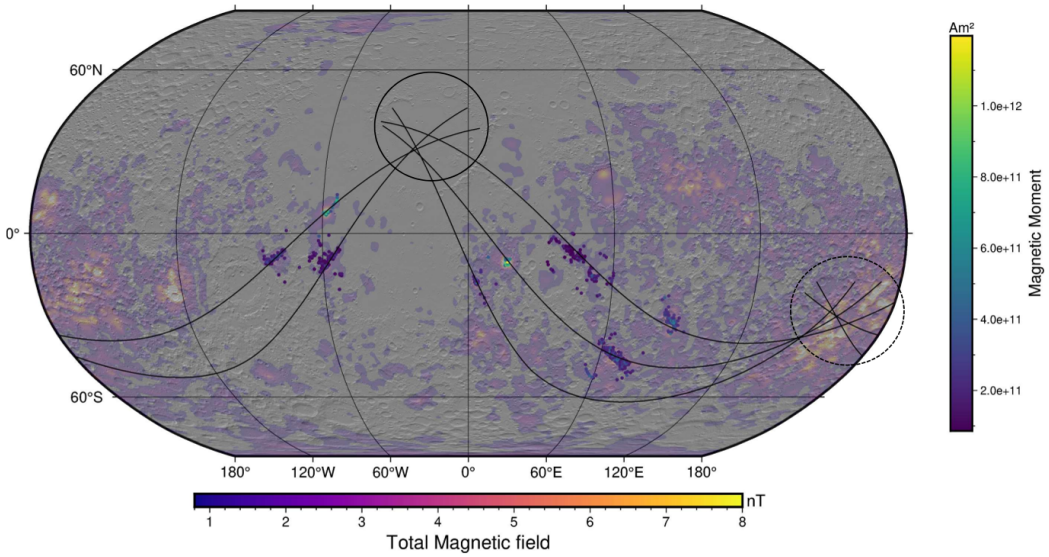

Figure A.16: Version of figure 7.1 where the dipoles share a unique scale for the magnetic moment.

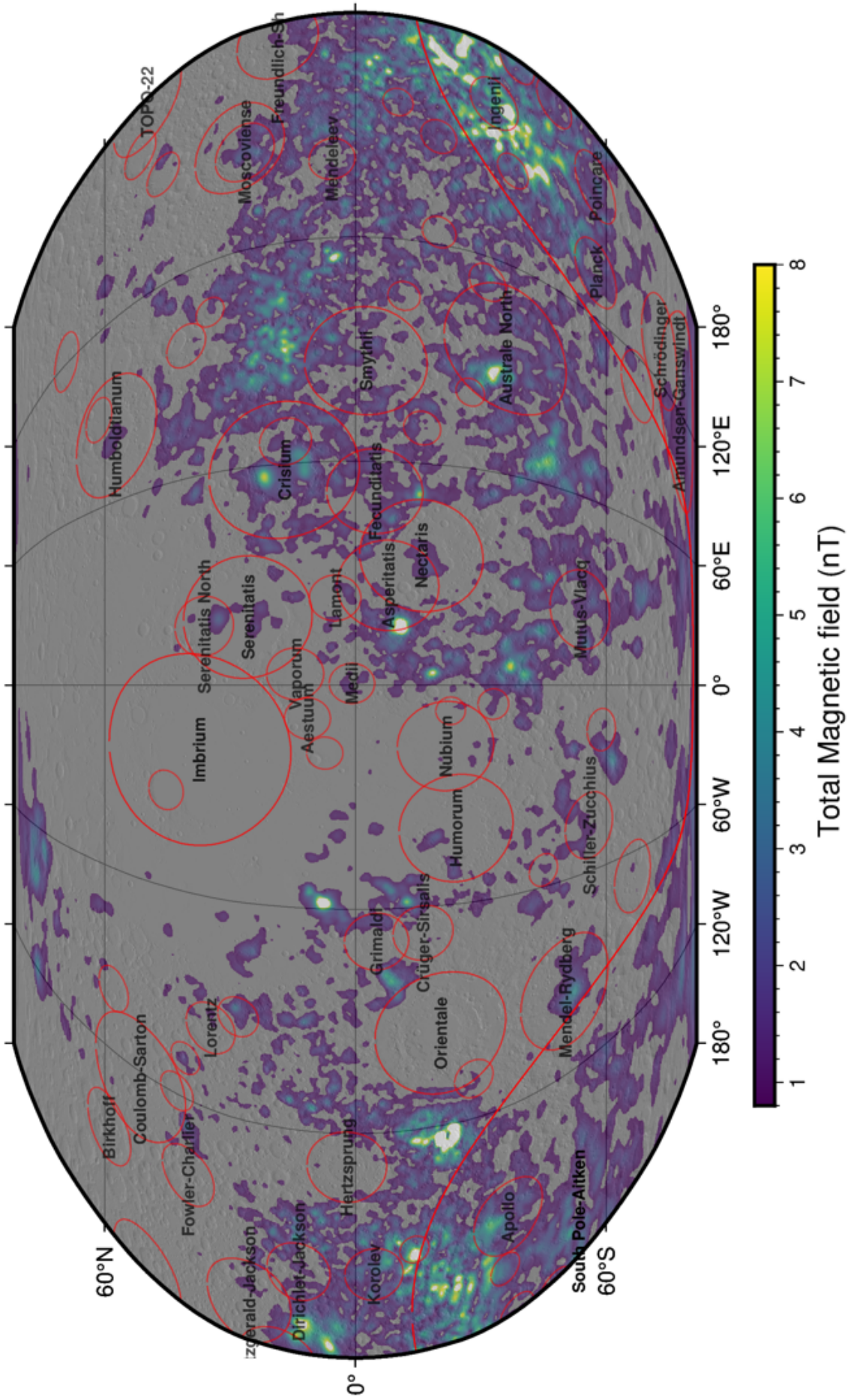

Figure A.17: Global map showing the location and size of large impact craters and impact basins above 200 km diameter (crater data from Neumann et al., 2015) compared to the Tsunakawa magnetic map at 30 km altitude.

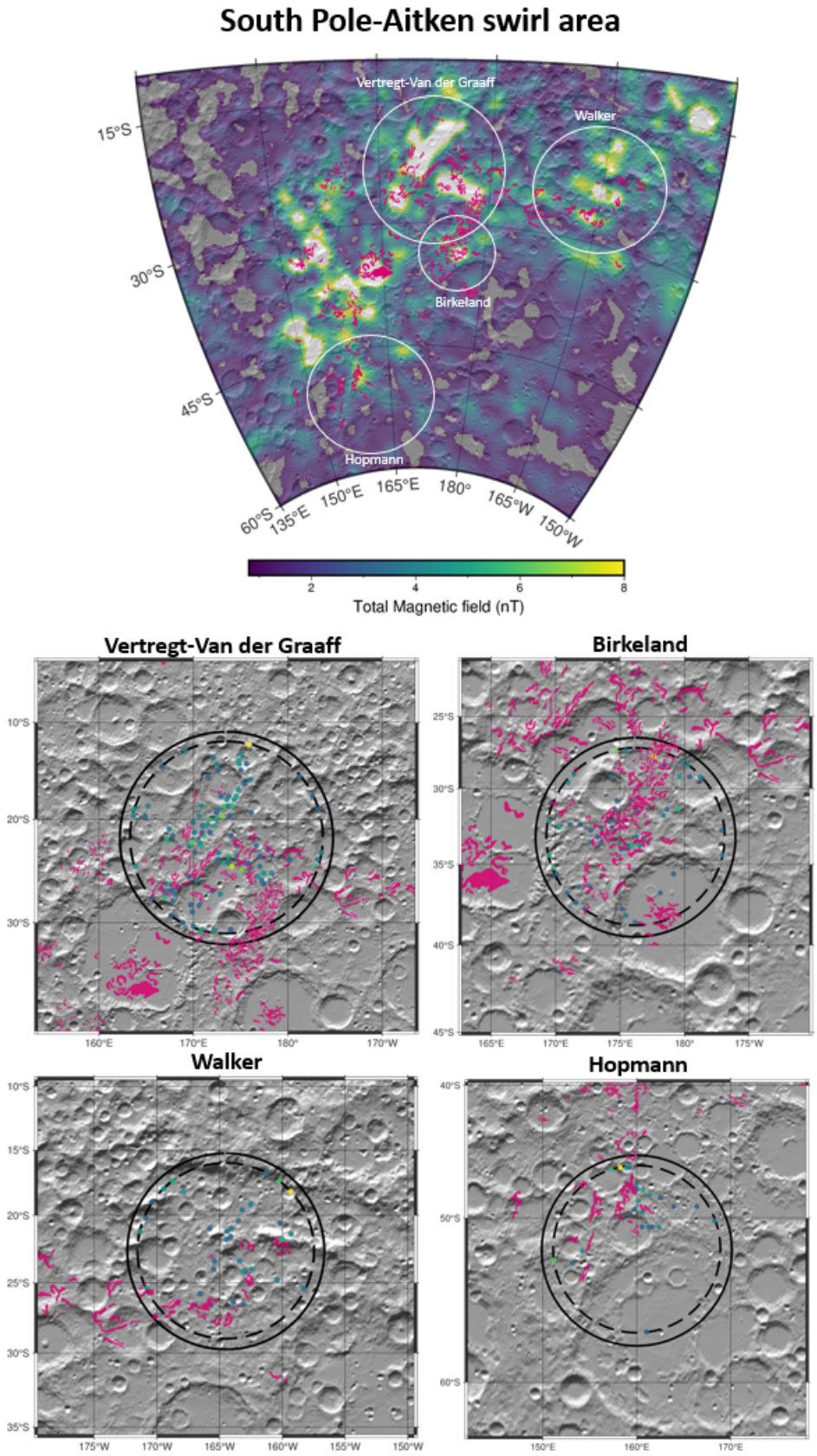

Figure A.18: Top: Correlation between lunar swirls and the magnetic field from the Tsunakawa map over the South Pole-Aitken swirl region. White circles highlight the areas analyzed using the Parker Inversion method. Bottom: Results of the inversion for the four regions, illustrating the relationship between the swirls and surface magnetized material (represented as magnetic dipoles with magnetic moments).

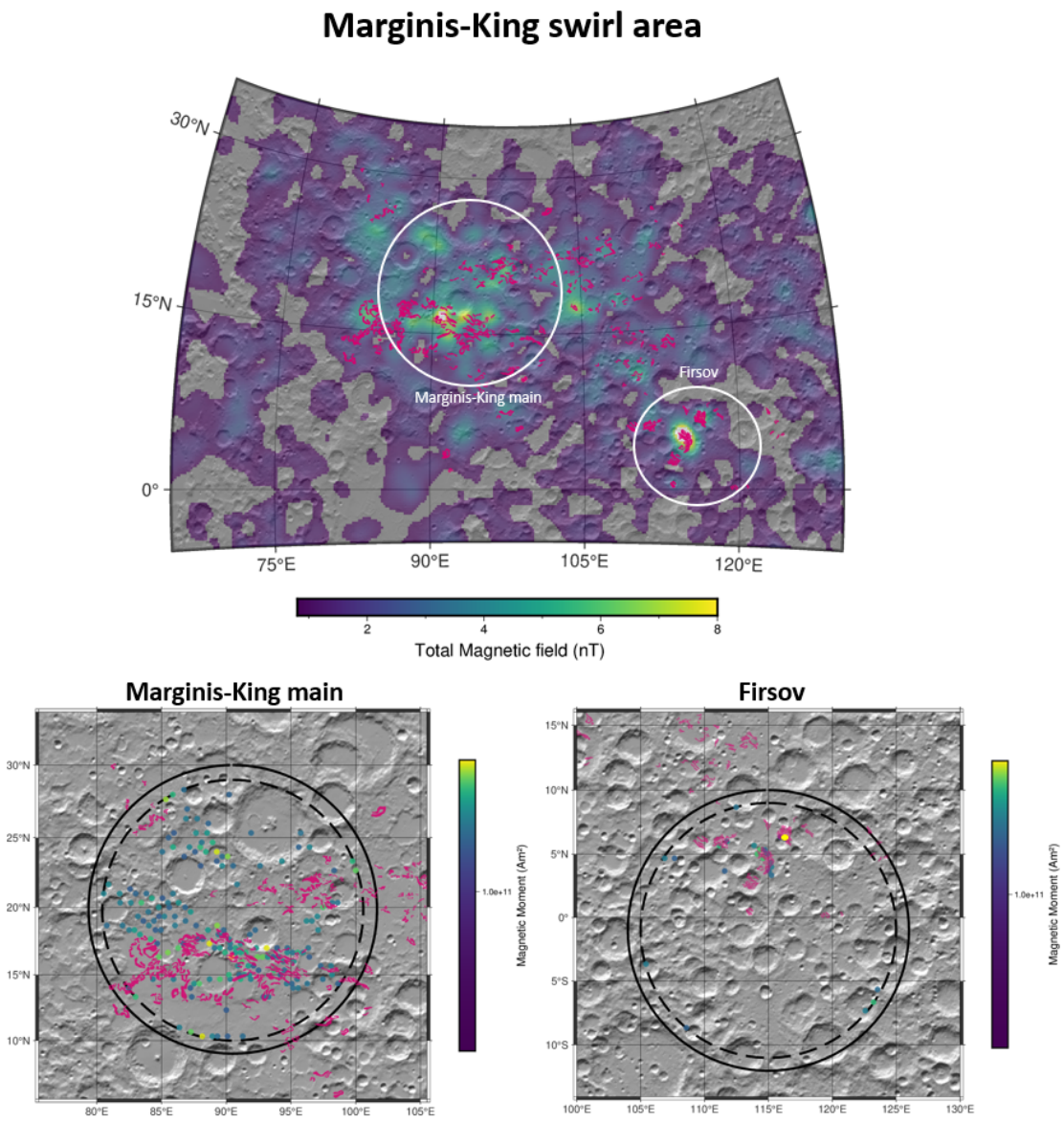

Figure A.19: Same as for figure A.18 but for the Marginis-King swirl area.